Physics of amorphous Selenium superlattice and its applications to X-ray-/photo-detectors

アモルファスセレン超格子の物性とX線/光検出器への応用

A Dissertation Presented to
the Graduate School of Arts and Sciences
International Christian University
for the Degree of Doctor of Philosophy

国際基督教大学　大学院
アーツ・サイエンス研究科提出博士論文

March 26, 2021

JOHN, Joshua Dumenkosi
ジョン　ジョシュア　ドゥメンコシ

Physics of amorphous Selenium superlattice and its applications to X-ray-/photo-detectors

アモルファスセレン超格子の物性とX線/光検出器への応用

A Dissertation Presented to
the Graduate School of Arts and Sciences,
International Christian University,
for the Degree of Doctor of Philosophy

国際基督教大学　大学院
アーツ・サイエンス研究科提出博士論文

March 26, 2021
２０２１年3月２６日

JOHN, Joshua Dumenkosi
ジョン　ジョシュア　ドゥメンコシ

審査委員会メンバー

Members of Evaluation Committee

主査 / Chief Examiner

岡野　健　教授

副査 / Examiner

田　旺帝　教授

副査 / Examiner

久保　謙哉　教授

副査 / Examiner

山田　貴壽 主任研究員(産業技術総合研究所)

Abstract

X-ray radiation is a key centerpiece of medical imaging. However, X-rays are a form of ionizing radiation, which is dangerous for living organisms. Young patients are at a higher risk as they have rapidly dividing cells. Clearly, these imaging modalities have to be used with limitation. Radiologists recognize the risks and provide guidelines for the maximum exposure. Nevertheless, a further improvement is to reduce the intensity used in the imaging process, which is possible if the detector is sensitive enough to capture the reduced number of X-rays. Thus, the requirement is an ultra-sensitive X-ray detector, and we proposed that a photo-detector based on amorphous Se superlattices can be used to detect X-ray photons at high sensitivity.

Amorphous Se superlattice structures were fabricated on Si and Ge substrates using thermal rotational evaporation. The resulting samples were characterized using Time of Flight Secondary Ion Mass Spectroscopy (TOF-SIMS), revealing the multi-nanolayer structure. Ultraviolet Photoelectron Spectroscopy (UPS) was used to investigate the Fermi level in Se. Using Raman Spectroscopy, the amorphous nature of the materials in the superlattice structure was confirmed. Spectroscopic Ellipsometry revealed quantum confinement in the superlattice structure. Using Deep Level Transient Fourier Spectroscopy (DLTFS) the trap energy levels in the individual materials, and the resulting modulation of energy levels due to the superlattice structure was observed. Current-Voltage (I-V) measurements revealed oscillations in the characteristics, a feature associated with superlattices.

From the experiments on superlattices, photo-detectors using Si as absorbing material, and superlattice Se as multiplier, were fabricated. The total thickness of the superlattices, was varied into 200 nm and 2 μm. Each type of detector was characterized using I-V, and Current-Time (I-T) measurements. The results were then used to evaluate the detector multiplication gain, showing that the gain depends on the number of layers. We could then show that the performance of the device could be engineered depending on the application by selectively varying the number of layers.

Towards X-ray detection, photo-detectors using Ge as absorbing material, and superlattice amorphous Se as multiplier, were fabricated and characterized. The results showed successful detection of X-rays and a responsivity comparable to other detectors in recent reports.

The results show a promising sensitive detector which may improve safety, allowing use of X-ray imaging during pregnancy, and on children without severe concerns. Additionally, such a system will open opportunities for innovation in X-ray imaging such as real-time imaging and automatic exposure (AE) control. Overall, this type of detector promises significant evolution in X-ray imaging.

医療診断用画像(Medical imaging)の撮影において，X線(X-ray)は重要な役割を果たしている．しかし，電離放射線の一種であるX線の人体への照射にはリスクが伴い，細胞分裂が活発な乳幼児ほどリスクは高まる．それゆえ，X線による画像撮影に制限があり，放射線学会はこのリスクを踏まえ，最大被爆量に関するガイドラインを示している．しかしながら，リスクの可能性は画像化プロセスでのX線強度を低減することで大きく抑えられる．このことは，低減された線量のX線を捉えるのに十分な感度を有する検出器を用いることで可能となる．超高感度X線検出器(Ultra-Sensitive X-ray Detector)として，超格子アモルファスSe(Amorphous Se superlattice structure)ベースの光検出器を用いることで，X線光子の超高感度検出が可能であることを提示した．

シリコンおよびゲルマニウム基板に超格子アモルファスSeを作製するために，真空回転蒸着法を用いた．飛行時間型二次イオン質量分析法(TOF-SIMS)を用いて構造解析を行ったところ，作製した試料はナノメートルオーダーの多層膜構造になっていることを明らかにした．紫外線光電子分光法(UPS)を用いた測定でSeのフェルミ準位を，ラマン分光法で超格子構造中の物質が非晶質であること，分光エリプソメトリーで超格子構造中に量子閉じ込めがあることを明らかにした．また，DLTFS法(Deep Level Transient Fourier Spectroscopy)は，不純物や欠陥によってバンドギャップ中に作られたキャリアを捕獲するエネルギー準位が，超格子構造では変調していることを示した．さらに，電流電圧測定(I-V)から，超格子に伴う電流の振動現象を観測した．

超格子アモルファスSeベースの光検出器の実験では，シリコンを光吸収材料とし，超格子Seをキャリアの増倍層とした．超格子薄膜の厚さは200nmと2μmの二種類を用意した．それぞれの検出器の特性評価には，I-Vと電流時間測定(I-T)を用いた．得られた結果から検出器の増倍利得を評価したところ，利得は層の数に依存していることを明らかにした．このことから，層の数を選択的に変化させることで，用途に応じたデバイスの性能を設計することが可能であることが示された．

X線検出に向けて，X線吸収材料としてゲルマニウムを用い，超格子アモルファスSeをキャリアの増倍層とした光検出器を作製し，特性評価を行なった．その結果，X線の検出に成功し，感度は，現在報告されている他の検出器と比較しても遜色のない値であることを示した．

以上の結果より，超格子アモルファスSeベースの超高感度光検出器は，妊娠中の胎児および乳幼児に対してのX線撮影がもたらす影響を払拭し，かつ安全性が向上することができる高感度光検出器であることを示した．さらに，本検出器はリアルタイムでの画像化や自動露出機構(AEC)などを可能とし，X線画像処理に大きな革新をもたらすことになる．従って，本研究で開発した検出器はX線画像撮影に大きな進化をもたらすことを約束するものである．

Acknowledgements

I would like to take this opportunity to thank the following people for their contributions to my research:

Prof. Ken Okano for the opportunity and mentorship. I appreciate his valuable guidance, timely insights and encouragement throughout my graduate studies at International Christian University (ICU).

Dr. Ichitaro Saito, Dr. Tomoaki Masuzawa, Dr. Takatoshi Yamada for their kind and patient assistance with many experiments, manuscript preparation and reviews.

Research advisors Prof. Wanjae and Prof. Kubo for the mentorship, guidance and reviews of this work.

Prof. Dr. D. R. T. Zahn of Chemnitz University of Technology and his team for welcoming me to visit their labs, access facilities, and for cooperating in the research work.

Prof. D. H. C. Chua of National University of Singapore for his insights and reviews.

Coauthors and friends, Dr. A. Sharma and Dr. S. Okano for their awesome contributions my research, and in general.

ICU Okano lab members Mr. Tsuzaki, Mr. Enomoto, Ms. Tanaka, Mr. Miyachi and Mr. Nishimoto for all their assistance and interesting experiences we shared at the lab.

ICU Graduate school staff for their consistent guidance in the course.

President Ito of Eiwa Bussan and his team for their great support.

The Mutendas for their anchoring support.

I am especially grateful to my parents and brothers for their support and patience. Thanks also to my friends who have always been there, providing emotional and spiritual support all the way through this course.

Contents

Chapter 1

Introduction

X-ray radiation has been the centerpiece of medical diagnostic imaging since the discovery by Roentgen in 1895. Many useful imaging modalities such as Computed Tomography (CT) and fluoroscopy have been innovated based on X-ray. These imaging modalities have become indispensable to modern medicine. X-ray based imaging is preferred because it is non-invasive and provides detailed information for surgical planning and for guiding interventional procedures such as placing of devices into the body.

However, a critical challenge to using X-rays is that they have energy that is high enough to remove electrons from atoms, leaving the atom in a charged state called an ion. As such, X-rays are classified as ionizing radiation. This ionization is particularly dangerous if it happens in atoms that make up living organisms [1]. Clearly there are some risks involved in using X-rays on patients.

Infants and young patients are at an even higher risk. Growing children have rapidly dividing cells in which DNA metabolism is very active [2]. Their DNA is at a high risk of getting damaged by ionizing radiation, which increases the chances of cancer. Children also have cells with a higher water content, and given the roughly cylindrical volume of the body, the water strongly absorbs X-ray rather than letting it pass through. This again increases the risk for young patients. Clearly modalities such as fluoroscopy or CT with inherently large exposure have to be used with limitation on young patients.

The Japan Association of Radiological Technologists (JART) has recognized the increased risks to young patients and provided guidelines as to the maximum exposure that young patients can receive from a CT scan [3]. These guidelines show some recommended dosage limits, measured using a standardized index called the Computed Tomography Dosage Index ($CTDI_{vol}$) in mGy, for CT scans of the head, thorax and abdomen. The recommendations are shown in Table. 1.1.

For comparison, JART suggests that adult patients can receive 85 mGy for head scan, 18 mGy for the thorax region and 20 mGy for the upper abdomen region. Another

Table 1.1: Recommended dosage limits, measured as the Computed Tomography Dosage Index ($CTDI_{vol}$) in mGy, for children below 1 year of age (1歳未満), 1 - 5 years of age (1 - 5歳), and 6 - 10 years of age (6 - 10歳), for a head (頭部), thorax (胸部) or abdomen (腹部) CT scan. The values given are for a 16 cm phantom, with values for a 32 cm shown in brackets. (from http://www.jart.jp/activity/hibaku_guideline.html)

	1歳未満 $CTDI_{vol}$ [mGy]	1 - 5歳 $CTDI_{vol}$ [mGy]	6 - 10歳 $CTDI_{vol}$ [mGy]
頭部	38	47	60
胸部	11 (5.5)	14 (7)	15 (7.5)
腹部	11 (5.5)	16 (8)	17 (8.5)

comparison is with X-ray photography with maximum of 3 mGy for the head, 6 mGy for the thorax image from the side and 11 mGy for the abdomen from the side [3].

While the recommendations for exposure go a long way in protecting young patients, there is need to limit exposure even further. One way to reduce exposure is to reduce the intensity of the X-rays used in the imaging process. Lower intensity of X-rays can be used if the detector is sensitive enough to capture the reduced number of X-rays. A decrease of the dosage by one order would be more safe and possibly allows several repeated measurements without significantly increasing the accumulated dosage. A decrease of the dosage by this magnitude requires that the sensitivity of the detector increase by the same one order. Thus, the requirement is an X-ray detector with at least one order higher sensitivity compared to detectors used at present. Amorphous Se based photo-detectors are a possible candidate, known for their ultra-sensitive detection due to the avalanche multiplication phenomenon observed in their transport features under an applied field [4, 5, 6, 7].

1.1 Photo-detectors based on amorphous Se

The operation of photo-detectors can be described by basic processes of photoelectric absorption and transport to the signal readout structures [8, 9]. In photoelectric absorption a photon incident onto the photo-detector material interacts with the material atoms, imparting all its energy, which creates an electron-hole pair [10, 11]. If there

is no source of electric field to separate the electron and hole, they will recombine in germinate recombination. If there is an electric field, then the electron and hole can be separated and drifted along the direction of the field. Along this drift transport, the electron or hole may also interact by collision with material atoms, dislodging other electrons such that the carriers appear to multiply. At the end of the drift path, the charge carrier electrons or holes can be collected and read out as a signal that represents the incident photon. We examine the properties of amorphous Se with respect to these processes towards the detection of X-rays.

1.1.1 Background

Well known for its ultrahigh sensitive photo-detection capabilities, amorphous Se is one of the main candidates for envisioned low-dose ultra-high sensitive X-ray imaging devices for medical applications [5, 12, 13, 14, 15, 16, 17, 18, 19]. The ultra-sensitivity is attributed to avalanche multiplication observed in amorphous Se films. The avalanche multiplication phenomenon was initially thought unlikely in theory due to the short mean free path in these materials [20]. Nevertheless, experiments on the transport properties in amorphous materials soon showed characteristics of impact ionization and avalanche multiplication [21]. These properties could be leveraged to make an ultra-sensitive vacuum type pick up tube for television, known as the High-gain Avalanche Rushing Photoconductor (HARP) [22]. The HARP has been innovated into solid state forms such as the HARP-CMOS and the HARP-TFT. In the HARP-CMOS, the amorphous Se HARP film is coated onto a complementary metal oxide semiconductor (CMOS) imaging array and biased with a field to operate in avalanche mode [23]. The HARP-TFT is similar in principle albeit using thin-film transistors [13]. All these devices have exhibited exceptional performance in detecting visible light.

Another direction of innovation has been the use of cold cathode field emission to drive the amorphous Se film [24, 25, 26]. In a diode structure vacuum device, the amorphous Se film is used as the photo-detecting anode, and a Spindt type field

emitter is used as the cathode. Operating at significantly lower field emission voltages compared to Spindt type emitters has been successfully demonstrated using a novel low threshold nitrogen-doped diamond field emitter [27, 28, 29, 30, 31, 32]. Diode and triode structures of these devices have been demonstrated for visible light detection, with multiplication gains of 10 - 40 being measured [33, 6, 34]. Here the multiplication gain $M = \frac{\Delta I}{qN_0}$ is given as the ratio of the light induced current (difference between dark current and current under illumination $\Delta I = I_{photo} - I_{dark}$) to the number of incident photons N_0, with q as the fundamental electronic charge. Detection of high energy ultraviolet photons was also demonstrated using this diamond driven amorphous Se photo-detector, showing M of over 1000. This is a promising results towards detection of higher energy photons.

1.1.2 Absorption of X-ray photons in amorphous Se

Amorphous Se is desirable for X-ray detection due to its ability for direct conversion. The mechanisms for absorption and photocarrier generation of high energy photons are reviewed in Appendix D. In direct conversion, X-ray photons are directly converted to a charge carrier signal for readout [35, 36, 14, 37]. Compared to scintillator based detectors which first down-convert X-ray photons to visible photons before detection (indirect conversion), direct conversion materials offer significant resolution, noise and response time performance [38, 39, 11]. Several attempts at direct conversion using amorphous Se have been demonstrated such as the Flat Panel X-ray Imager (FPXI) which has commercial applications in mammography and tomosynthesis [5, 12, 13].

Amorphous Se films for photo-detectors are fabricated with the inclusion of As_2Se_3 either mixed in the bulk [15], or in a mille-feuille structure [40]. The incorporation of As_2Se_3 is for stabilization from temperature degradation given that the amorphous Se takes a crystalline phase at temperatures above its glass transition of about 318 K [37]. Herein, we use mille-feuille structured films fabricated using rotational evaporation. We examine the absorption characteristics of the films to high energy X-ray photons

by calculating the half value layer (HVL) of the film for a range of photon energies.

The Half Value Layer (HVL) gives the thickness of any given material where half of the incident energy is absorbed [41]. The HVL is calculated using data from the National Institute of Standards and Technology (NIST) XCOM database [42].

$$HVL = \frac{\ln\left(\frac{1}{2}\right)}{\left(\frac{\mu}{\rho}\right)\rho} \tag{1.1}$$

where $\left(\frac{\mu}{\rho}\right)\rho$ is the mass attenuation coefficient, μ is the attenuation coefficient and ρ is the material density. The HVL variation with incident photon energy of a stoichiometric equivalent (1:1 ratio by volume of Se and As_2Se_3) of the multi-layer amorphous Se structure, along with conventional materials Si and Ge, is shown in Fig. 1.1. As shown in Fig. 1.1, the HVL increases as the photon energy increases. For an amorphous Se detector of length L, photons of energy E_{ph} will have a HVL of x, at which about 50 % of the incident photons have produced electron hole pairs. This then means that the remaining length of the photo-detector, $L-x$, is used for transport and multiplication. The multiplication factor depends on the transport length as $M \propto \exp(\alpha(L-x))$, where α is an ionization cross section [20]. Thus for the same detector length, as the photon energy increases, the multiplication gain reduces. The total length of the amorphous Se film could be increased accordingly. However, given that the transport and multiplication is field depended, thicker films would require higher applied field.

Typical amorphous Se films used for detection in mammography and tomosynthesis are 200 μm thick and are operated in a 'normal' (transport without multiplication) mode with applied fields of about 10 V/μm (2 kV applied voltage). The threshold field for multiplication in amorphous Se is about 70 V/μm [19, 20, 43]. As such, operating the detector in 'multiplication' mode would require 14 kV applied voltage, which poses practical challenges with insulation.

Clearly it would be beneficial if the absorption layer was comparatively thin. This is possible if the absorbing material has a high atomic mass, Z [16]. There has been

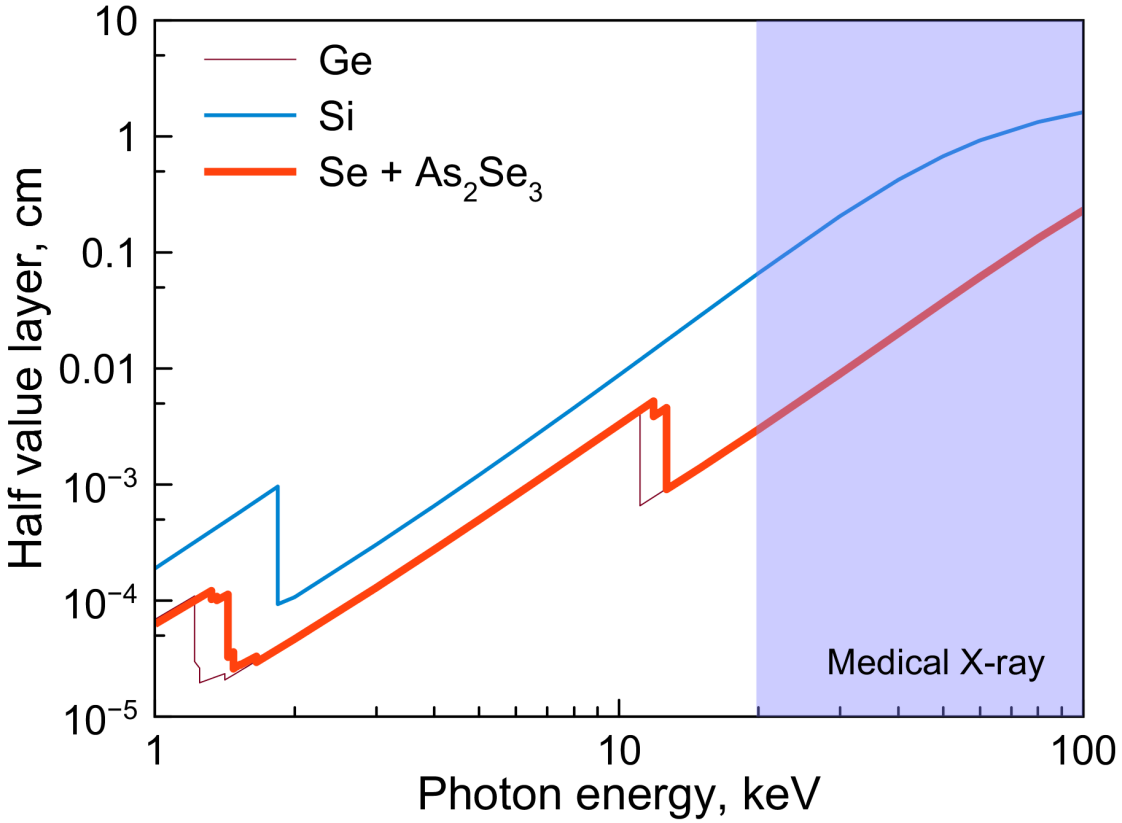

Figure 1.1: The Half Value Layer (HVL) thicknesses of multi-layer amorphous Se (1:1 ratio by volume of Se and As_2Se_3), Si and Ge for different photon energies. The shaded region shows X-ray energies used in medical imaging. For the same energy, Ge and multi-layer amorphous Se are more absorbing for X-ray photons.

significant progress in the development on high Z absorbing materials such as CdTe, PbO and perovskites [44, 45, 46, 47, 48, 49, 50]. These materials have shorter HVL values (better absorption) since their constituent atoms have a high atomic mass. Conventional semiconductor materials such as Si and Ge are also strong candidates for application as absorbing materials [11]. Conventional materials have well established methods of purification and fabrication such that high quality monocrystalline wafers are available off the shelf. These materials also have established device fabrication method such that the photo-detector can be directly integrated with the readout circuitry.

We therefore propose separating the absorption and transport components of the photo-detector from being the single material amorphous Se. Instead, we propose a multi-layer multi-material structure with some layers specialized on absorption and photo-generation of carriers, and other layers and materials applied for transport and multiplication gain. Absorption layers may use specialized materials such as high Z absorbing materials or perovskites. Amorphous Se is then applied for transport and multiplication to amplify the carriers generated in the absorbing layers.

1.1.3 Multiplication of charge carriers in amorphous Se

The high sensitivity of amorphous Se based photo-detector performance is attributed to avalanche multiplication observed in amorphous Se at high fields of over 70 V/μm [19, 20, 43]. The avalanche multiplication phenomenon has been described by models like the Lucky Drift, Polaronic-Supersonic Transformation, and Cascade Multiplication [22, 20, 51, 52].

The Lucky Drift model has its origins in the Lucky Electron model [53]. In the Lucky Electron model, an electron moving along the direction of the applied field F gains energy qFz after traveling a distance z. If the threshold energy for an ionization event is E_{th} then a lucky electron travels a long enough distance z to acquire E_{th} and therefore possibly impact and ionize. Unlucky electrons experience frequent collisions

and thus never reach E_{th}. However, this model could not explain experimental results.

The theory of impact ionization was then improved by introducing the Lucky Drift model [54]. In the Lucky Electron model, the carrier loses its momentum and energy on scattering collisions, whereas in the lucky drift model, the momentum relaxes much faster than the energy. An electron can experience collisions during its drift, losing its momentum, and yet still gain energy, possibly reaching E_{th}. As such, the model requires that the mean free path for momentum relaxation, λ, be less than the mean free path for energy relaxation, λ_E, ($\lambda < \lambda_E$). The energy relaxation mean free path λ_E determines the average distance between inelastic collisions. The lucky drift model applied to amorphous Se gives λ_E of about 2.6 - 6 nm for E_{th} for $\frac{E_G}{2}$ up to $E_G \approx 2$ eV.

The Polaronic-Supersonic Model emanates from the comparison of carrier drift velocities in amorphous Se with respect to the speed of sound [51]. There appears to be a relationship between the threshold field for avalanche multiplication, at 70 $\mathrm{MVm^{-1}}$, and the field where the drift mobility transcends the longitudinal sound velocity of 1.8 $\times$ 10^3 $\mathrm{ms^{-1}}$ in Se, at 40 $\mathrm{MVm^{-1}}$. At low fields, photon generated carriers immediately form polarons. At high fields, the carriers transport in a ballistic way, likely resulting in impact ionization. By considering polaronic conduction, the model takes into account the molecular structure of the amorphous Se film and attempts to explain avalanche multiplication. This however is still a qualitative model which does not yet consistently explain avalanche multiplication in different allotropes of Se, and in other amorphous semiconductors.

The models discussed above take the Se film as a single bulk, or as an alloyed bulk of Se and As_2Se_3, with As_2Se_3 added for temperature stabilization, without considering the multi-nanolayer structure of the film.

Investigating the multi-layer structure

While it was well established that As incorporated into amorphous Se improved the durability of the film from thermal degradation, there was need to investigate the

specific case of incorporation in the form of a mille-feuille structure [55, 40]. In a comparative study of bulk amorphous Se, bulk of mixed amorphous Se and As_2Se_3, and mille-feuille Se and As_2Se_3, it was confirmed that adding As_2Se_3 improved durability from thermal degradation. Bulk amorphous Se crystallized after about 45 °C annealing temperature, whereas crystalline phases in mixed and multi-layer Se and As_2Se_3 appeared around 85 °C and 105 °C, respectively. Electrical conductivity measurements in dark conditions showed higher currents for the multi-layer films. Photoconductivity was also shown to be higher by an order in the multi-layer films. A study of breakdown current showed reversible breakdown at around 135 MVm^{-1} in multi-layer films, while permanent breakdown occurred in bulk films at higher applied fields [6]. When the multi-layer film was applied as the photo-detecting anode in a vacuum diode photodetector structure driven by nitrogen doped diamond field emitter cold cathode, multiplication gains of up to 4000 were observed. An accumulation of these observations and analysis led to the proposal of the Cascade Multiplication model.

The Cascade Multiplication model considers the multi-layer structure of the Se film, and suggests that the multi-layer arrangement specifically results in carrier multiplication [52]. In this model, the different layers of the multi-layer structure have different roles during the transport of photo-generated charge. The As_2Se_3 were considered as p-type layers wherein the photo-carriers are accelerated by a high field in the film. The amorphous Se layers were considered trapping layers with a high density of filled traps. Cascade multiplication was then a process where photo-generated charge is accelerated in the As_2Se_3 layer, possibly reaching the threshold ionization energy, and then injected into the next amorphous Se layer. The accelerated carrier then excites carriers from the trap levels in the amorphous Se layer, resulting in carrier multiplication. The resulting carriers will then be injected into the next As_2Se_3 layer where they are accelerated. In this way, carrier multiplication cascades along the film thickness. Thus, by creating separate regions of acceleration and collision, carrier multiplication cascades along the sample in the direction of the applied field. Nevertheless, so far,

no physical interpretation with experimental evidence for such electronic property has been presented.

Depending on the thicknesses of the layers of Se and As_2Se_3, the multi-layered arrangement is possibly a superlattice structure. As such, the multi-layered arrangement of the amorphous Se film needs to be investigated in more detail using the physics of superlattices (See Appendix A for a basic review of the theory superlattices). In the proposal of semiconductor superlattices it was predicted that the band structures of the base materials would be perturbed resulting in the superlattice having a unique band structure and consequently altered electronic transport properties like negative differential resistance and resonant tunneling [56, 57]. Furthermore, it was shown that tetrahedrally bonded amorphous materials such as a-Si:H could be fabricated as superlattices, and that the superlattice structure had the effect of stretching the distribution of shallow, weakly localized states in these materials [58, 59, 60]. The superlattice structure should also have an effect on the bands and defect states of the amorphous materials Se and As_2Se_3.

Given that multiplication gain in the multi-layer structure of amorphous Se is key for improving detector sensitivity, it is necessary to understand the electronic properties and charge transport characteristics of the amorphous Se superlattice. We therefore study the fabrication of multi-nanolayer amorphous Se superlattice, and the characterization of its structural, optical and electronic properties.

Chapter 2 discusses the fabrication and characterization of multi-layer films of amorphous Se and As_2Se_3. The process of rotational evaporation is used to fabricate multi-layer films. Results from Time of Flight Secondary Ion Mass Spectroscopy (TOF-SIMS) and Raman spectroscopy are then presented, showing the characterization of the physical properties of the films.

Chapter 3 discusses the energy level structure of amorphous Se superlattice films fabricated using rotational evaporation. Using Deep Level Transient Spectroscopy (DLTS), a comparative study of the individual Se, As_2Se_3, and the multi-nanolayer

structure of the two materials is presented. The discussion reveals trap level modulation and miniband formation associated with quantum superlattice structures.

In Chapter 4, a study of the optical properties is presented. Spectroscopic ellipsometry is used to characterize Se, As_2Se_3 and multi-layer films of the two materials, revealing optical band gap and dielectric function properties of the materials. The multi-nanolayer films show discrete transitions associated with quantum superlattice structures.

A discussion of the electronic transport properties of the multi-nanolayer films is presented in Chapter 5. Oscillations in current-voltage (I-V) characteristics reveal oscillations associated with superlattice structures. A model based on injection, sequential quantum tunneling and impact ionization is presented to explain the observed features.

In Chapter 6, we present a design method developed based on the characterizations discussed in the previous chapters. This design model uses the observed quantum features associated with the multi-nanolayer structure, to optimize the performance of photo-detectors with respect to operating wavelength, required sensitivity and response time.

Chapter 7 is a demonstration of the design method towards developing an X-ray detector. We show that it is possible to design and fabricate an X-ray detector using Ge and superlattice Se, which can be operated successfully at room temperatures and with sensitivities of up to 6688 $\text{pCmGy}^{-1}_{airKERMA}$, comparable to state of the art detectors.

The conclusion summarizes the significance of the work, challenges encountered, future experimental work and possible innovations.

References

[1] O. V. Belyakov, S. A. Mitchell, D. Parikh, G. Randers-Pehrson, S. A. Marino, S. A. Amundson, C. R. Geard, and D. J. Brenner, "Biological effects in unirradiated human tissue induced by radiation damage up to 1 mm away," *Proceedings of the National Academy of Sciences*, vol. 102, no. 40, pp. 14203–14208, 2005.

[2] J. Mirsch, F. Tommasino, A. Frohns, S. Conrad, M. Durante, M. Scholz, T. Friedrich, and M. Löbrich, "Direct measurement of the 3-dimensional DNA lesion distribution induced by energetic charged particles in a mouse model tissue," *Proceedings of the National Academy of Sciences*, vol. 112, no. 40, pp. 12396–12401, 2015.

[3] JART, "Medical Exposure Guideline," Jun 2015.

[4] J. Scheuermann, A. Howansky, A. Goldan, S. Leveille, O. Tousignant, K. Tanioka, and W. Zhao, "MO-AB-BRA-07: Low Dose Imaging with Avalanche Amorphous Selenium Flat Panel Imager," *Medical Physics*, vol. 43, no. 6Part28, pp. 3692–3692, 2016.

[5] S. Kasap, J. Yang, B. Simonson, E. Adeagbo, M. Walornyj, G. Belev, M. P. Bradley, and R. E. Johanson, "Effects of X-ray irradiation on charge transport and charge collection efficiency in stabilized a-Se photoconductors," *Journal of Applied Physics*, vol. 127, no. 8, p. 084502, 2020.

[6] T. Masuzawa, I. Saito, T. Yamada, M. Onishi, H. Yamaguchi, Y. Suzuki, K. Oonuki, N. Kato, S. Ogawa, Y. Takakuwa, A. Koh, D. Chua, Y. Mori, T. Shi-

mosawa, and K. Okano, "Development of an amorphous Selenium-based photodetector driven by a diamond cold cathode," *Sensors*, vol. 13, pp. 13744–13778, Oct 2013.

[7] D. C. Hunt, K. Tanioka, and J. A. Rowlands, "X-ray imaging using avalanche multiplication in amorphous selenium: Investigation of depth dependent avalanche noise," *Medical Physics*, vol. 34, pp. 976–986, Feb 2007.

[8] S. M. Sze, *Physics of semiconductor devices*. Wiley, New York, 1990.

[9] R. H. Bube, *Photovoltaic Materials*. Imperial College Press, London, 1998.

[10] D. A. Neamen, *Semiconductor physics and devices : basic principles*. McGraw-Hill, New York, 2003.

[11] G. Lutz, *Semiconductor Radiation Detectors*. Springer, Berlin, 1999.

[12] J. B. Frey, K. Sadasivam, G. Belev, H. Mani, L. Laperriere, and S. Kasap, "Dark current - voltage characteristics of vacuum deposited multilayer amorphous selenium-alloy detectors and the effect of X-ray irradiation," *Journal of Vacuum Science & Technology A*, vol. 37, no. 6, p. 061501, 2019.

[13] S. Kasap, J. B. Frey, G. Belev, O. Tousignant, H. Mani, J. Greenspan, L. Laperriere, O. Bubon, A. Reznik, G. DeCrescenzo, K. S. Karim, and J. A. Rowlands, "Amorphous and polycrystalline photoconductors for direct conversion flat panel X-ray image sensors," *Sensors*, vol. 11, pp. 5112–5157, May 2011.

[14] M. J. Yaffe and J. A. Rowlands, "X-ray detectors for digital radiography," *Physics in Medicine and Biology*, vol. 42, pp. 1–39, Aug 1997.

[15] G. S. Belev, *Electrical properties of amorphous selenium based photoconductive devices for application in X-ray image detectors*. PhD thesis, Department of Electrical and Computer Engineering, University of Saskatchewan, Saskatoon, SK, Canada, Jan 2007.

[16] S. Kasap and M. Zangahir Kabir, "Photoconductors for X-ray Image Detectors," in *Handbook of Electronic and Photonic Materials*, pp. 1125–1147, Springer US, 2017.

[17] Z. Wei and J. A. Rowlands, "Large-area solid state detector for radiology using amorphous selenium," in *Proceedings SPIE Medical Imaging VI: Instrumentation*, vol. 1651, pp. 1–10, SPIE, 1992.

[18] A. Mehta, "High resistivity amorphous Selenium alloy semiconductors for radiation detection applications.," Master's thesis, Univbersity of South Carolina, 2013. Retrieved from http://scholarcommons.sc.edu/etd/2412.

[19] S. Abbaszadeh, C. C. Scott, O. Bubon, A. R. Reznik, and K. S. Karim, "Enhanced detection efficiency of direct conversion X-ray detector using polyimide as hole-blocking layer," *Nature Scientific Reports*, vol. 3, no. 3360, 2013.

[20] S. Kasap, J. Rowlands, S. D. Baranovskii, and K. Tanioka, "Lucky drift impact ionization in amorphous semiconductors," *Journal of Applied Physics*, vol. 96, pp. 2037–2047, Aug 2004.

[21] G. Juska and K. Arlauskas, "Features of hot carriers in amorphous Selenium," *physica status solidi (a)*, vol. 77, no. 1, pp. 387–391, 1983.

[22] K. Tanioka, "Mechanism of the HARP imaging tube (translated)," *NHK Research News*, vol. 54, pp. 12–17, Jul 1994.

[23] K. Tanioka, "Ultra-high-sensitivity new Super-HARP pickup tube," in *Proc. 2001 IEEE Workshop CCD and Advanced Image Sensors*, pp. 216–219, IEEE, 2001.

[24] Y. Honda, M. Nanba, K. Miyakawa, M. Kubota, M. Nagao, Y. Neo, H. Mimura, and N. Egami, "Electrostatic-focusing image sensor with volcano-structured Spind-type field emitter array," *Journal of Vacuum Science and Technology B*, vol. 34, no. 5, pp. 052201–1–052201–6, 2016.

[25] T. Nakada, T. Sato, Y. Matsuba, K. Sakemura, Y. Okuda, N. Negishi, A. Watanabe, T. Yoshikawa, K. Ogasawara, M. Nanba, K. Tanioka, N. Egami, A. Kobayashi, and N. Koshida, "2/3 in. ultrahigh-sensitivity image sensor with active-matrix high-efficiency electron emission device," *Journal of Vacuum Science and Technology B*, vol. 28, no. 2, pp. C2D11–C2D16, 2010.

[26] N. Negishi, Y. Matsuba, R. Tanaka, T. Nakada, K. Sakemura, Y. Okuda, A. Watanabe, T. Yoshikawa, K. Ogasawara, M. Nanba, S. Okazaki, K. Tanioka, N. Egami, and N. Koshida, "Development of a high-resolution active-matrix electron emitter array for application to high-sensitivity image sensing," *Journal of Vacuum Science and Technology B*, vol. 25, no. 2, pp. 661–665, 2007.

[27] K. Okano, T. Yamada, H. Ishihara, S. Koizumi, and J. Itoh, "Electron emission from nitrogen-doped pyramid-shape diamond and its battery operation," *Applied Physics Letters*, vol. 70, pp. 2201–2203, Apr 1997.

[28] Y. Suzuki, H. Yamaguchi, K. Oonuki, Y. Okamura, and K. Okano, "Amorphous Selenium photodetector driven by diamond cold cathode," *IEEE Electron Device Letters*, vol. 24, no. 1, pp. 16–18, 2003.

[29] N. Kato, I. Saito, H. Yamaguchi, H. Okamura, T. Yamada, T. Butler, N. L. Rupesinghe, G. A. H. Amaratunga, and K. Okano, "Amorphous selenium based photodetector driven by field emission current from N-doped diamond cold cathode," *Journal of Vacuum Science and Technology B*, vol. 24, no. 2, pp. 1035–1039, 2006.

[30] K. Okano, S. Koizumi, S. Ravi, P. Silva, and G. A. J. Amaratunga, "Low-threshold cold cathodes made of nitrogen-doped chemical-vapor-deposited diiamond," *Nature*, vol. 381, pp. 140–141, May 1996.

[31] K. Okano, K. Hoshina, S. Koizumi, and K. Nishimura, "Mold growth of polycrystalline pyramidal-shape diamond for field emitters," *Diamond and Related Materials*, vol. 5, pp. 19–24, Jan 1996.

[32] K. Okano, K. Hoshina, M. Iida, S. Koizumi, and T. Inuzuka, "Fabrication of diamond field emitter array," *Applied Physics Letters*, vol. 64, pp. 2742–2744, May 1994.

[33] Y. Suzuki, K. Oonuki, H. Yamaguchi, Y. Okamura, and K. Okano, "Triode-structure amorphous selenium photodetector driven by diamond cold cathode," *Electronics Letters*, vol. 38, pp. 1–2, Dec 2002.

[34] T. Masuzawa, "Formation of p-n junction in a-Se thin film and its application to high sensitivity photodetector driven by diamond cold cathode," *physica status solidi (a)*, vol. 214, no. 11, pp. 1–7, 2017.

[35] M. Bliss and W. J. Weber, "Radiation detector materials: an overview," *Journal of Materials Research*, vol. 23, pp. 2561–2581, Oct 2008.

[36] Spahn, "X-ray detectors in medical imaging," *Nuclear Instruments and Methods in Physics Research A*, vol. 731, pp. 57–63, Jun 2013.

[37] G. Belev and S. Kasap, "Amorphous selenium as an X-ray photoconductor," *Journal of Non-Crystalline Solids*, vol. 345-346, pp. 484–488, 2004. Physics of Non-Crystalline Solids 10.

[38] J. G. Rocha and S. Lanceros-Mendez, "Review on X-ray detectors based on scintillators and CMOS Technology," *Recent Patents on Electrical Engineering*, vol. 4, pp. 1–26, Sep 2011.

[39] M. Overdick, C. Baumer, K. J. Engel, J. Fink, C. Hermann, H. Kruger, M. Simon, R. Steadman, and G. Zeitler, "Status of direct conversion detectors for medical imaging with X-rays," *IEEE Transactions on Nuclear Science*, vol. 56, pp. 1800–1809, Aug 2009.

[40] I. Saito, T. Masuzawa, Y. Kudo, S. Pittner, T. Yamada, A. T. T. Koh, D. H. C. Chua, Y. Mori, D. R. T. Zahn, G. A. J. Amaratunga, and K. Okano, "Durability and photo-electric characteristics of a millie-feuille structured amorphous selenium (a-Se)-arsenic selenide (As_2Se_3) multi-layered thin film," *Journal of Non-Crystalline Solids*, vol. 378, pp. 96–100, Apr 2013.

[41] F. H. Attix, *Introduction to Radiological Physics and Radiation Dosimetry*. WILEY-VCH Verlag, Weinheim, 2004.

[42] M. J. Berger, J. H. Hubbell, S. M. Seltzer, J. Chang, J. S. Coursey, R. Sukumar, D. S. Zucker, and K. Olsen, "XCOM: Photon Cross Section Database (version 1.5)," *National Institute of Standards and Technology*, 2010.

[43] S. Kasap, J. B. Frey, G. Belev, O. Tousignant, H. Mani, L. Laperriere, A. Reznik, and J. A. Rowlands, "Amorphous selenium and its alloys from early xeroradiography to high resolution X-ray image detectors and ultrasensitive imaging tubes," *physica status solidi (b)*, vol. 246, no. 8, pp. 1794–1805, 2009.

[44] Y. Eisen, A. Shor, and I. Mardor, "CdTe and CdZnTe gamma ray detectors for medical and industrial imaging systems," *Nuclear Instruments and Methods in Physics Research Section A: Accelerators, Spectrometers, Detectors and Associated Equipment*, vol. 428, no. 1, pp. 158–170, 1999.

[45] C. Szeles, "CdZnTe and CdTe materials for X-ray and gamma ray radiation detector applications," *physica status solidi (b)*, vol. 241, no. 3, pp. 783–790, 2004.

[46] O. Semeniuk, O. Grynko, G. Decrescenzo, G. Juska, K. Wang, and A. Reznik, "Characterization of polycrystalline lead oxide for applications in direct conversion X-ray detectors," *Scientific Reports*, vol. 7, pp. 1–10, Aug 2017.

[47] O. Grynko, T. Thibault, E. Pineau, G. Juska, and A. Reznik, "Bilayer lead oxide X-ray photoconductor for lag-free operation," *Scientific Reports*, vol. 10, no. 20117, pp. 1 –9, 2020.

[48] J. A. Rowlands, "Material change for X-ray detectors," *Nature*, vol. 550, pp. 47–48, Oct 2017.

[49] Y. C. Kim, H. Kim, K, D. Son, D. Jeong, J. Seo, I. T. Choi, Y. S. Han, Y. S. Lee, and N. Park, "Printable organometalic perovskite large-area, low-dose X-ray imaging," *Nature*, vol. 550, pp. 87–91, October 2017.

[50] H. Tsai, F. Liu, S. Shrestha, K. Fernando, S. Tretiak, B. Scott, D. T. Vo, J. Strzalka, and W. Nie, "A sensitive and robust thin-film X-ray detector using 2D layered perovskite diodes," *Science Advances*, vol. 6, no. 15, 2020.

[51] K. Tanaka, "A polaronic view of impact ionization in amorphous Se films," *Physica Status Solidi RRL*, vol. 11, pp. 1–3, Nov 2017.

[52] T. Masuzawa, S. Kuniyoshi, M. Onishi, R. Kato, I. Saito, T. Yamada, A. T. Koh, D. H. C. Chua, T. Shimosawa, and K. Okano, "Conditions for a carrier multiplication in amorphous-selenium based photodetector," *Applied Physics Letters*, vol. 102, no. 073506, pp. 1–4, 2013.

[53] W. Shockley, "Problems related to p-n junctions in silicon," *Solid-State Electronics*, vol. 2, no. 1, pp. 35–67, 1961.

[54] B. K. Ridley, "Lucky-drift mechanism for impact ionisation in semiconductors," *Journal of Physics C: Solid State Physics*, vol. 16, pp. 3373–3388, jun 1983.

[55] I. Saito, *Amorphous Selenium Photoelectric Devices*. PhD thesis, Wolfson College, Department of Engineering, University of Cambridge, Cambridge, United Kingdom, Jan 2011.

[56] L. Esaki and R. Tsu, "Superlattice and negative differential conductivity in semiconductors," *IBM Journal of Research and Development*, vol. 14, pp. 61–65, Jan 1970.

[57] L. Esaki and L. L. Chang, "New transport phenomenon in a semiconductor "superlattice"," *Physical Review Letters*, vol. 33, pp. 496–498, Aug 1974.

[58] B. Abeles and T. Tiedje, "Amorphous semiconductor superlattices," *Physical Review Letters*, vol. 51, pp. 2003–2006, Nov 1983.

[59] B. Abeles, "Amorphous semiconductor superlattices," *Superlattices and Microstructures*, vol. 5, pp. 473–480, Jul 1989.

[60] S. Miyazaki, "Amorphous semiconductor superlattices (in Japanese)," *New Glass*, vol. 5, no. 1, pp. 45–56, 1990.

Chapter 2

Material fabrication and characterization

The technologically simple method of rotational evaporation was used to fabricate multi-layer films of Se and As_2Se_3. The material distribution in the films was characterized by depth profiling using Time of Flight Secondary Ion Mass Spectroscopy (TOF-SIMS). Raman spectroscopy was used to characterize the phase state of the individual materials, and of the multi-layer structures.

2.1 Fabrication

Using the rotational evaporation technique, samples of the individual materials, namely amorphous Se only, As_2Se_3 only, and the multi-layer combination of the two materials in 1:1 ratio by volume, were fabricated [1]. The substrates were n-type Si (100), 5 - 8 Ω·cm, single side polished wafers diced into 10 mm squares. The Si substrates were cleaned in an ultrasonic bath using acetone, methanol, and deionized water, before being submerged in 25 % diluted HF to remove the surface oxide. The cleaned Si substrates were then attached to circular glass holders and placed into the rotational evaporation system, with the polished surface as the target for deposition. The evaporation chamber was immediately pumped to high vacuum. The schematic of the rotational evaporator is shown in Fig. 2.1.

When the target chamber pressure of 10^{-6} Torr was reached, the turntable holding the substrates was rotated at 80 rpm. Single bulk material samples (As_2Se_3 only and Se only) were deposited using one boat at a time. The sources were granulated As_2Se_3 (STREM Chemicals 5N purity, 0.5 mm diameter grains) and Se pellets (Nilaco 5N purity, 1 mm pellets), respectively. The multi-layer films were fabricated by having both boats heated such that alternating layers of Se and As_2Se_3 were evaporated and deposited onto the Si substrates. The deposition thickness was measured using a crystal oscillator which traced the same circular path as the samples. Individual samples had a target thickness of 1 μm while the target total thickness of the multi-layer film was 2 μm.

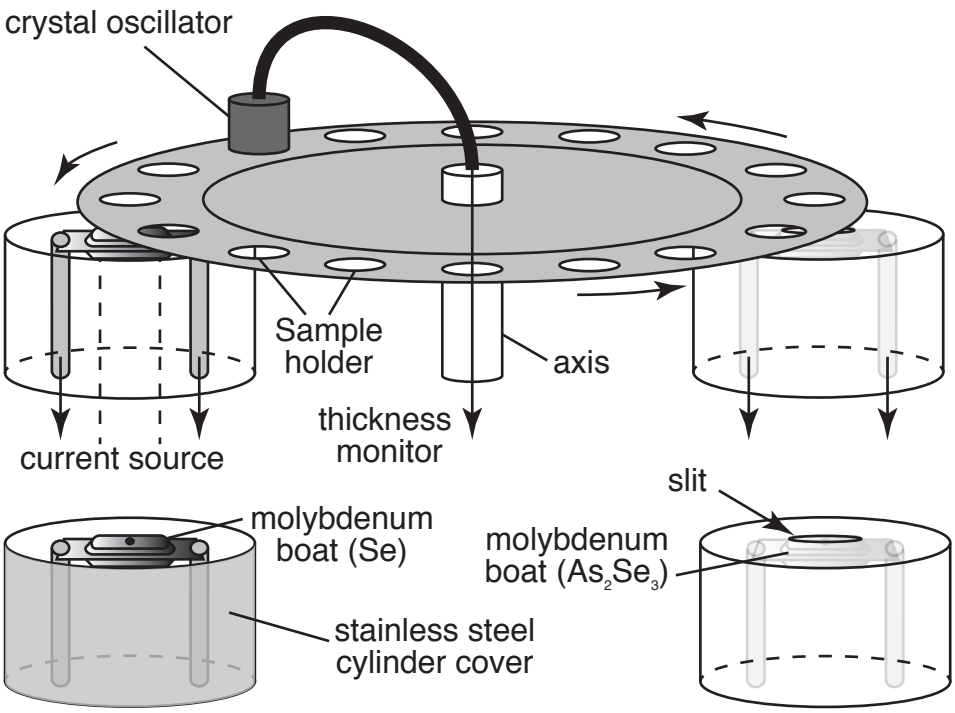

Figure 2.1: The schematic of the rotational evaporation system. The substrates were placed on a turntable such that they alternately passed over heated boats containing evaporating Se and As_2Se_3. A crystal oscillator traced the same path as the substrates and measured the deposited thickness.

2.2 Time Of Flight Secondary Ion Mass Spectroscopy (TOF-SIMS)

The depth profile of superlattice Se samples was evaluated using TOF-SIMS on the ION-TOF TOF.SIMS5 system [1, 2]. The measurement was performed by alternating sputtering the film surface using a Cs beam, and irradiating with a Ga primary ion beam. The analysis beam covered a spot size of 100 μm square and the sputtering etch area was 200 μm square, with both beams irradiated alternately for 4 s. For the analysis beam, the acceleration voltage was 1 kV at a current of 4 nA. A 200 nm superlattice Se sample was used for the TOF-SIMS and the results of the measurements are shown in Fig. 2.2. From the TOF-SIMS result, it is possible to estimate the thickness of each superlattice layer. For the peaks shown in Fig. 2.2, a Gaussian fit was applied as shown in Fig. 2.3, and the thickness determined from the Full Width at Half Maximum (FWHM). The FWHM gave values of thickness from 6 - 9 nm. These values agree with estimates made from the rotational speed and duration of deposition, and with measurements from previous work [1]. The result confirms that across the deposition thickness, there are alternating layers of Se and As_2Se_3 with a period of 12 - 18 nm. Since these materials have different dielectric constant, and consequently band gap an energy band distribution can also be inferred, as shown in Fig. 2.4. The energy band structure suggests the formation of a series of nanometer size quantum wells such that the deposited structure can thus be considered as a superlattice [3]. The conditions for a superlattice are that the period is of the order of 10 nm, and the periodic potential is greater than 0 eV [3]. We used the de Broglie wavelength to check if the fabricated nanolayer structures qualify as quantum devices [4]. The de Broglie wavelength is

$$\lambda_{deBroglie} \approx \frac{h}{\sqrt{m^* k_B T}} \tag{2.1}$$

where h is the Planck's constant, k_B is the Boltzmann constant, T is the temperature in kelvin, and m^* is the carrier effective mass. For As_2Se_3 quantum well, with effective

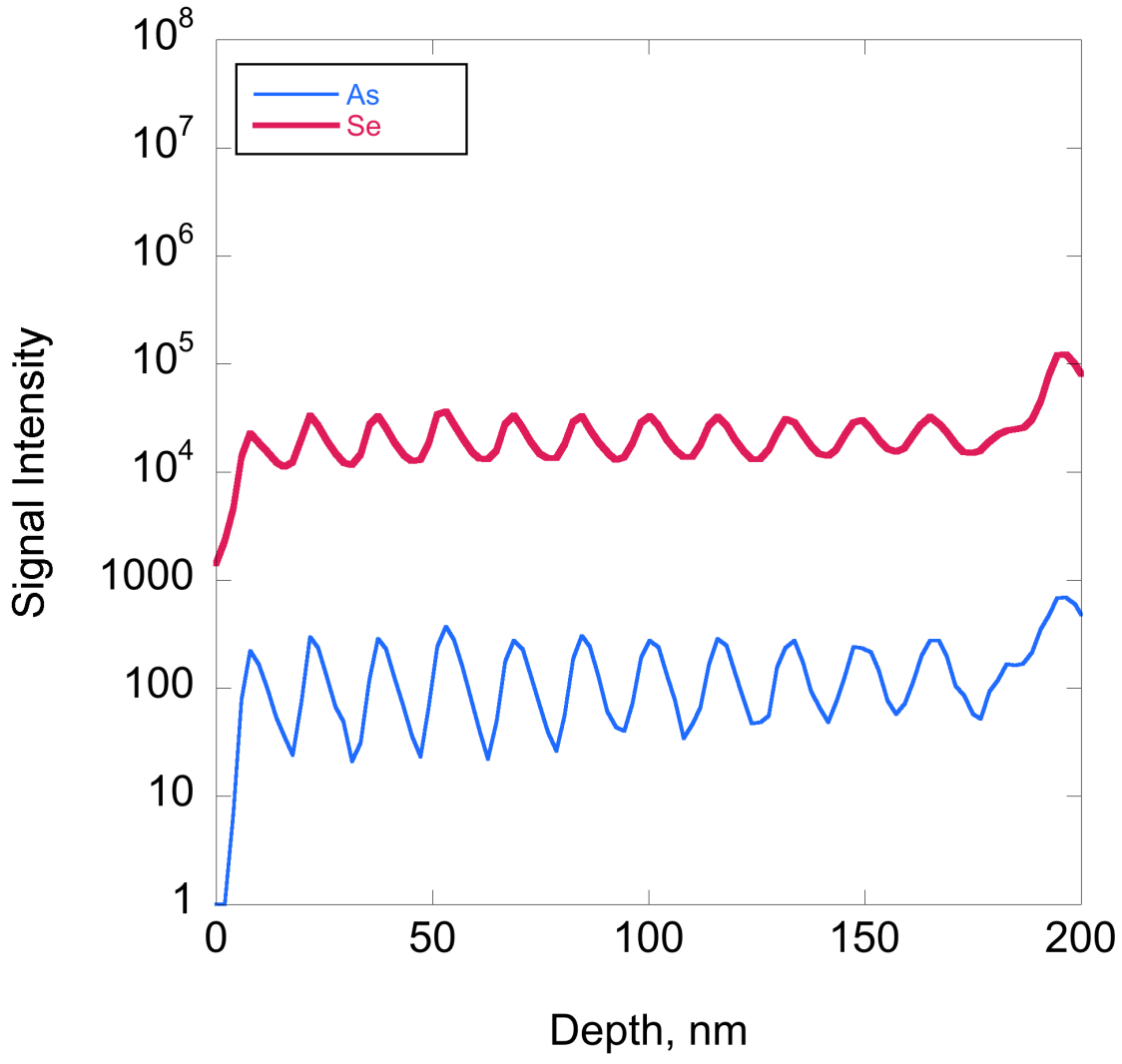

Figure 2.2: The results of the TOF-SIMS measurement of 200 nm film of superlattice Se showing the layered distribution of Se and As.

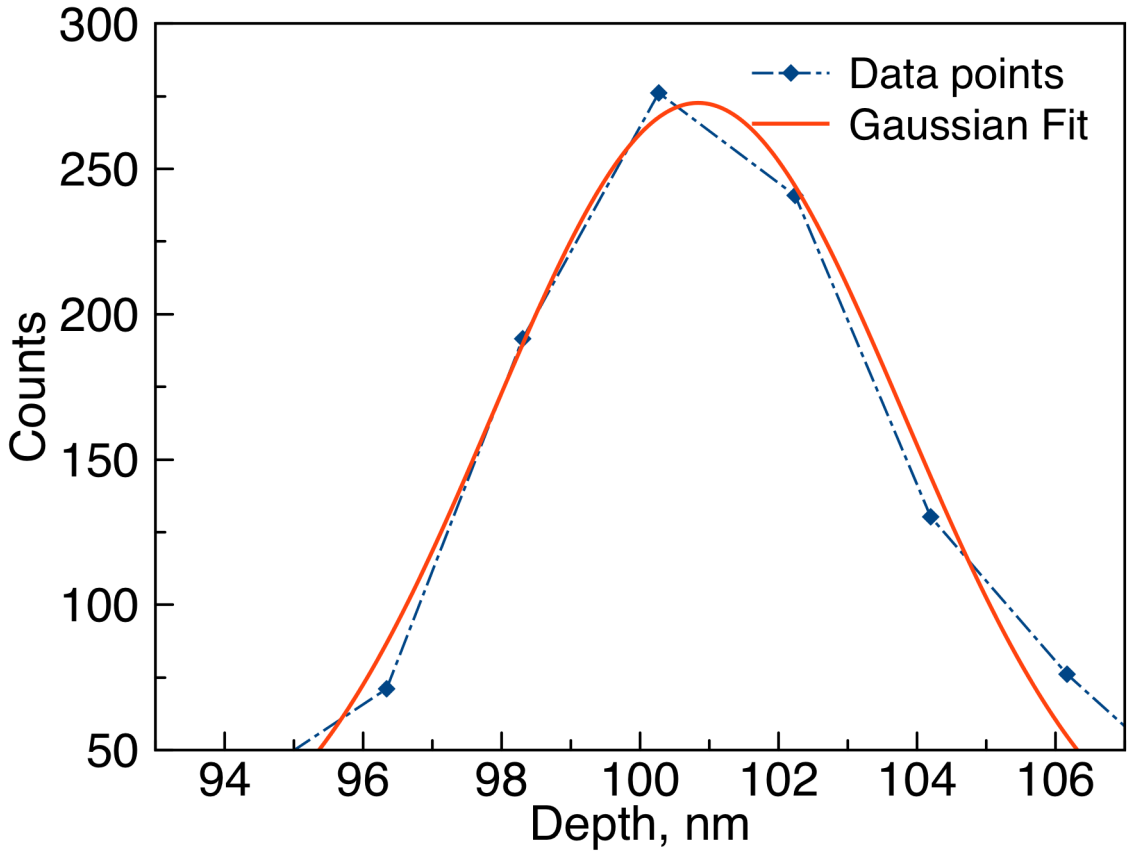

Figure 2.3: A single peak from the results shown in Fig. 2.2 fitted with a Gaussian curve. Analysis of the peaks using the Gaussian fit showed Full Width at Half Maximum (FWHM) values of 6 - 9 nm.

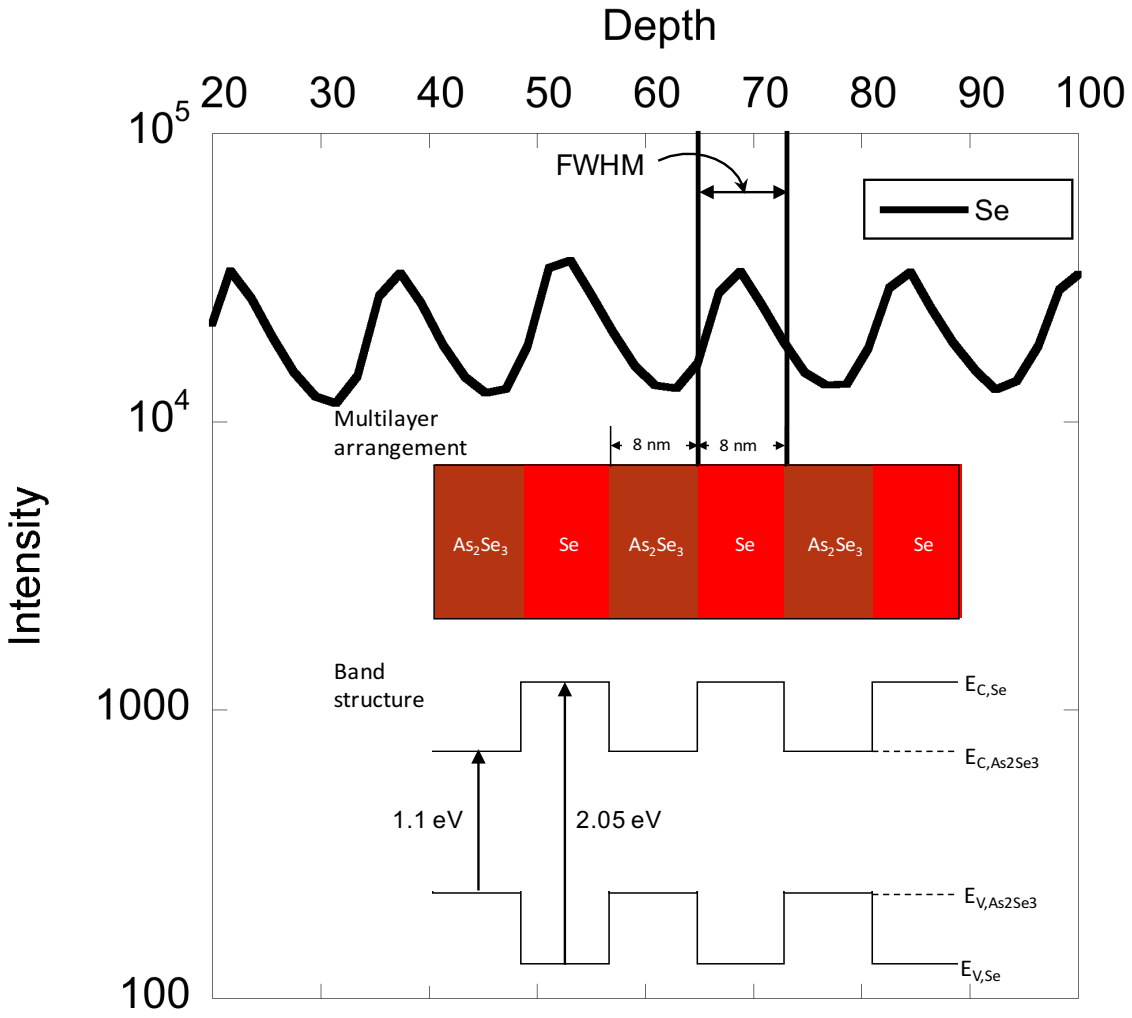

Figure 2.4: Se component measured using TOF-SIMS with illustrations below showing the material distribution and energy band distribution. On average, each layer of Se and As_2Se_3 is 8 nm.

electron and hole masses of 0.27 and 0.28, respectively [5], at 300 K, $\lambda_{deBroglie} \approx 21$ nm. Thus for superlattice periods of 12 - 18 nm measured from TOF-SIMS the layer thicknesses are within the expected order for superlattice quantum structures. The energy levels and wave-functions for this periodic structure can be calculated from the Kronig-Penney model, which is reviewed in Appendix A.

2.3 Raman spectroscopy

The three types of samples were measured using Raman spectroscopy using an Andor LBP100 system. The excitation laser was a helium-neon continuous wave (He-Ne CW) laser with emission line of 638.2 nm and power set to 2 mW. All samples were measured at room temperature and pressure conditions. The results are shown in Fig. 2.5.

Fig. 2.5 a) shows the Raman spectrum of amorphous As_2Se_3 sample as indicated by a broad band asymmetric and skewed to the lower frequency side with a maximum around 225 cm^{-1} [6]. The maximum is attributed to stretching vibrations of $AsSe_3$ pyramidal units, with other parts of the spectrum contributed by the presence of structural units of As_4Se_4 (205 cm^{-1}), As_4Se_3 (237 cm^{-1}), Se_8 rings (252 cm^{-1}), and Se_n chains (238 cm^{-1} and 255 cm^{-1}) [7]. Since the spectrum of crystalline As_2Se_3 is known to have narrow peaks, we could confirm the amorphous nature of the samples [6].

In Fig. 2.5 b) the spectrum of amorphous Se is shown. The spectrum has a broad peak skewed towards the higher-frequency side with a maximum around 255 cm^{-1}. The maximum originates predominantly from Se_8 rings with other parts of the spectrum coming from Se_n chains. Again we could confirm the amorphous nature of the Se samples since they can be clearly contrasted with crystalline/trigonal Se spectra which have a narrow peak at 235 cm^{-1} [1].

The results of the Raman measurements of the superlattice Se are shown in Fig. 2.5 c). The spectrum also shows a broad, higher-frequency side skewed peak with a maximum around 250 cm^{-1}. A small shoulder around 225 cm^{-1} is observed indicating the

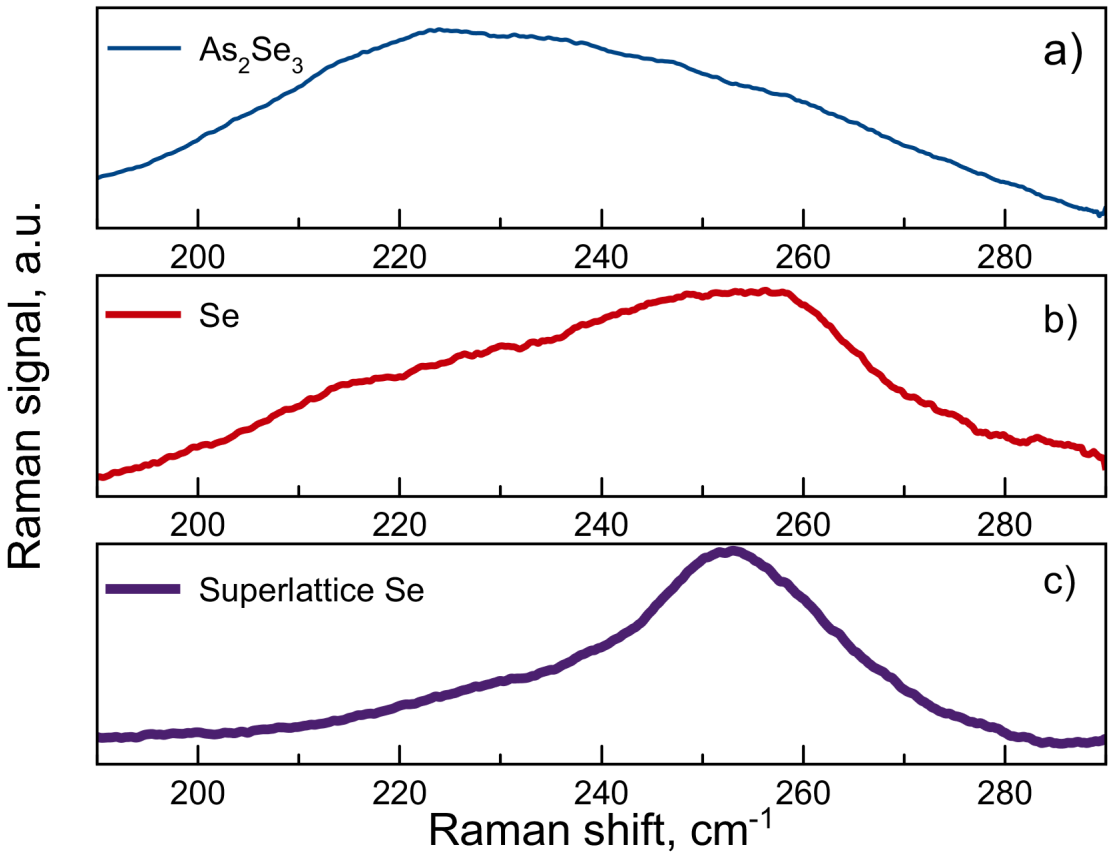

Figure 2.5: Raman spectra for a) amorphous As_2Se_3 showing a broad band with a maximum around 225 cm^{-1}, b) amorphous Se showing a broad band with maximum around 255 cm^{-1}, and c) superlattice-Se showing a broad peak with maximum around 250 cm^{-1}. The broad bands indicate the amorphous nature of the samples.

presence of As-Se structures, most likely $AsSe_3$ pyramidal units. However, the largest contribution is due to Se_8 rings and Se_n chains. From the deposition conditions and TOF-SIMS results, both Se and As_2Se_3 have equal layer thicknesses, which implies that there is overstoichiometry of Se in the sample. Since no narrow peaks were observed we confirmed that the superlattice Se samples have an amorphous nature.

Using rotational evaporation we could fabricate films with alternating layers of Se and As_2Se_3. The multi-layer distribution of materials in the films could be confirmed using TOF-SIMS characterization. Analysis of the results showed that the multi-layers were 6 - 9 nm thick, and based on an estimation using de Broglie wavelength, could be quantum structures. Raman spectroscopy was used to confirm the phase state of the films, with the multi-layer films exhibiting an amorphous state. In this way, we successfully fabricated amorphous superlattice structures using rotational evaporation of amorphous Se and amorphous As_2Se_3, from a physical distribution point of view. As is discussed in Appendix A, due to quantum size effects, superlattices also exhibit unique energy band structure, optical transitions and carrier transport properties. We investigated these properties using Deep Level Transient Spectroscopy (DLTS), spectroscopic ellipsometry, and current-voltage (I-V) and current-time (I-V) characterization.

References

[1] I. Saito, T. Masuzawa, Y. Kudo, S. Pittner, T. Yamada, A. T. T. Koh, D. H. C. Chua, Y. Mori, D. R. T. Zahn, G. A. J. Amaratunga, and K. Okano, "Durability and photo-electric characteristics of a millie-feuille structured amorphous selenium (a-Se)-arsenic selenide (As_2Se_3) multi-layered thin film," *Journal of Non-Crystalline Solids*, vol. 378, pp. 96–100, Apr 2013.

[2] I. Saito, W. Miyazaki, M. Onishi, Y. Kudo, T. Masuzawa, T. Yamada, A. Koh, D. Chua, K. Soga, M. Overend, M. Aono, G. A. J. Amaratunga, and K. Okano, "A transparent ultraviolet triggered amorphous selenium p-n junction," *Applied Physics Letters*, vol. 98, p. 152102, Apr 2011.

[3] L. Esaki and R. Tsu, "Superlattice and negative differential conductivity in semiconductors," *IBM Journal of Research and Development*, vol. 14, pp. 61–65, Jan 1970.

[4] P. Blood, *Optical transitions in quantum wells*. Oxford: Oxford University Press, 2015.

[5] E. Antonelli, A. Tarnow and J. D. Joannopoulos, "New insight into the electronic structure of As_2Se_3," *Physical Review B*, vol. 33, pp. 2968–2971, Feb 1986.

[6] Y. Azhniuk, V. Dzhagan, D. Solonenko, V. Loya, I. Grytsyshche, V. Lopushansky, A. Gomonnai, and D. R. Zahn, "In-doped As2Se3 thin films studied by Raman and X-ray photoelectron spectroscopies," *Applied Surface Science*, vol. 471, pp. 943 – 949, 2019.

[7] K. Okano, I. Saito, T. Mine, Y. Suzuki, T. Yamada, N. Rupesinghe, G. A. J. Amaratunga, W. I. Milne, and D. R. T. Zahn, "Characterizations of a-Se based photodetectors using X-ray photoelectron spectroscopy and Raman spectroscopy," *Journal of Non-Crystalline Solids*, vol. 53, pp. 308–312, Jan 2007.

Chapter 3

Energy level structure of Se, As_2Se_3 and superlattice amorphous Se *

*This chapter is based on the following publication:
John, J. D., et al., "Observation of two-level defect system in amorphous Se superlattices." **Applied Physics Letters**, 2020, 116(19), 192104. https://aip.scitation.org/doi/10.1063/5.0004570

3.1 Introduction

Well known for its ultra-high sensitive photo-detection capabilities, amorphous Se is one of the main candidates for envisioned low-dose ultra-high sensitive X-ray imagers for medical applications [1, 2]. Recently it was pointed out that innovation in materials is essential towards reaching low-dose X-ray imaging, with perovskite material demonstrated as a promising candidate [3, 4]. The effectiveness of perovskites stems from the unique arrangement of different material atoms. Multi-material multi-layer amorphous Se based structures have already been successfully applied in a High-gain Avalanche Rushing Photoconductor (HARP) camera [5]. Recently, high photo-detector quantum efficiencies for visible and UV photons were reported for amorphous Se based photoconductors in vacuum photo-detectors driven by low-threshold field emission from nitrogen-doped diamond [6, 7]. The ultra-sensitive performance of these devices is attributed to avalanche multiplication described by models like the Lucky Drift, Polaronic-Supersonic Transformation, and Cascade Multiplication [8, 9, 10, 11]. In this set of models, only Cascade Multiplication considers the multi-layer structure of the Se film, with the other two taking the Se film as an alloyed bulk of Se and As_2Se_3, with As_2Se_3 added for temperature stabilization. However, Cascade Multiplication suggests that the multi-layer arrangement specifically results in carrier multiplication by creating separate regions of acceleration and collision. A comparative study of bulk Se and the multi-layer structure showed that the multi-layer structure had significantly higher photoconductivity [12]. So far, no physical interpretation with experimental evidence for such electronic property has been presented.

Depending on the thicknesses of the layers of Se and As_2Se_3, the multilayered arrangement is possibly a superlattice structure. As such, the multilayered arrangement of the amorphous Se film needs to be investigated in more detail using the physics of superlattices. In the proposal of semiconductor superlattices it was predicted that the band structures of the base materials would be perturbed resulting in the superlattice having a unique band structure and consequently altered electronic transport proper-

ties like negative differential resistance and resonant tunneling [13, 14]. Furthermore, it was shown that tetrahedrally bonded amorphous materials such as a-Si:H could be fabricated as superlattices, and that the superlattice structure had the effect of stretching the distribution of shallow, weakly localized states in these materials [15, 16]. The superlattice structure should also have an effect on the bands and defect states of the amorphous materials Se and As_2Se_3. Using the technically simple method of rotational thermal evaporation, we fabricated a multi-nanolayer superlattice of the two materials and studied the effect on the electronic band-gap states using Deep Level Transient Fourier Spectroscopy (DLTFS). A basic review of DLTFS is presented in Appendix B.

3.2 Results and Discussion

Three types of samples, As_2Se_3 only and amorphous Se only and the multi-layer combination of the two materials, were fabricated on n-type Si substrates using a rotational evaporation system as discussed in Chapter 2 [17]. The depth profile of samples with alternating layers of Se and As_2Se_3 (hereafter referred to as superlattice Se) was characterized using Time of Flight Secondary Ion Mass Spectroscopy (TOF-SIMS). The details of the TOF-SIMS characterization and analysis are found in literature and reviewed in Chapter 2 [12, 17, 18]. The Full Width at Half Maximum (FWHM) values of the peaks showed a layer thickness in the range of 6 - 9 nm for each layer, in agreement with previous estimates [12] and with basic evaluation from deposition rotation speeds and duration. This shows that across the deposition thickness there is a layered distribution of materials with different dielectric constants and consequently a periodically varying energy gap E_G, with a period of 12 - 18 nm. This period is within the order of 10 nm, which is within the threshold condition of so called superlattice structures [13]. The other condition is that the periodic potential must be greater than 0 eV. To determine the periodic potential, the Anderson's rule was used [19]. For amorphous Se, the mobility gap is 2.05 eV [20], and the Fermi level determined from Ultraviolet Photoelectron Spectroscopy (UPS) is about $E_{V,Se} + 0.8$ eV within ± 0.1 eV, in close

agreement to values reported in literature [21]. The electrical band gap of As_2Se_3 is 1.1 eV, with the Fermi level taken to be at the mid-gap [22, 23, 24, 25].

The energy of defect states and how they are affected by "superlatticing" was then investigated using DLTFS. Three types of samples were measured: 1 μm thick As_2Se_3, 1 μm thick amorphous Se and 2 μm thick superlattice Se. These samples were fabricated on n-type Si substrate using rotational evaporation as described before. A top contact of solidified silver paste was placed on the film surface, with Al foil contact attached to n-type Si side also using silver paste. This sample structure was then connected as the device under test on the FT1030 HERA DLTFS system. The sample structure and measurement schematic are shown in Fig. 3.1.

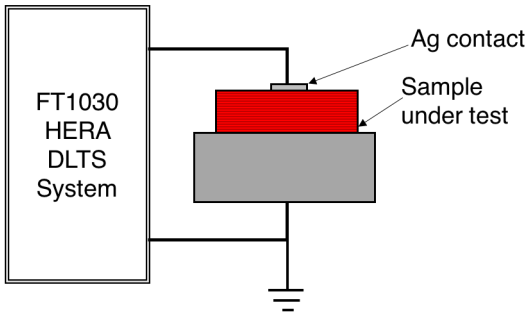

Figure 3.1: The connection of samples under test to the FT1030 HERA DLTFS system. Three types of samples were tested: 1 μm thick As_2Se_3, 1 μm thick amorphous Se, and 2 μm thick superlattice-Se.

The measurement was performed under dark conditions with a temperature scan from 130 K to 300 K in a liquid nitrogen (LN2) temperature regulator (AME tc-2091). The upper temperature limit was chosen to stay below the glass transition temperature of amorphous Se of about 318 K [26]. An initial capacitance-voltage C-V measurement was taken for each sample type to determine the choice of the reverse bias and peak voltages. The reverse voltage V_R was set to +5 V for As_2Se_3 samples, and −5 V for amorphous Se and superlattice Se samples. These directions of bias suggest that As_2Se_3 has n-type conduction and Se has p-type conduction, agreeing with observations in literature [11, 17, 27]. The pulse voltage was set at 0 V, with a time window T_W of

20.48 ms. The resulting DLTFS spectra and Fourier coefficients are shown in Fig. 3.2 and Fig. 3.3 respectively.

The DLTFS Fourier coefficients were used to calculate the time constants and Arrhenius plots following the direct evaluation methods detailed in Appendix B [28, 29]. Here, the Arrhenius equation is

$$\ln(\tau T^2 C) = \frac{(E_C - E)}{k_B}\frac{1}{T} - \ln\sigma \tag{3.1}$$

where T is the temperature, $C = \frac{v_{th}N_C}{T^2}$, v_{th} is thermal velocity, N_C is the density of states, $E_C - E$ is the energy difference between the energy level and the conduction band, k_B is the Boltzmann constant and σ is the capture cross section. The time constant τ is obtained from the Fourier coefficients a_n, and b_n, obtained from a Fourier transformation of the capacitance transient. Figure 3.3 shows coefficients a_1, a_2, and b_1 and b_2 obtained for the three samples As_2Se_3, amorphous Se, and superlattice Se. There are three possible combinations of the coefficients that give the time constants [29]:

$$\tau(a_n, a_k) = \frac{1}{\omega}\sqrt{\frac{a_n - a_k}{k^2 a_k - n^2 a_n}} \tag{3.2}$$

$$\tau(b_n, b_k) = \frac{1}{\omega}\sqrt{\frac{kb_n - nb_k}{k^2 nb_k - n^2 kb_n}} \tag{3.3}$$

$$\tau(a_n, b_n) = \frac{1}{n\omega}\frac{b_n}{a_n} \tag{3.4}$$

where $\omega = \frac{1}{T_W}$. Since the maxima of of the different coefficients are displaced relative to each other, we chose the coefficients which were likely to have the least effect on each other. We therefore used $\tau(a_1, a_2)$ to evaluate levels at higher temperatures, and $\tau(b_1, b_2)$ for levels at lower temperatures. These time constants were then substituted into the Arrhenius plots.

A linear model in terms of $1/T$ was used to fit the Arrhenius plots using linear regression, from which the slope was used to calculate the energy levels. The results

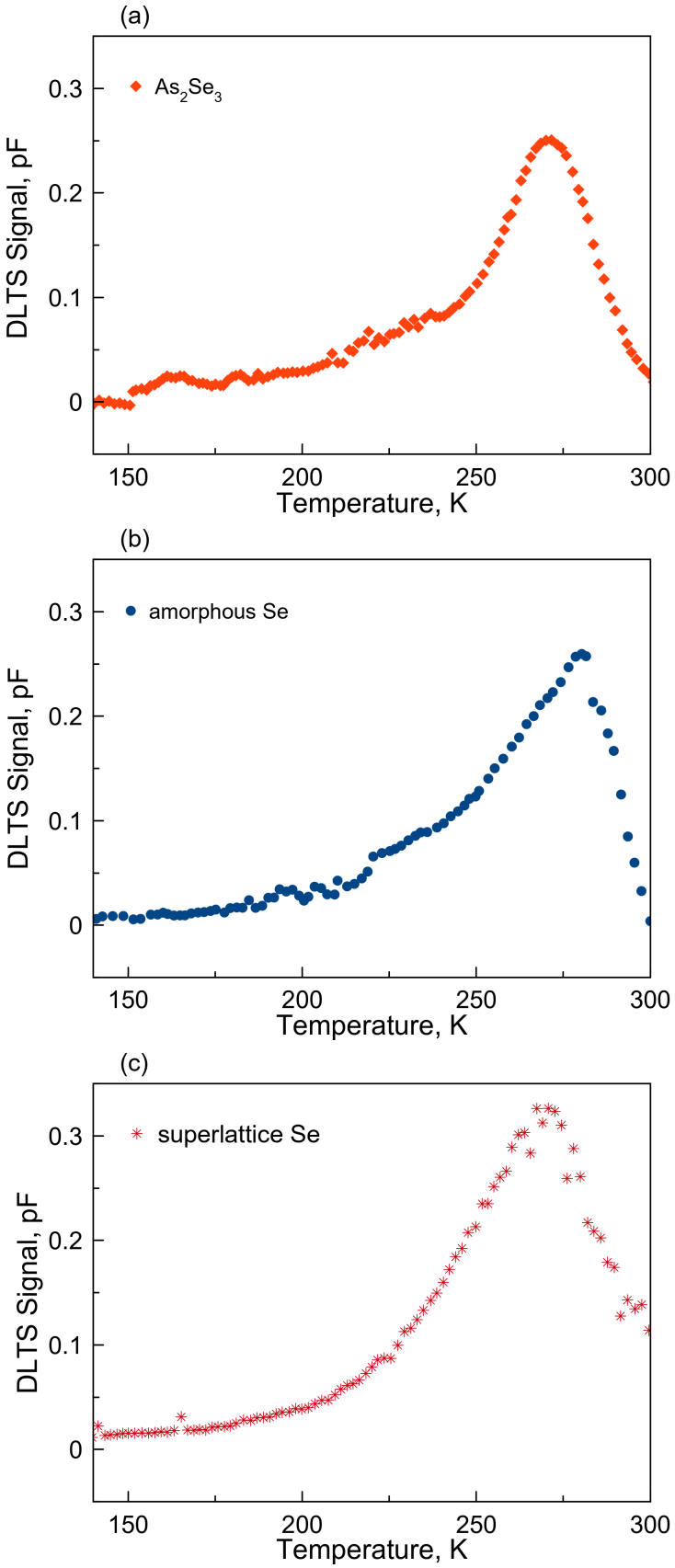

Figure 3.2: The DLTFS spectra of (a) As_2Se_3 (b), amorphous Se, and (c) superlattice Se over the temperature range 130 K t0 300 K.

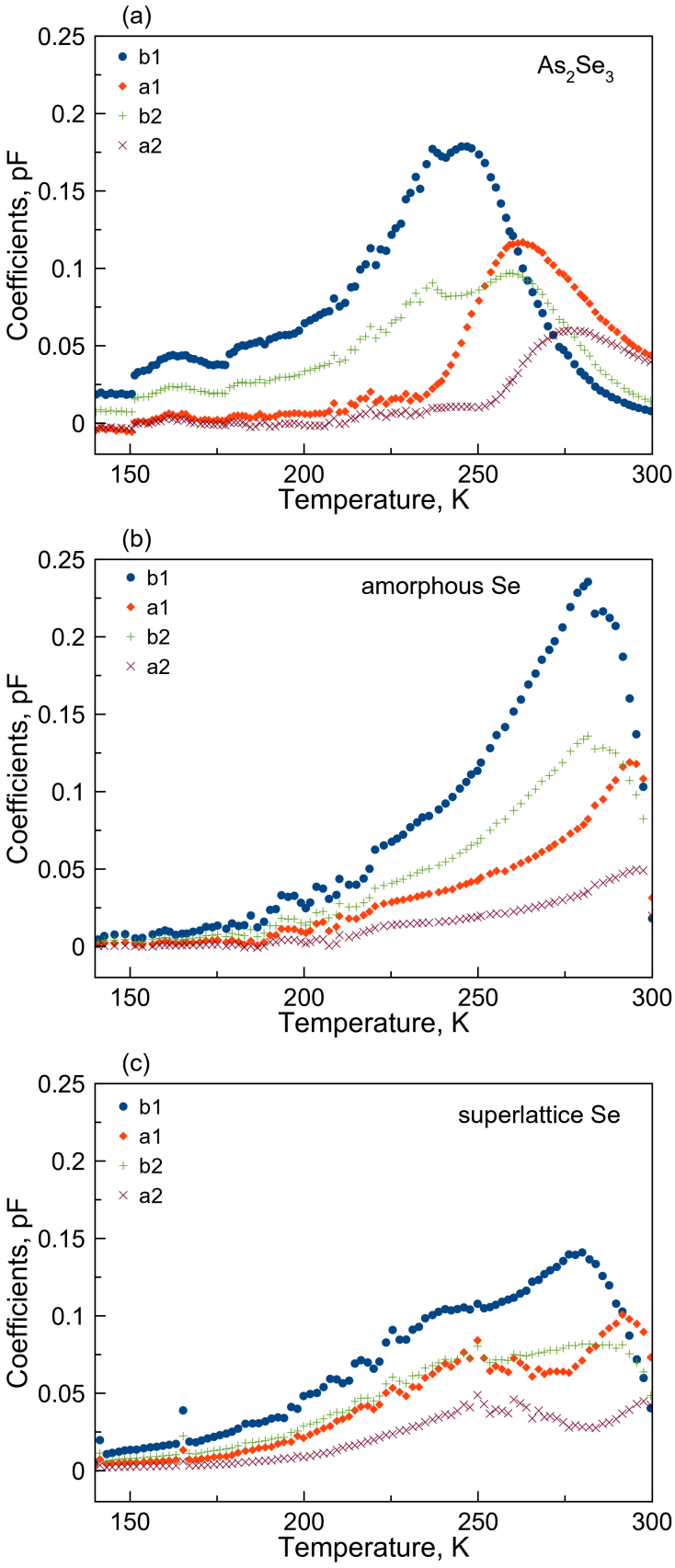

Figure 3.3: The Fourier coefficient spectra of (a) As_2Se_3, (b) amorphous Se, and (c) superlattice Se. These coefficients a_1, a_2, b_1 and b_1 were used to calculate the transient time constants.

of the evaluations are shown in Fig. 3.4. The energy levels observed for each material sample are visualized in band diagrams in Fig. 3.5.

The trap levels measured for As_2Se_3 are comparable to those reported in references [24, 30]. Amorphous Se showed three levels in close agreement with observations reported in literature [31, 32]. For the chalcogen Se and chalcogenide As_2Se_3, these energy levels are associated with valence alternating pairs (VAP) and intimate valence alternating pairs (IVAP) energy states of the C_3^+ and C_1^- coordination defects described by the MDS (Mott, Davis and Street) and KAF (Kastner, Adler and Friztsche) models [25, 33, 34]. In comparison, the superlattice-Se superlattice only exhibits two levels at $E_{C,Se} - 0.5330$ eV and $E_{V,Se} + 0.269$ eV. These are assigned to the minibands resulting from the superlattice structure.

The superlattice resulted in the shifting and aggregation of the defect energy states of each material into two levels seen in the superlattice Se structure. This shifting is attributed to the perturbation of each material's band structure by the alternating periodic arrangement of bands, which creates a new potential variation over the potentials from each material's energy bands. Our result shows that the superlattice potential has a localizing effect, not only on shallow states near the band edges as previously reported [15, 16], but also on deep states. The superlattice imposes an overarching order to the amorphous structure of each material. While amorphous materials have no well-defined wave-vector dependence [9], the periodic structure introduces a superlattice wave-vector and consequently, minibands which depend on the periodic potential [35]. In this way the superlattice modulates the energy levels found in each individual material resulting in trap levels being reduced to only two minibands below and above the mid-gap energy.

For the superlattice, a calculation of the energy levels based on the Kronig-Penney model predicts the presence of five energy levels in the quantum wells for electrons and three for holes. However, these energy levels where not observed in the DLTFS measurement. The filling pulse level at -5 V and the pulse duration may have been

p

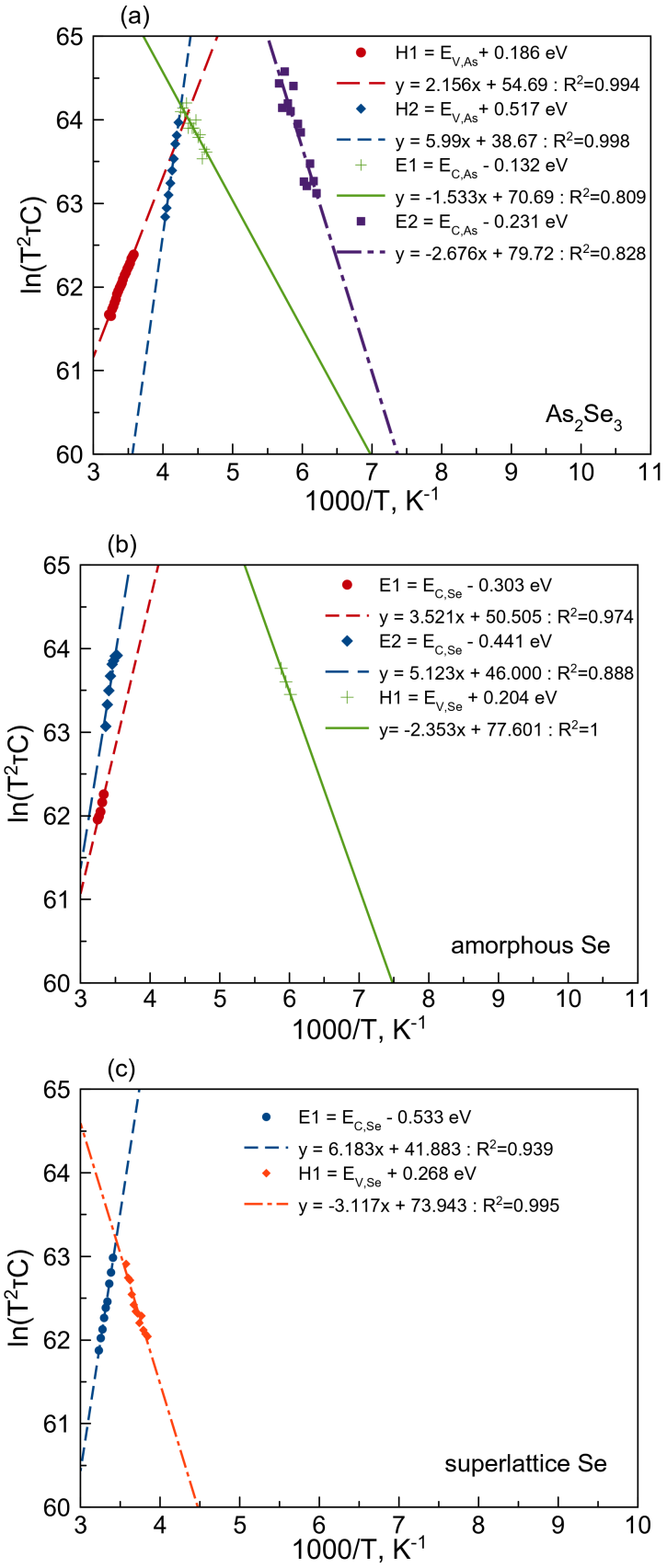

Figure 3.4: The Arrhenius plots obtained from the spectra of (a) As_2Se_3, (b) amorphous Se, and (c) superlattice-Se, modeled by linear fit lines with slopes used to calculate the energy levels.

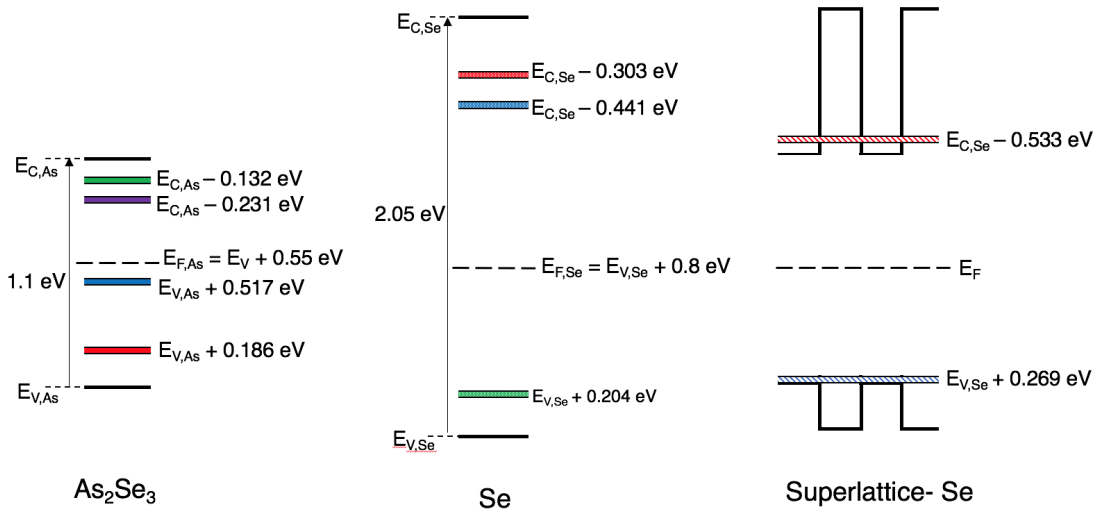

Figure 3.5: The energy levels in the band gaps of As_2Se_3, amorphous Se, and superlattice-Se.

sufficient to fill only the lowest energy levels. By changing the pulse level and time, it may be possible to observe higher energy levels. Additionally, photogeneration may also be applied as a filling pulse in a form of photo-DLTFS, allowing possible observation of higher energy levels. Nevertheless, even under the conditions in this experiment we could demonstrate the effect of multi-layering on the energy levels structure and show quantum superlattice effects.

3.3 Conclusion

To summarize, we investigated the arrangement of defects states in the band gap of chalcogenide material As_2Se_3 and chalcogen amorphous Se, and their arrangement in a superlattice. We showed that superlattice Se can be fabricated using multi-source rotational evaporation, a result which was confirmed in TOF-SIMS measurements. These three materials were then evaluated using DLTFS to measure the energy states in the band gap. The results show that the superlattice arrangement results in the modulation of multiple energy states in each individual material to minibands in the superlattice. From the results we could clarify the phenomena behind some exceptional

performances of superlattice Se based devices. The clarity is essential in the design of other Se based devices, with particular interest focused on ultra-sensitive X-ray detectors that could be used with lower doses than in present systems. There are also potential applications of Se based photo-detectors in spectroscopy systems such as Inverse Photoelectron Spectroscopy (IPES) which require inherent signal amplification and wide spectral sensitivity.

Beyond just Se superlattices, we envision that superlattices of amorphous materials could be a way to control the distributions of energy states that result from the material disorder. Furthermore, such systems seem to allow fabrication at lower technological thresholds using simple methods such as rotational evaporation. We anticipate that this work will inspire more investigations into the fabrication, characterization, and application of superlattices of amorphous materials.

References

[1] M. J. Yaffe and J. A. Rowlands, "X-ray detectors for digital radiography," *Physics in Medicine and Biology*, vol. 42, pp. 1–39, Aug 1997.

[2] S. Kasap and M. Zangahir Kabir, "Photoconductors for X-ray Image Detectors," in *Handbook of Electronic and Photonic Materials*, pp. 1125–1147, Springer US, 2017.

[3] J. A. Rowlands, "Material change for X-ray detectors," *Nature*, vol. 550, pp. 47–48, Oct 2017.

[4] Y. C. Kim, H. Kim, K, D. Son, D. Jeong, J. Seo, I. T. Choi, Y. S. Han, Y. S. Lee, and N. Park, "Printable organometalic perovskite large-area, low-dose X-ray imaging," *Nature*, vol. 550, pp. 87–91, October 2017.

[5] K. Tanioka, "Ultra-high-sensitivity new Super-HARP pickup tube," in *Proc. 2001 IEEE Workshop CCD and Advanced Image Sensors*, pp. 216–219, IEEE, 2001.

[6] T. Masuzawa, "Formation of p-n junction in a-Se thin film and its application to high sensitivity photodetector driven by diamond cold cathode," *physica status solidi (a)*, vol. 214, no. 11, pp. 1–7, 2017.

[7] K. Okano, S. Koizumi, S. Ravi, P. Silva, and G. A. J. Amaratunga, "Low-threshold cold cathodes made of nitrogen-doped chemical-vapor-deposited diiamond," *Nature*, vol. 381, pp. 140–141, May 1996.

[8] K. Tanioka, "Mechanism of the HARP imaging tube (translated)," *NHK Research News*, vol. 54, pp. 12–17, Jul 1994.

[9] S. Kasap, J. Rowlands, S. D. Baranovskii, and K. Tanioka, "Lucky drift impact ionization in amorphous semiconductors," *Journal of Applied Physics*, vol. 96, pp. 2037–2047, Aug 2004.

[10] K. Tanaka, "A polaronic view of impact ionization in amorphous Se films," *Physica Status Solidi RRL*, vol. 11, pp. 1–3, Nov 2017.

[11] T. Masuzawa, S. Kuniyoshi, M. Onishi, R. Kato, I. Saito, T. Yamada, A. T. Koh, D. H. C. Chua, T. Shimosawa, and K. Okano, "Conditions for a carrier multiplication in amorphous-selenium based photodetector," *Applied Physics Letters*, vol. 102, no. 073506, pp. 1–4, 2013.

[12] I. Saito, T. Masuzawa, Y. Kudo, S. Pittner, T. Yamada, A. T. T. Koh, D. H. C. Chua, Y. Mori, D. R. T. Zahn, G. A. J. Amaratunga, and K. Okano, "Durability and photo-electric characteristics of a millie-feuille structured amorphous selenium (a-Se)-arsenic selenide (As_2Se_3) multi-layered thin film," *Journal of Non-Crystalline Solids*, vol. 378, pp. 96–100, Apr 2013.

[13] L. Esaki and R. Tsu, "Superlattice and negative differential conductivity in semiconductors," *IBM Journal of Research and Development*, vol. 14, pp. 61–65, Jan 1970.

[14] L. Esaki and L. L. Chang, "New transport phenomenon in a semiconductor "superlattice"," *Physical Review Letters*, vol. 33, pp. 496–498, Aug 1974.

[15] B. Abeles and T. Tiedje, "Amorphous semiconductor superlattices," *Physical Review Letters*, vol. 51, pp. 2003–2006, Nov 1983.

[16] B. Abeles, "Amorphous semiconductor superlattices," *Superlattices and Microstructures*, vol. 5, pp. 473–480, Jul 1989.

[17] I. Saito, W. Miyazaki, M. Onishi, Y. Kudo, T. Masuzawa, T. Yamada, A. Koh, D. Chua, K. Soga, M. Overend, M. Aono, G. A. J. Amaratunga, and K. Okano, "A transparent ultraviolet triggered amorphous selenium p-n junction," *Applied Physics Letters*, vol. 98, p. 152102, Apr 2011.

[18] J. D. John, S. Okano, A. Sharma, O. Selyshchev, M. Rahaman, N. Miyachi, K. Enomoto, J. Ochiai, I. Saito, T. Masuzawa, T. Yamada, D. H. C. Chua, D. R. T. Zahn, and K. Okano, "Transport properties of Se/As_2Se_3 nanolayer superlattice fabricated using rotational evaporation," *Advanced Functional Materials*, vol. 29, no. 40, p. 1904758, 2019.

[19] R. L. Anderson, "Experiments on Ge-GaAs heterojunctions," *Solid-State Electronics*, vol. 5, pp. 341–351, 1962.

[20] E. A. Davis, "Optical absorption, transport and photoconductivity in amorphous selenium," *Journal of Non-Crystalline Solids*, vol. 4, pp. 107–116, 1970.

[21] G. S. Belev, *Electrical properties of amorphous selenium based photoconductive devices for application in X-ray image detectors*. PhD thesis, Department of Electrical and Computer Engineering, University of Saskatchewan, Saskatoon, SK, Canada, Jan 2007.

[22] A. Zakery and S. R. Elliot, *Optical Nonlinearities in Chalcogenide Glasses and their Applications*. Springer, Berlin Heidelberg, 2007.

[23] M. Abkowitz, "Density of states in a-Se from combined analysis of xerographic potentials and transient transport data," *Philosophical Magazine Letters*, vol. 58, no. 1, pp. 53–57, 1988.

[24] G. Pfister and M. Morgan, "Defects in chalcogenide glasses I. The influence of thermally induced defects on transport in a-As_2Se_3," *Philosophical Maganize Part B*, vol. 41, pp. 191–202, Jul 1980.

[25] N. F. Mott, "Electrons in non-crystalline materials: The last twenty five years," *Contemporary Physics*, vol. 26, pp. 203–215, Mar 1985.

[26] G. Belev and S. Kasap, "Amorphous selenium as an X-ray photoconductor," *Journal of Non-Crystalline Solids*, vol. 345-346, pp. 484–488, 2004. Physics of Non-Crystalline Solids 10.

[27] I. Saito, *Amorphous Selenium Photoelectric Devices*. PhD thesis, Wolfson College, Department of Engineering, University of Cambridge, Cambridge, United Kingdom, Jan 2011.

[28] M. Okuyama, H. Takakura, and Y. Hamakawa, "Fourier transformation analysis of deep level transient signals in semiconductors," *Solid-State Electronics*, vol. 26, pp. 689–694, Aug 1983.

[29] S. Weiss and R. Kassing, "Deep Level Transient Fourier Spectroscopy (DLTFS) - A technque for the analysis of deep level properties," *Solid-State Electronics*, vol. 31, pp. 1733–1742, Jun 1988.

[30] G. Pfister and M. Morgan, "Defects in chalcogenide glasses II. The effect of metallic impurities on the transport properties of a-As_2Se_3," *Philosophical Maganize Part B*, vol. 41, pp. 209–234, Jul 1980.

[31] S. Kasap, C. Koughia, J. Berashevich, R. Johanson, and A. Reznik, "Charge transport in pure and stabilized amorphous selenium: re-examination of the density of states distribution in the mobility gap and the role of defects," *Journal of Material Science: Materials in Electronics*, vol. 26, pp. 4464–4658, May 2015.

[32] F. Sedouk and M. L. Benkhedir, "Density of states in pure and As doped amorphous selenium determined from transient photoconductivity using Laplace-transform method," *Physica B*, vol. 459, pp. 122–128, Aug 2015.

[33] N. F. Mott, "Electrons in Glass," *Revue de Physique Appliquee*, vol. 12, pp. 619–629, May 1977.

[34] H. Fritzsche, "The Nature of Localized States and the Effect of Doping in Amorphous Semiconductors," *Chinese Journal of Physics*, vol. 15, pp. 73–89, Mar 1977.

[35] V. V. Mitin, V. A. Kochelap, and M. A. Stroscio, *Quantum heterostructures : microelectronics and optoelectronics*. Cambridge University Press, Cambridge, 1999.

Chapter 4

Optical properties of Se, As_2Se_3 and superlattice amorphous Se *

*This chapter is based on the following publication:
John, J. D., et al., "Spectroscopic Ellipsometry of amorphous Se superlattices. **Journal of Physics D**, 2021 (Accepted manuscript) https://doi.org/10.1088/1361-6463/abf228

4.1 Introduction

Superlattice structures, made from a periodic arrangement of nano-layers of different materials, have unusual optical and electrical properties like negative dynamic resistance and effective mass filtering [1, 2]. These properties are highly desired for optoelectronic devices like quantum cascade lasers and ultrasensitive photo-detectors. However, these properties and devices are not widely available since superlattice structures require high-tech fabrication methods, like Molecular Beam Epitaxy (MBE) or Atomic Layer Deposition (ALD). Superlattice structures fabricated using amorphous silicon and amorphous silicon carbide were investigated, with the results showing a stretching of the distribution of localized states [3, 4]. Amorphous Selenium (Se) and Arsenic Selenide (As_2Se_3) have a long history of application in optoelectronic devices. A combination of the two materials was shown to exhibit even better photo-detection performance with high quantum efficiencies [5, 6]. This material combination is also a promising candidate for ultrasensitive flat-panel X-ray imagers [7, 8]. Recent work revealed that multi-layer films of Se and As_2Se_3 fabricated using rotational evaporation exhibit electrical properties associated with superlattice structures, altering the band structures of the base materials and resulting in sequential tunneling based transport phenomena observed as oscillations in the current-voltage (I-V)characteristics [9, 10]. It is therefore expected that an optical study should also reveal characteristics emanating from the superlattice structure. Two-dimensional superlattice structures are known to have a density of states that follows a series of constant energy levels due to quantum confinement in one-dimension [11]. The optical absorption coefficient is proportional to the joint density of states. Thus by measuring the optical properties, the nature of the joint density of states can be determined, possibly confirming the superlattice structure of rotationally evaporated Se and As_2Se_3 superlattices. Spectroscopic ellipsometry provides an accurate, non-destructive method for evaluating the optical properties of layered semiconductor structures [12]. A basic review of spectroscopic ellipsometry is presented in Appendix C. The method has been successfully applied to superlat-

tice structures, showing excitonic peaks associated with sub-band transitions, and also reliably evaluating the quality of superlattice structures from different deposition conditions [13, 14]. Compared to destructive depth profiling methods such as Secondary Ion Mass Spectroscopy (SIM), spectroscopic ellipsometry is non-destructive and provides access to depth profiles and optical properties simultaneously. This is highly desirable in evaluating superlattice structures integrated in active devices such as quantum cascade lasers and Modulation Doped Field Effect Transistors (MODFET) [14]. Another interesting application is evaluating nanostructures of phase-changeable materials such as Phase Changeable Memories (PCM) [15, 16]. We were interested in determining the quality of superlattices fabricated from amorphous materials deposited using the technologically simple method of rotational evaporation, and the optical properties of the resulting superlattices. We therefore fabricated samples of amorphous Se, As_2Se_3, and a multinanolayer structure of the two materials, using rotational evaporation, and studied the resulting films using spectroscopic ellipsometry.

4.2 Results and Discussion

The three types of samples were then studied using spectroscopic ellipsometry. The Variable Angle Spectroscopic Ellipsometry (VASE) measurements were performed on a M2000 ellipsometer (J. Woolam) running the CompleteEase 5.15 software for analysis and modeling [17]. The light spot size had a diameter of 3 mm, and the spectral energy range was from 0.75 eV to 5.2 eV. The angle of incidence was varied from 45° to 75° in steps of 5°. The schematic of the system is shown in Fig. 4.1.

All samples were measured under room temperature and ambient conditions. The system measured the amplitude, Ψ, and phase shift, Δ, of the light's electric field after interacting with the sample. The amplitude and phase shifts (Ψ and Δ) from the spectroscopic ellipsometry for each type of sample are shown in Fig. 4.2.

The results for each type of sample were modeled with a B-Spline fit with resolution 0.025 eV to give the refractive index, n, and extinction coefficient, k. The B-Spline

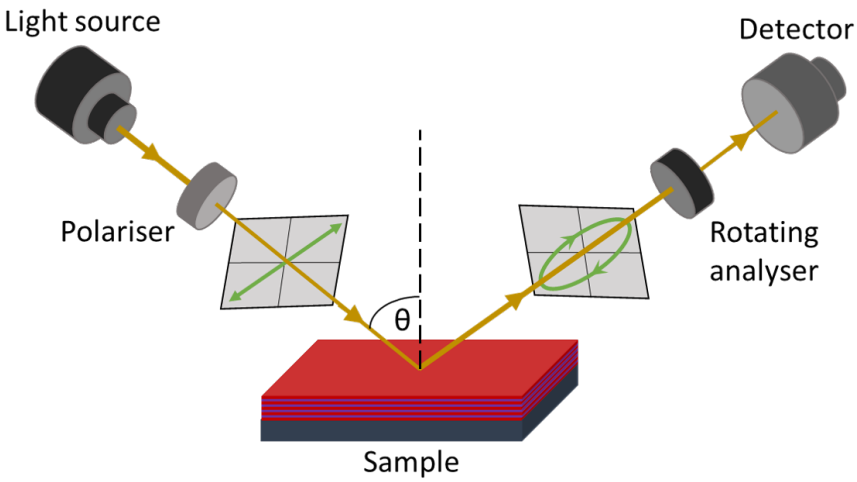

Figure 4.1: Sample measurement using spectroscopic ellipsometry. The angle of incidence θ was varied from 45° to 75° in steps of 5°, with the sample measured at each angle using light in the range from 0.75 eV to 5.2 eV.

model can be used to model the dielectric function as

$$\epsilon_2(\omega) = \sum_{i=1}^{N} c_i B_i^k(\omega) \tag{4.1}$$

where the basis splines B_i^k are [18, 19]

$$B_i^0(x) = \begin{cases} 1 & t_i \leq x < t_{i+1} \\ 0 & \text{otherwise} \end{cases} \tag{4.2}$$

$$B_i^k(x) = \left(\frac{x - t_i}{t_{i+k} - t_i}\right) B_i^{k-1}(x) + \left(\frac{t_{i+k+1} - x}{t_{i+k+1} - t_{i+1}}\right) B_{i+1}^{k-1}(x) \tag{4.3}$$

where k is the degree of the B-Spline, t_i is the ith knot location on the x-axis. Knots also known as nodes are locations on the x-axis where the polynomial segments connect. The real part of the dielectric function can then be obtained using Kramers-Kronig causality relations [18, 20].

The parameters of the fitted model are shown in Table 4.1. The graphs of the resulting n and k from the B-Spline fitting are shown in Fig. 4.3.

These n and k were then parametrized using Cody-Lorentz oscillators. The Cody-

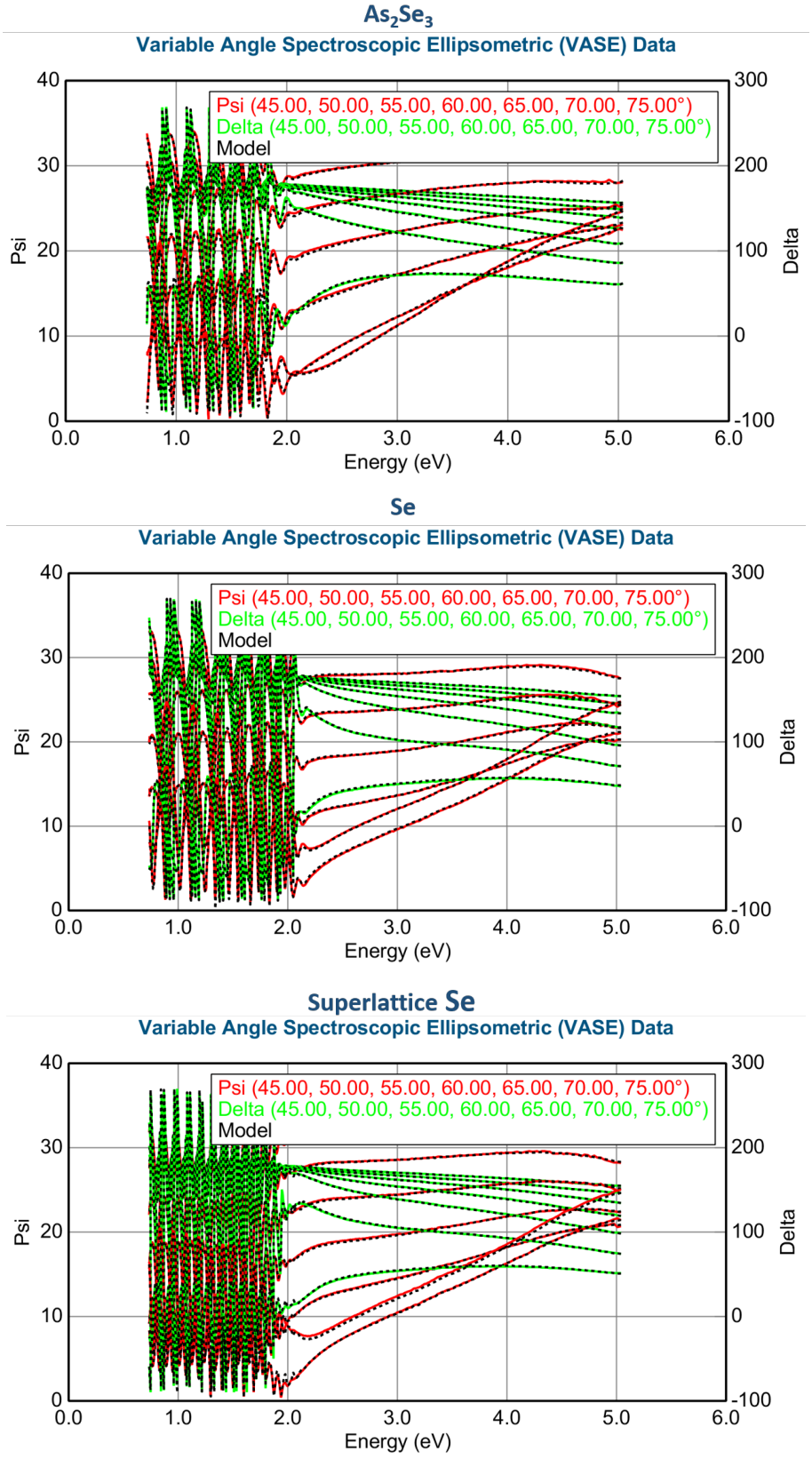

Figure 4.2: The amplitude Ψ and phase shift Δ data for Se, As_2Se_3 and superlattice Se measured at angles from 45° to 75° in steps of 5°.

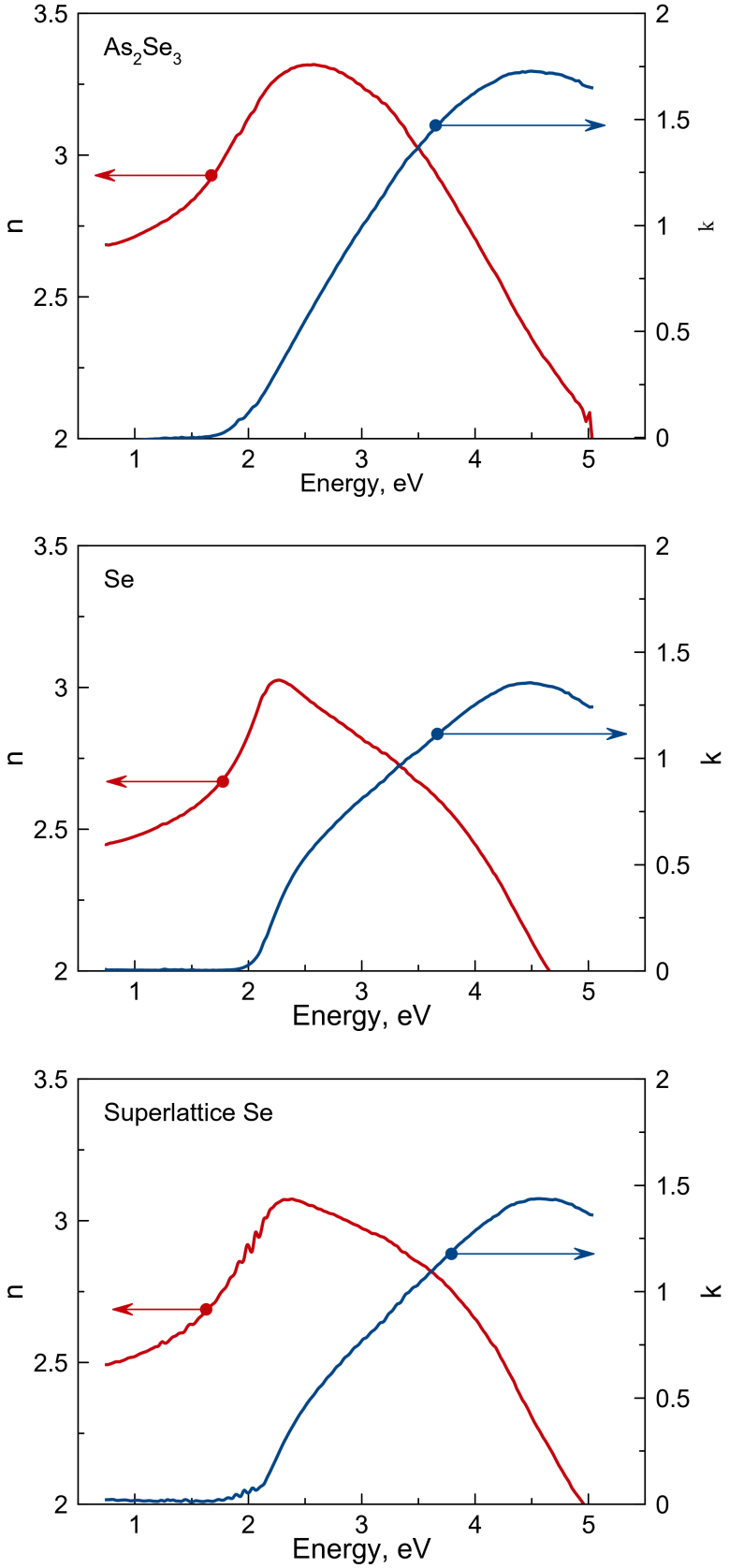

Figure 4.3: Resulting refractive index, n, and extinction coefficient, k, for Se, As_2Se_3 and superlattice Se after fitting Ψ and Δ data using a B-Spline with resolution 0.025 eV.

Table 4.1: Parameters used to fit the B-Spline model for Se, As_2Se_3 and superlattice Se. The film thicknesses agree reasonably with values measured during deposition using a crystal oscillator.

Parameter	Se	As_2Se_3	Superlattice Se
MSE	7.828	10.649	8.314
Thickness [nm]	1070.20±0.16	1010.76±0.13	2090.24±0.42
n of B-Spline at 1.96 eV	2.79673	3.10087	2.86156
k of B-Spline at 1.96 eV	0.01691	0.090007	0.06391

Lorentz oscillator, in addition to absorption at energies above the optical band gap, takes into account the Urbach absorption below the band gap, which is expected for amorphous materials [12, 17]. In the Cody-Lorentz oscillator, the imaginary part of the dielectric function $\epsilon_2(E)$ has the form [21]

$$\epsilon_2(E) = \begin{cases} \frac{E_l}{E} \exp\left[\frac{(E - E_{gn} + E_{tn})}{E_{un}}\right] & : 0 < E \leq (E_{gn} + E_{tn}) \\ \\ \frac{(E - E_{gn})^2}{(E - E_{gn})^2 + E_{pn}^2} \cdot \frac{A_n E_{0n} \Gamma_n E}{(E^2 - E_{0n}^2) + \Gamma_n^2 E^2} & : E > (E_{gn} + E_{tn}) \end{cases}$$

where, for the nth oscillator,

- A_n is the amplitude of the Lorentzian peak,
- Γ_n is the Full Width at Half Maximum (FMHW) of the Lorentzian peak,
- E_{0n} is the energy at the peak position ,
- E_{pn} is the transition from Lorentzian absorption to Cody absorption,
- E_l is the demarcation energy between band to band and Urbach tail transitions,
- E_{tn} is the transition from Cody absorption to Urbach absorption, and
- E_{un} is the exponential rate of the transition E_t.

The superlattice material has unique optical properties, different from the individual materials Se and As_2Se_3. As such, the superlattice material was modeled as a single

layer with unknown thickness. The parameters of the oscillators for Se, As_2Se_3 and superlattice Se are shown in Table 4.2 a) and the additional Lorentz oscillators for superlattice Se are shown in Table 4.2 b). The thicknesses from the ellipsometric model

Table 4.2: a) Parameters used to fit the Cody-Lorentz model for Se, As_2Se_3, and superlattice Se, and b) additional parameters for Lorentz oscillators modeling the "steps" observed near $E_{G,Opt}$ of the superlattice.

(a) Parameters used to fit the Cody-Lorentz model for Se, As_2Se_3 and superlattice Se.

Parameter	Se	As_2Se_3	Superlattice Se
MSE	15.743	15.112	37.71
Thickness [nm]	1060.62±0.12	1018.19±0.21	1989.62±1.63
$E_{g,opt}$ [eV]	1.968±0.0055	1.689±0.0009	1.691±0.002
A	46.394	62.475	51.631
Γ	8.374	6.408	7.807
E_0	5.921	4.536	5.282
E_p	0.351	1.088	0.786
E_t	0.141	0.222	0.443
E_u	0.076	0.104	0.127

(b) Parameters used to fit Lorentz oscillators for the "steps" observed near $E_{G,Opt}$ of the superlattice

n	E_n [eV]	Amp	Br
1	1.724±0.0024	0.057	0.050
2	1.817±0.0663	0.700	0.041
3	1.891±0.0103	0.103	0.0341
4	1.965±0.0081	0.157	0.0356
5	2.036±0.0114	0.107	0.0398

agreed reasonably well with the target thicknesses measured by the crystal oscillator. The modeled optical parameters are shown in Fig. 4.4.

The extinction coefficient, k, can be used to obtain the absorption coefficient α [20],

$$\alpha = \frac{4\pi k}{\lambda} \tag{4.4}$$

where λ is the photon wavelength. The absorption coefficient is proportional to the joint density of states [11]. The absorption coefficient plot for superlattice Se is shown in Fig. 4.5.

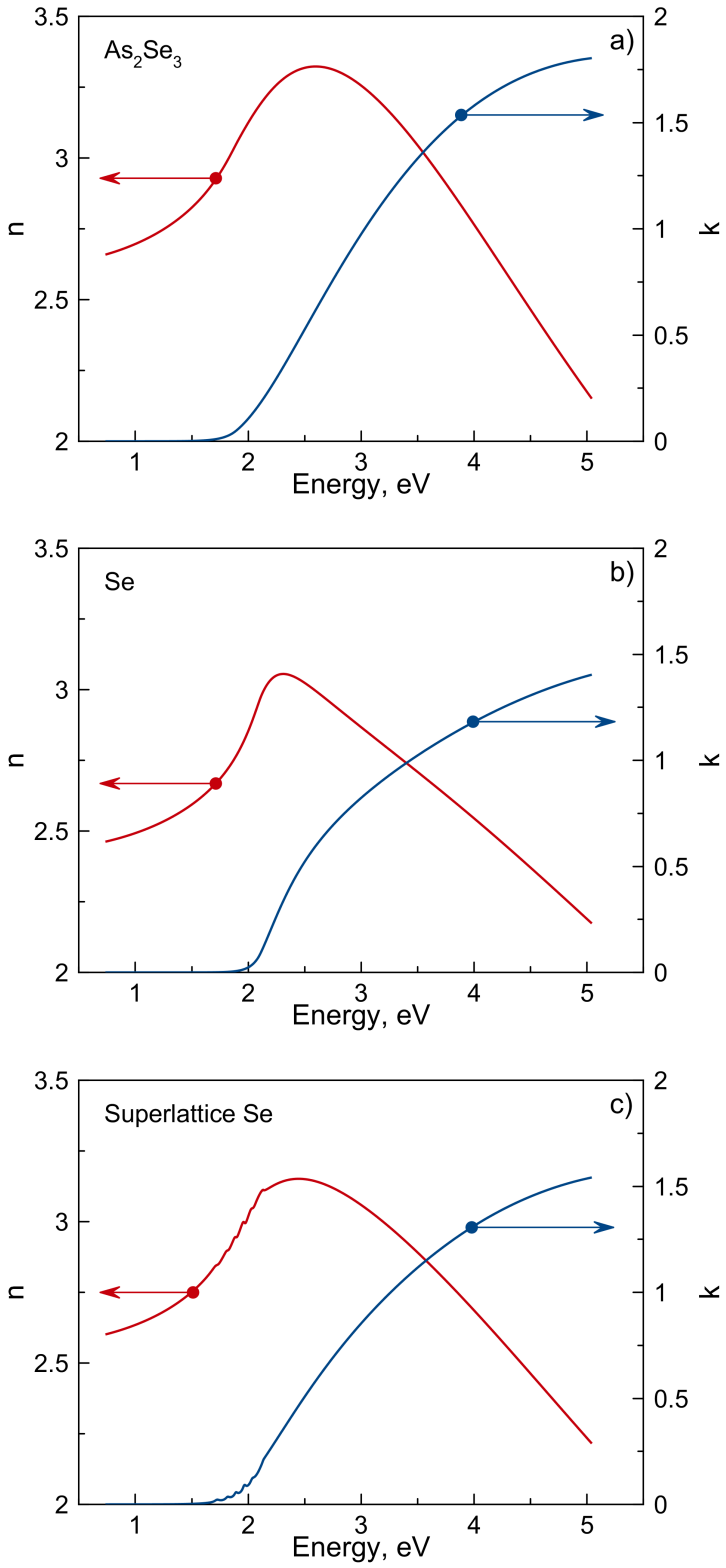

Figure 4.4: The refractive index, n, and extinction coefficient, k, of a) As_2Se_3, b) Se, and c) superlattice Se. These optical constants were obtained after modeling with Cody-Lorentz oscillators.

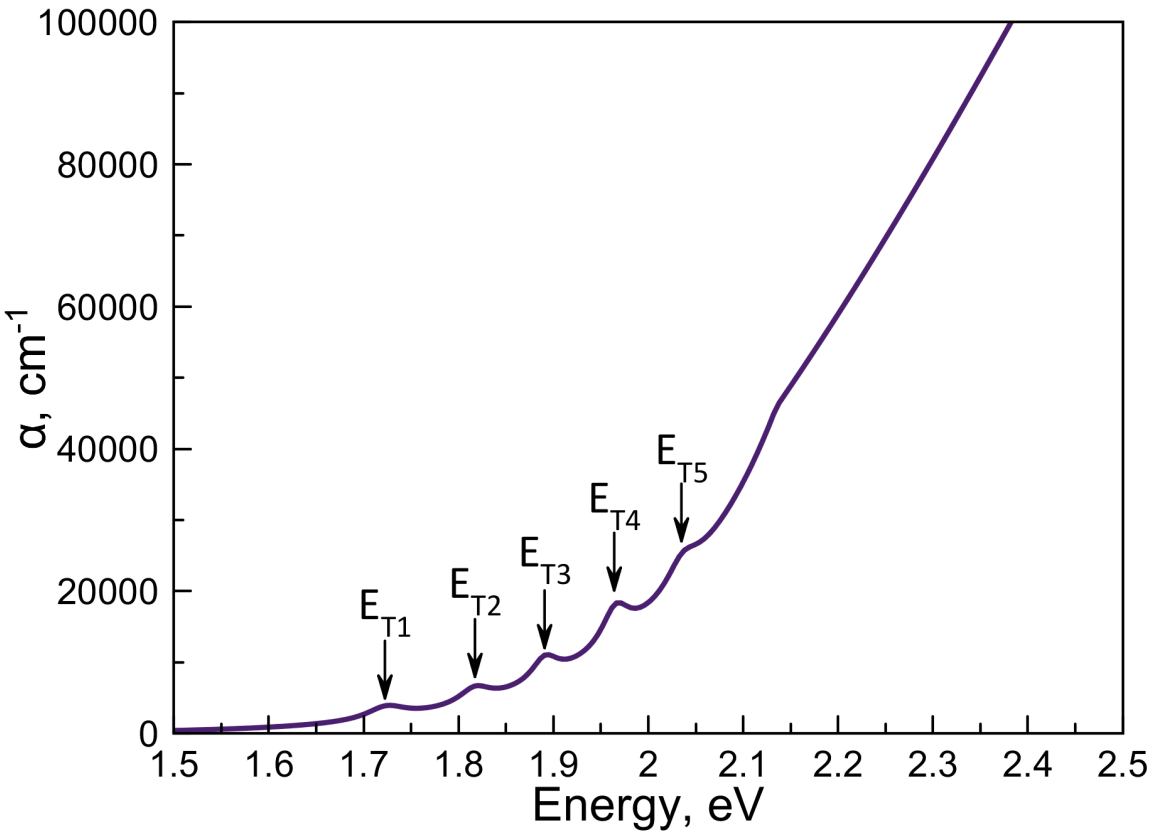

Figure 4.5: The absorption coefficient, α, of the superlattice Se, showing a series of five "staircase steps" in energy. These steps stem from transitions between energy levels in quantum wells of the superlattice structure. The inset shows the band structure (not to scale) used to calculate the energy levels in the quantum wells following the Kronig-Penney model [22, 23].

The absorption coefficient shows a series of "staircase steps" as expected of a superlattice where carriers are confined in one dimension. The peaks of the steps are associated with transitions from energy levels in the quantum wells of the superlattice structure. The transitions are governed by selection rules, specifically that the transition can only occur from energy levels with the same quantum number *i.e.* $\Delta n = 0$ [11]. As such the absorption steps, E_{Tn}, will be given by

$$E_{Tn} = E_{G,Opt} + E_{en} + E_{hn} \tag{4.5}$$

where $E_{G,Opt}$ is the optical band gap of the quantum well material, E_{en} is the nth energy state for electrons in the quantum wells, and E_{hn} is the nth energy state for holes in the quantum wells.

The energy levels in the superlattice quantum wells were calculated following the Kronig-Penney model [22, 23]. The derivation of the equation for energy levels and wave-functions is discussed in Appendix A. The optical band gaps obtained from the Cody-Lorentz models shown in Fig. 4.4, for Se and As_2Se_3 were 1.97 eV and 1.69 eV respectively, with the Fermi level set to be at $E_V + 0.8$ eV for Se and at the mid gap for As_2Se_3 [9]. Effective masses in the quantum well material As_2Se_3 were set as 0.27 and 0.28 for electrons and holes respectively [24]. The quantum well width used was 8 nm. A sketch of the resulting band structure is shown in Fig. 4.6. The results of the calculations were then compared to the transitions measured using ellipsometry, as shown in Table 4.3. In this way the observed transitions can be explained as stemming

Table 4.3: Transitions measured from ellipsometry compared to those obtained from the calculation based on the Kronig-Penney model. The optical band gap, $E_{G,Opt}$, of the quantum well material As_2Se_3 was 1.69 eV.

n	E_n [eV]	E_{en} [eV]	E_{hn} [eV]	E_{Tn} [eV]	Discussion
1	1.724	0.019	0.011	1.720	Transition between lowest quantum well levels for holes and electrons.
2	1.817	0.074	0.044	1.808	Transition between the second quantum well levels for holes and electrons.
3	1.891	0.163	-	1.853	Transitions from $E_{V,As2Se3}$ to the third quantum well level for electrons.
4	1.965	0.277	-	1.967	Transitions from $E_{V,As2Se3}$ to the fourth quantum well level for electrons.
5	2.036	-	-	2.015	Transitions from $E_{V,As2Se3}$ to $E_{C,Se}$

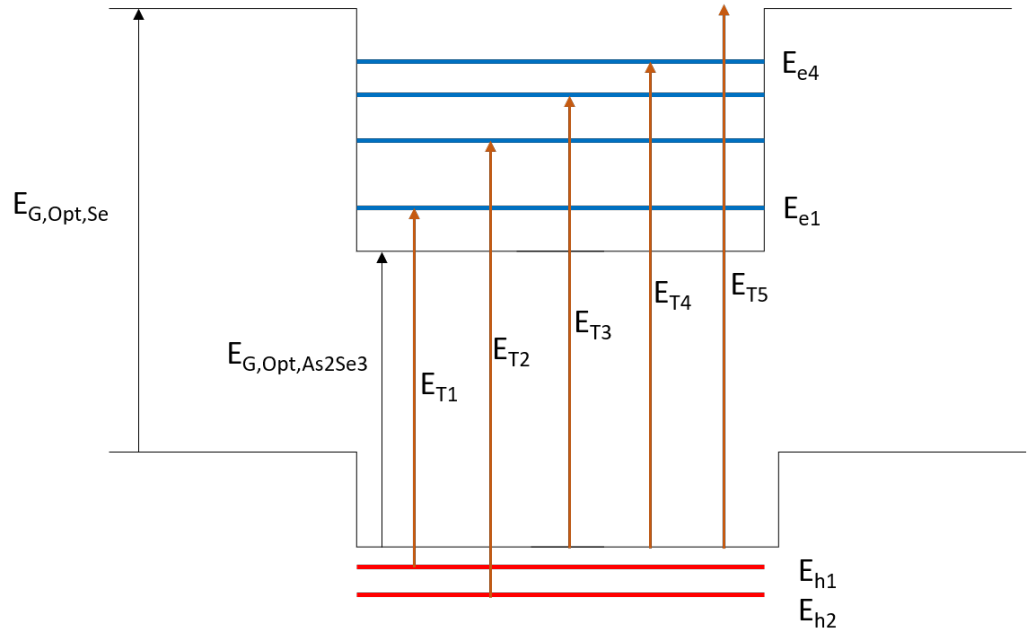

Figure 4.6: The band structure (not to scale) used to calculate the energy levels in the quantum wells following the Kronig-Penney model [22, 23], along with the transitions from the energy levels, following the $\Delta n = 0$ selection rule. These calculated transitions are compared to measured results in Table 4.3.

from quantum confined levels of the superlattice structure. The first two transitions are from the first and second energy levels, respectively, of the quantum wells for holes and electrons. The third and fourth transitions are from the valence band of As_2Se_3 to the third and fourth energy levels, respectively, of the quantum well for electrons. The fifth transition occurs from the valence band of As_2Se_3 to the conduction band of Se. The observation of transitions due to confined levels shows that it was possible to fabricate a well defined superlattice structure using rotational evaporation of Se and valence band of As_2Se_3.

4.3 Optical and electrical band gap

There is a difference between the electrical and optical band gaps when results form electrical and optical characterizations are compared. The electrical band gaps used were 2.1 eV for Se determined from xerographic measurements [25], and 1.1 eV for As_2Se_3 determined from Seeback measurements [26]. From ellipsometry measurements,

the optical band gap of Se (1.97 eV) is smaller than the electrical band gap, while for As_2Se_3 the electrical band gap is smaller compared to the optical band gap (1.69 eV). The difference in optical and electrical band gap was treated in literature [27]. The discussion therein showed that the optical band gap is insensitive to potential fluctuations compared to the electrical band gap. Short wavelength potential fluctuations are the origin of localized states and thus affect the electrical properties significantly. However, these localized states seem to have a much lower density compared to extended states, and as such optical transitions between these localized states and extended states are not observed. Thus the optical band gap is related to transitions only between extended states whereas the electrical band gap includes localized states.

The difference in electrical and optical band gaps has a significant impact on the superlattice structure of Se and As_2Se_3. The electronic energy structure of the superlattice was evaluated using Deep Level Transient Spectroscopy (DLTS) on a HERA DLTS system [10]. The samples were measured in the temperature range from 140 K to 300 K, with a filling voltage pulse of 5 V and a time window of 20.48 ms. The resulting capacitance transient was Fourier transformed and the time constants obtained from the resulting Fourier coefficients [28]. The time constants were then used to plot Arrhenius plots which provide the energy levels. The results revealed two energy levels at 0.533 eV from the conduction band of Se and 0.267 eV from the valence band of Se. These energy levels were explained as defect level modulation and miniband formation due to the superlattice periodic potential, and sequential tunneling transport from the miniband level [9, 10]. Optical measurements using spectroscopic ellipsometry reported herein showed transitions from quantized energy levels in the extended states of the superlattice materials. A band structure can be visualized for the difference between the optical and electrical gaps. If the band structure is referenced to a common Fermi level, the electrical superlattice structure is different from the optical. Such a band structure is shown in Fig. 4.7.

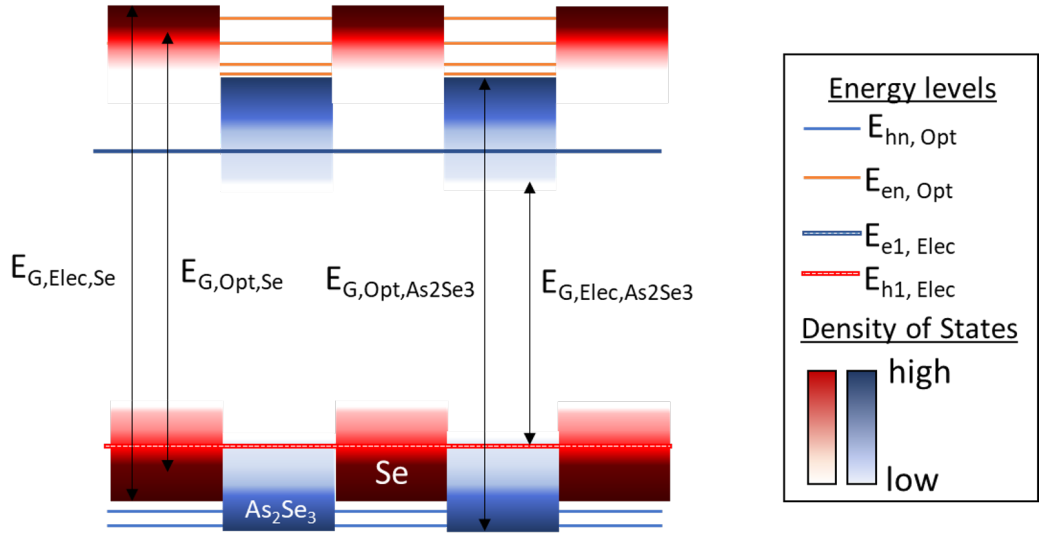

Figure 4.7: A band diagram showing the superlattice structure of amorphous Se and As_2Se_3. The band edges are shown using gradient shading to indicate the tailing of states. The superlattice periodic potential results in quantized energy levels ($E_{en,Opt}$ and $E_{hn,Opt}$) in the extended states and miniband formation in the localized states ($E_{e1,Elec}$ and $E_{h1,Elec}$),

Optical measurements only showed transitions from quantized energy levels ($E_{en,Opt}$ and $E_{hn,Opt}$ shown in Fig. 4.7) in the extended states of the superlattice materials, with the transition from the miniband levels ($E_{e1,Elec}$ and $E_{h1,Elec}$ shown in Fig. 4.7) not appearing. These results therefore suggest that the superlattice periodic potential causes quantization in the extended states, and miniband formation with defect level modulation in the localized states. As an ongoing investigation, the quantum well width and superlattice period can be used as a caliper to change the quantization and observe the impact on localized and extended states using a zoo of optical and electrical measurements.

4.4 Conclusion

We studied the optical properties of amorphous Se superlattices using spectroscopic ellipsometry. The amorphous nature of the deposited samples was confirmed using Raman spectroscopy, and each type of sample, amorphous As_2Se_3, amorphous Se, and su-

perlattice Se exhibited broad peaks as expected for amorphous materials. The samples were then studied using spectroscopic ellipsometry to obtain their optical parameters. These optical parameters were modeled using Cody-Lorentz oscillators. As_2Se_3 samples exhibited an optical band gap of 1.69 eV. Se samples showed an optical bandgap of 1.97 eV. Superlattice Se samples showed a series of five steps of energy at 1.72 eV, 1.82 eV, 1.89 eV, 1.97 eV and 2.04 eV. The energy steps are due to the two-dimensional density of states from the quantized energy levels in the superlattice structure. The results of the spectroscopic ellipsometry study of the superlattice Se confirmed that a well defined superlattice structure could be fabricated using amorphous materials and simple fabrication methods of rotational evaporation. These results open a way to simpler fabrication of novel nanostructures using amorphous, crystalline-amorphous mixed-phase, and phase-changeable materials, along with characterization using advanced non-destructive methods like spectroscopic ellipsometry.

References

[1] L. Esaki, "Advances in semiconductor superlattices, quantum wells and heterostructures," *Journal de Physique Colloques*, vol. 45, pp. C5–3–C5–21, Apr 1984.

[2] F. Capasso, "Band-gap engineering: From physics and materials to new semiconductor devices," *Science*, vol. 235, no. 4785, pp. 172–176, 1987.

[3] B. Abeles and T. Tiedje, "Amorphous semiconductor superlattices," *Physical Review Letters*, vol. 51, pp. 2003–2006, Nov 1983.

[4] S. Miyazaki, "Amorphous semiconductor superlattices (in Japanese)," *New Glass*, vol. 5, no. 1, pp. 45–56, 1990.

[5] K. Tanioka, "Ultra-high-sensitivity new Super-HARP pickup tube," in *Proc. 2001 IEEE Workshop CCD and Advanced Image Sensors*, pp. 216–219, IEEE, 2001.

[6] T. Masuzawa, S. Kuniyoshi, M. Onishi, R. Kato, I. Saito, T. Yamada, A. T. Koh, D. H. C. Chua, T. Shimosawa, and K. Okano, "Conditions for a carrier multiplication in amorphous-selenium based photodetector," *Applied Physics Letters*, vol. 102, no. 073506, pp. 1–4, 2013.

[7] M. J. Yaffe and J. A. Rowlands, "X-ray detectors for digital radiography," *Physics in Medicine and Biology*, vol. 42, pp. 1–39, Aug 1997.

[8] S. Kasap and M. Zangahir Kabir, "Photoconductors for X-ray Image Detectors," in *Handbook of Electronic and Photonic Materials*, pp. 1125–1147, Springer US, 2017.

[9] J. D. John, S. Okano, A. Sharma, O. Selyshchev, M. Rahaman, N. Miyachi, K. Enomoto, J. Ochiai, I. Saito, T. Masuzawa, T. Yamada, D. H. C. Chua, D. R. T. Zahn, and K. Okano, "Transport properties of Se/As_2Se_3 nanolayer superlattice fabricated using rotational evaporation," *Advanced Functional Materials*, vol. 29, no. 40, p. 1904758, 2019.

[10] J. D. John, S. Okano, A. Sharma, O. Selyshchev, M. Rahaman, N. Miyachi, K. Enomoto, J. Ochiai, G. Saito, Ichitaro Salvan, T. Masuzawa, T. Yamada, D. H. C. Chua, D. R. T. Zahn, and K. Okano, "Observation of two-level defect system in amorphous Se superlattices," *Applied Physics Letters*, vol. 116, p. 192104, 2020.

[11] P. Blood, *Optical transitions in quantum wells*. Oxford: Oxford University Press, 2015.

[12] H. Fujiwara, *Spectroscopic Ellipsometry: Principles and Applications*. John Wiley and Sons, 2007.

[13] J. A. Woolam, P. G. Snyder, K. G. Merkel, and S. A. Alterovitz, "Ellipsometric characterization of multilayer transistor structures," *Materials Science and Engineering*, vol. B5, pp. 291–294, 1990.

[14] P. G. Snyder, B. N. De, K. G. Merkel, and J. A. Woolam, "Measurement of superlattice optical properties by variable angle spectrocopic ellipsometry," *Superlattices and Microstructures*, vol. 4, no. 1, pp. 97–99, 1987.

[15] T. C. Chong, L. P. Shi, X. Q. Wei, R. Zhao, H. K. Lee, P. Yang, and A. Y. Du, "Crystalline amorphous semiconductor superlattice," *Phys. Rev. Lett.*, vol. 100, p. 136101, Mar 2008.

[16] M. L. Gallo and A. Sebastian, "An overview of phase-change memory device physics," *Journal of Physics D: Applied Physics*, vol. 53, p. 213002, mar 2020.

[17] J. A. Woolam, *CompleteEASE Software Manual*. J. A. Woolam Co., Lincoln, USA, 2014.

[18] B. Johs and J. S. Hale, "Dielectric function representation by B-splines," *physica status solidi (a)*, vol. 205, no. 4, pp. 715–719, 2008.

[19] J. Weber, T. Hansen, V. de Sanden, and R. R. Engeln, "B-spline parametrization of the dielectric function applied to spectroscopic ellipsometry on amorphous carbon," *Journal of Applied Physics*, vol. 106, p. 123503, 2009.

[20] J. I. Pankove, *Optical Processes in Semiconductors*. Dover Publications, 1975.

[21] A. S. Ferlauto, G. M. Ferreira, J. M. Pearce, C. R. Wronski, R. W. Collins, X. Deng, and G. Ganguly, "Analytical model for the optical functions of amorphous semiconductors from the near-infrared to ultraviolet: Applications in thin film photovoltaics," *Journal of Applied Physics*, vol. 92, no. 5, pp. 2424–2436, 2002.

[22] d. L. R. Kronig and W. G. Penney, "Quantum mechanics of electrons in crystal lattices," *Proceedings of the Royal Society London A*, vol. 130, pp. 499–513, 1931.

[23] L. Esaki and L. L. Chang, "New transport phenomenon in a semiconductor "superlattice"," *Physical Review Letters*, vol. 33, pp. 496–498, Aug 1974.

[24] E. Antonelli, A. Tarnow and J. D. Joannopoulos, "New insight into the electronic structure of As_2Se_3," *Physical Review B*, vol. 33, pp. 2968–2971, Feb 1986.

[25] E. A. Davis, "Optical absorption, transport and photoconductivity in amorphous selenium," *Journal of Non-Crystalline Solids*, vol. 4, pp. 107–116, 1970.

[26] C. H. Seager and R. K. Quinn, "Dc electronic transport in binary arsenic chalcogenide glasses," *Physical Review B*, vol. 17, pp. 386–400, 1975.

[27] H. Fritzsche, "Optical and electrical energy gaps in amorphous semiconductors," *Journal of Non-crystalline Solids*, vol. 6, pp. 49–71, 1971.

[28] S. Weiss and R. Kassing, "Deep Level Transient Fourier Spectroscopy (DLTFS) - A technque for the analysis of deep level properties," *Solid-State Electronics*, vol. 31, pp. 1733–1742, Jun 1988.

Chapter 5

Transport properties of superlattice amorphous Se *

*This chapter is based on the following publication:
John, J. D., et al., "Transport Properties of Se/As_2Se_3 Nanolayer Superlattice Fabricated Using Rotational Evaporation." **Advanced Functional Materials**, 2019, 29, 1904758. https://doi.org/10.1002/adfm.201904758)

5.1 Introduction

Multi-material multi-layer amorphous Se based structures have already been successfully applied in a High-gain Avalanche Rushing Photoconductor (HARP) camera [1]. Recently, attempts have been made to utilize amorphous Se HARP features for ultra-sensitive X-ray detection, which is essential for low-dose imaging [2, 3]. Features of the HARP, such as the high detectivity for low intensity light and avalanche multiplication, key to the success of the device, have been the subject of models like the Lucky Drift, Polaronic-Supersonic Transformation and Cascade Multiplication [1, 4, 5, 6]. With the exception of Cascade Multiplication, most models treat the amorphous Se as a bulk material in which As_2Se_3 is only incorporated to stabilize the material against thermal degradation. A bulk material of the same stoichiometry as the Se and As_2Se_3 layered structure does not exhibit photomultiplication [7]. However, Cascade Multiplication hints that the layered structure creates separate regions for acceleration and for collision. So far, no physical interpretation with scientific evidence has been presented. Herein, we investigate the device from the perspective that its layered structure, fabricated by rotational evaporation, qualifies it as a form of superlattice and/or heterostructure and as such has to be analyzed using corresponding physics. Such an understanding broadens the possible applications of these low-tech fabricated superlattices. For example, while conventional approaches are to use amorphous Se HARP as the direct conversion absorber of X-rays, we see the superlattice Se as having more effect as a blocking/selective transport layer and amplifier, easily attached to X-ray absorbing materials such as perovskites, CdTe, Ge or Si, which have challenges with dark/leakage currents and signal to noise ratio (SNR) [8, 9]. Herein we discuss the transport characteristics, measured using variations of current with applied voltage (I-V) of superlattice Se deposited on n-type Si.

5.2 Materials and Methods

Samples were fabricated on n-type Si substrates using a rotational evaporation system, and characterized using TOF-SIMS and Raman spectroscopy as discussed in Chapter 2.

The samples were then characterized using Deep Level Transient Spectroscopy (DLTS) to measure the energy level structure. A top contact of solidified Ag paste was placed on the superlattice Se surface, with Al foil contact attached to n-type Si side also using Ag paste. This sample structure was then connected as the device under test on a FT1030 HERA DLTS system. The sample structure and measurement schematic are shown in Fig. 5.1.

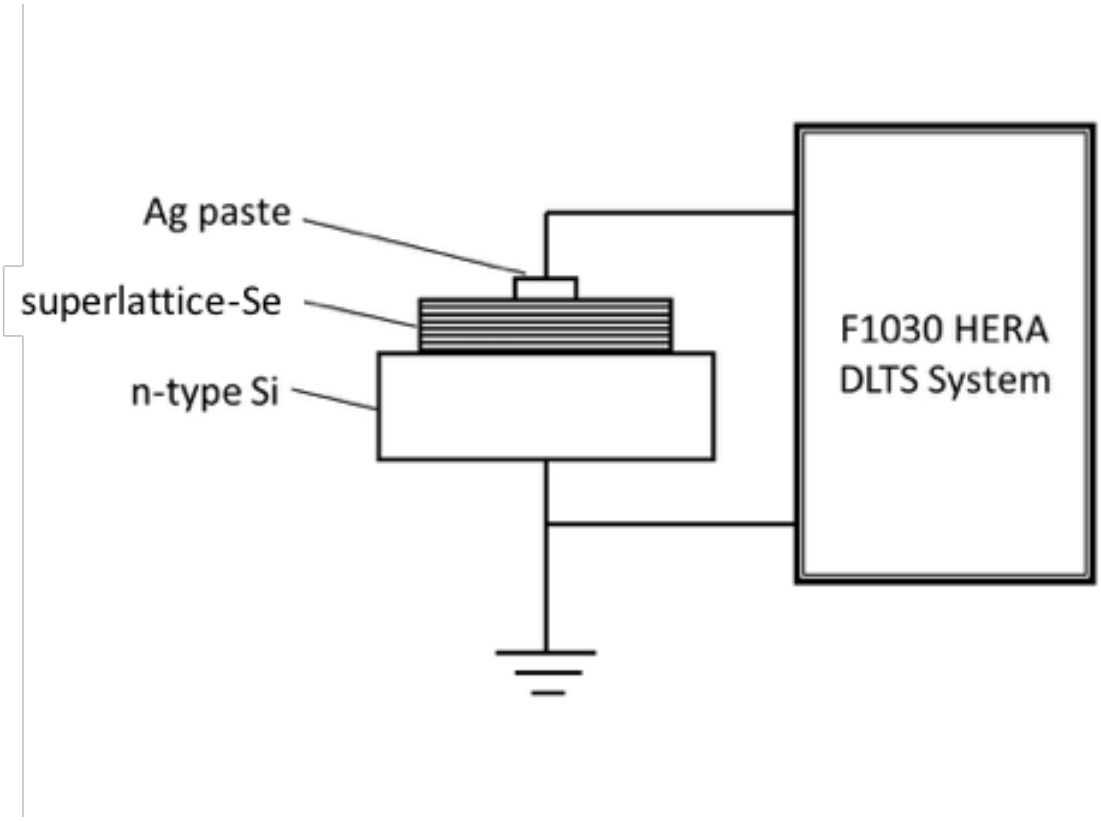

Figure 5.1: The samples structure and connection to the FT1030 HERA DLTS system.

The measurement was performed under dark conditions with a temperature scan from 130 K to 300 K with the upper temperature limit chosen to stay below the glass transition temperature of amorphous of about 318 K [10]. An initial capacitance-

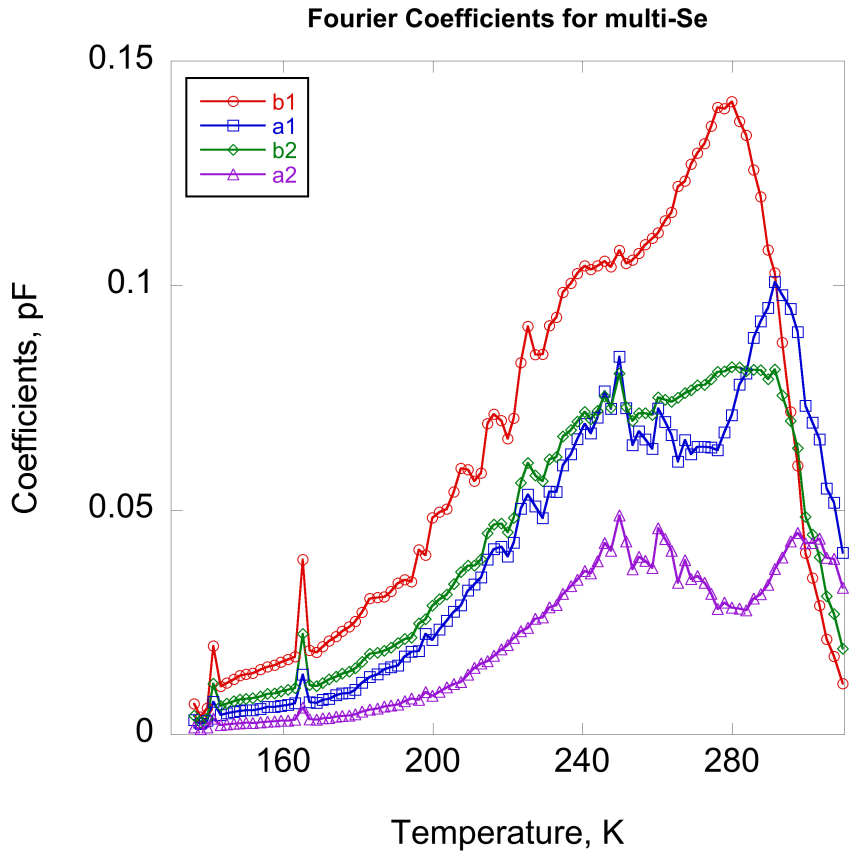

Figure 5.2: Fourier coefficients measured for superlattice Se on n-type Si substrate.

voltage (C-V) measurement was taken to determine the direction of bias for the reverse voltage. The reverse voltage V_R was set to -5 V with the pulse voltage at 0 V and a time window T_W of 20.48 ms. The resulting Fourier coefficients, shown in Fig. 5.2, were used to calculate the time constants and Arrhenius plots following the direct evaluation methods detailed in literature [11, 12].

5.3 Results

Superlattices are expected to exhibit quantum well levels or minibands due to the periodic structure. Using DLTS, we measured the energy levels of the occupied bands of the Si/superlattice-Se device [13]. The measurement procedure also used Fourier

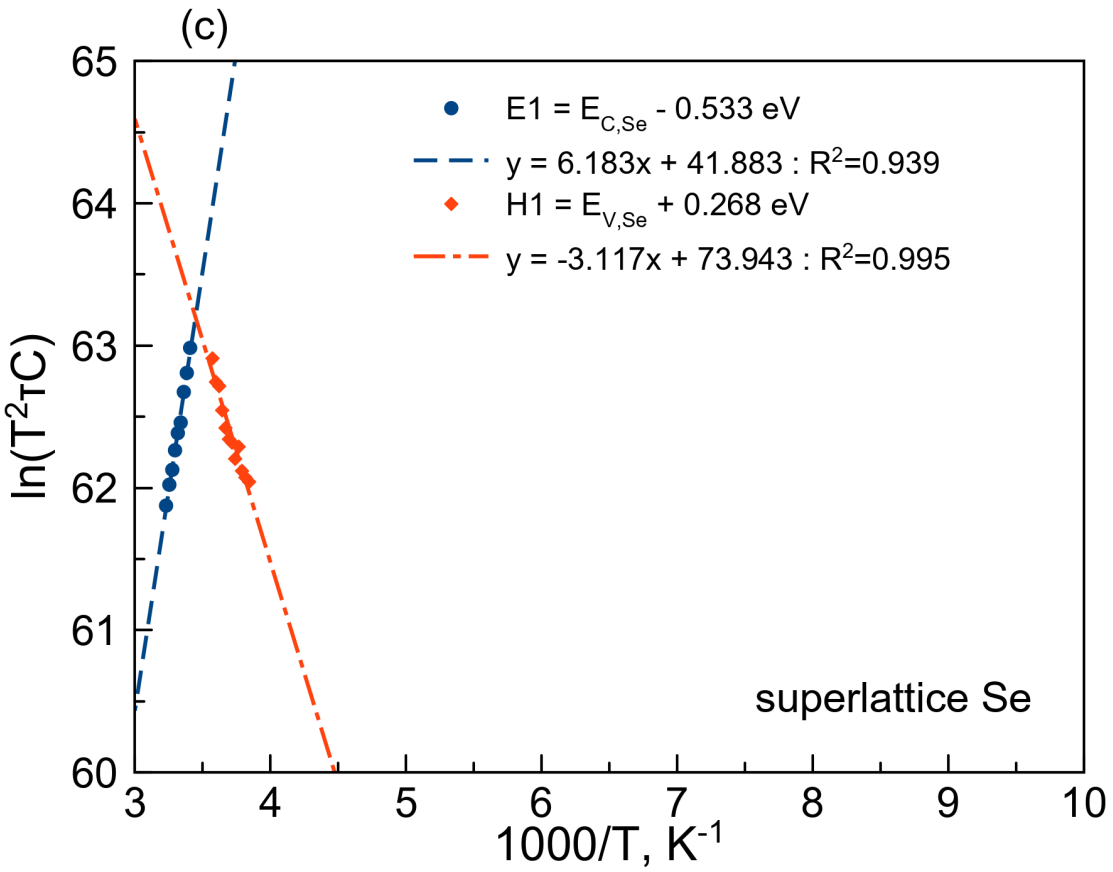

Figure 5.3: Linear fit lines to the Arrhenius plot obtained from the DLTS spectrum. The slopes of the lines give the minibands, $E1$ and $H1$, in the superlattice Se.

transformation of the measured transient, the analysis is presented in Appendix B. The resulting Fourier coefficients were used to calculate the time constants and Arrhenius plots following the direct evaluation methods detailed in literature [11, 12, 13]. The results of the evaluations are shown in Fig 5.3. They showed two occupied minibands at $E1 = E_{C,Se} - 0.533$ eV measured from the conduction band minimum of Se, and $H1 = E_{V,Se} + 0.269$ eV measured above the valence band maximum of Se. These occupied levels play an essential role in the transport characteristics of the Si/superlattice Se device when an external field is applied.

For I-V measurements, a contact of aluminium (Al) foil was placed on the superlattice Se film surface, with the Al foil contact attached to n-type Si side using silver (Ag) paste. Both contacts exhibit practically Ohmic behavior. The I-V characteristics of the superlattice Se samples were measured using a HP4140B controllable voltage

source and pico-ammeter. Measurements under dark conditions were performed with the sample enclosed in the HP 16055A test fixture dark box. The sample structure and connection schematic are shown in Fig. 5.4 (a). Under dark conditions, the I-V characteristics were measured for voltages from 0 V to +100 V and 0 V to −100 V. The results are shown in Fig. 5.4 (b). They show that when the n-type Si is negatively biased there is some oscillation in the I-V characteristic followed by an increase in the current from about 45 V. For positive applied bias the oscillation in the I-V persists longer with the exponential increase appearing at much higher applied field of about 85 V. The characteristic is asymmetric, showing about two orders higher current at −100 V compared to +100 V.

The heterostructural asymmetry can be used to further investigate the effect of injection rate on the I-V characteristics by applying a positive bias to the n-type Si so as to foster minority hole transport. Then illuminating the n-type Si surface with green light at 525 nm and power of 1 μW and 100 μW generates additional holes from photons absorbed in the n-type Si. The results are shown in Fig. 5.5.

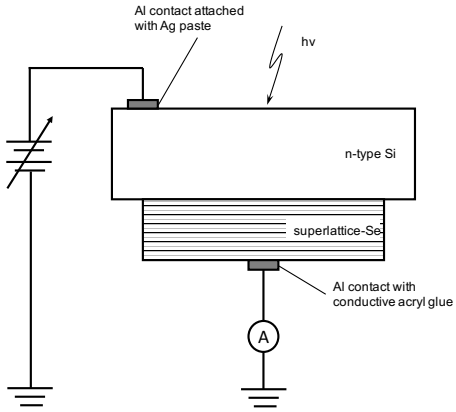

(a)

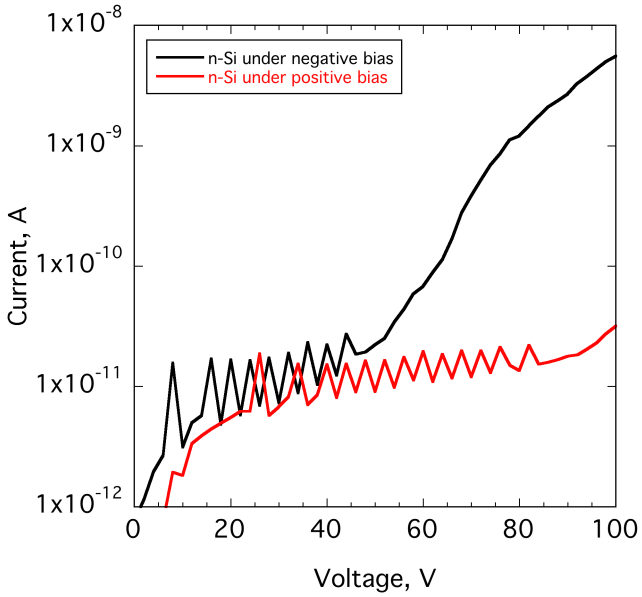

(b)

Figure 5.4: (a) The samples structure and connection schematic for I-V measurements of the superlattice Se device, and (b) the I-V characteristics of the superlattice Se device measured under positive and negative bias. The characteristic shows regions of oscillation where current decreases as the applied voltage increases.

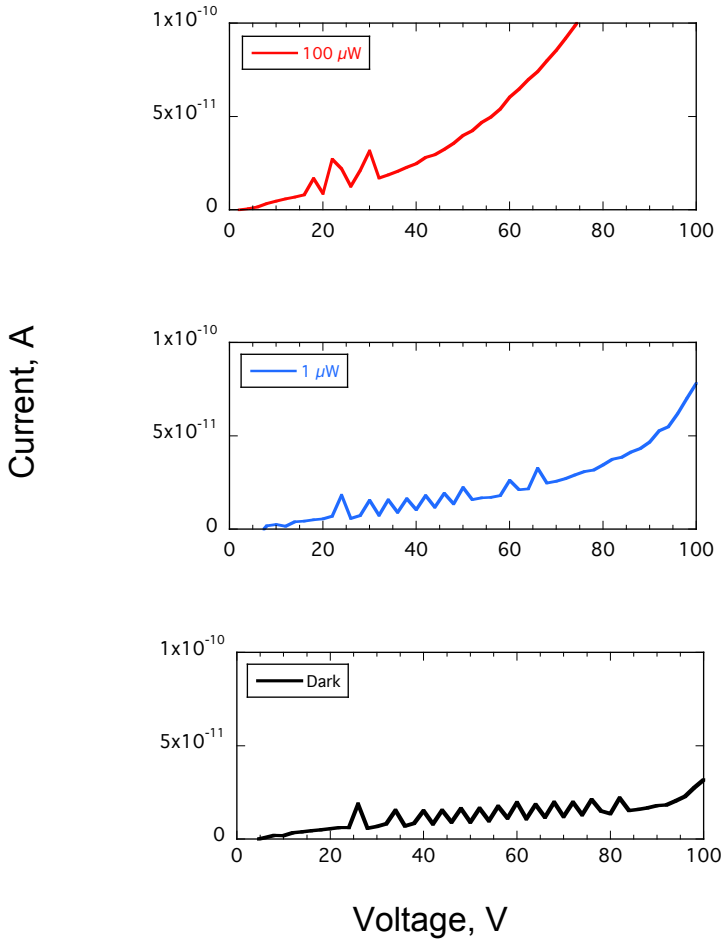

Figure 5.5: I-V characteristics of the superlattice Se device, with the n-type Si dark, and illuminated by green light (525 nm) at 1 μW and 100 μW. The number of peaks of oscillation is decreasing as the light power increases.

They show that the number of peaks decreases as the intensity of the light increases. The threshold voltage where the exponential increase in current begins is also lower for higher intensity light, about 70 V under 1 μW illumination and about 35 V under 100 μW illumination.

5.4 Discussion

The observations can be explained using a model adapted from the Metal-Insulator-Vacuum (MIV) and Schottky barrier models described in references [14, 15]. In these models, current transport is controlled by injection from back contact. In our case, there are two back contacts: first is the n-type Si back contact of the whole superlattice Se; and second, the occupied bands of individual quantum wells. The observed characteristics are an interplay between the rate of injection from the n-type Si and the rate of emission from occupied quantum well bands, as illustrated in Fig. 5.6.

The structure in flatband condition is shown in Fig. 5.6 (a). The band structure and Fermi level of Se were determined from Ultraviolet Photoelectron Spectroscopy (UPS), giving $E_{F,Se} = 0.8 \pm 0.1$ eV, comparable to values obtained in literature [16]. The Fermi level of As_2Se_3 was taken to be at the mid-gap as expected for chalcogenides [17, 18]. The periodic structure was then calculated using Anderson's rule, assuming that the Fermi level between the materials will be common since thermal equilibrium is achieved by carriers diffusing and/or tunneling across interfaces. This gave the periodic structure onto which the energy levels measured from DLTFS are visualized.

The initial conditions for the transport process are as follows. A field at the n-type Si back contact is established by leakage current due to residual tunneling and/or thermal generation, resulting in injection of carriers into the superlattice Se. As an external field is applied, the rate of injection increases, with carriers gradually filling unoccupied bands in the quantum wells of the superlattice Se. Simultaneously, the field causes barrier shifts and band bending on the Se barriers, with the As_2Se_3 quantum wells containing occupied bands behaving as a source of carrier injection, much like metals in metal/p-type semiconductor barriers.

By applying a negative bias to the n-type Si, the whole device is under forward bias, including individual quantum wells. This means that the barrier for electrons emitting to Se is reduced as more field is applied. Each level in the quantum well has a different barrier, with the highest bands having the lowest barrier height. Therefore, under a

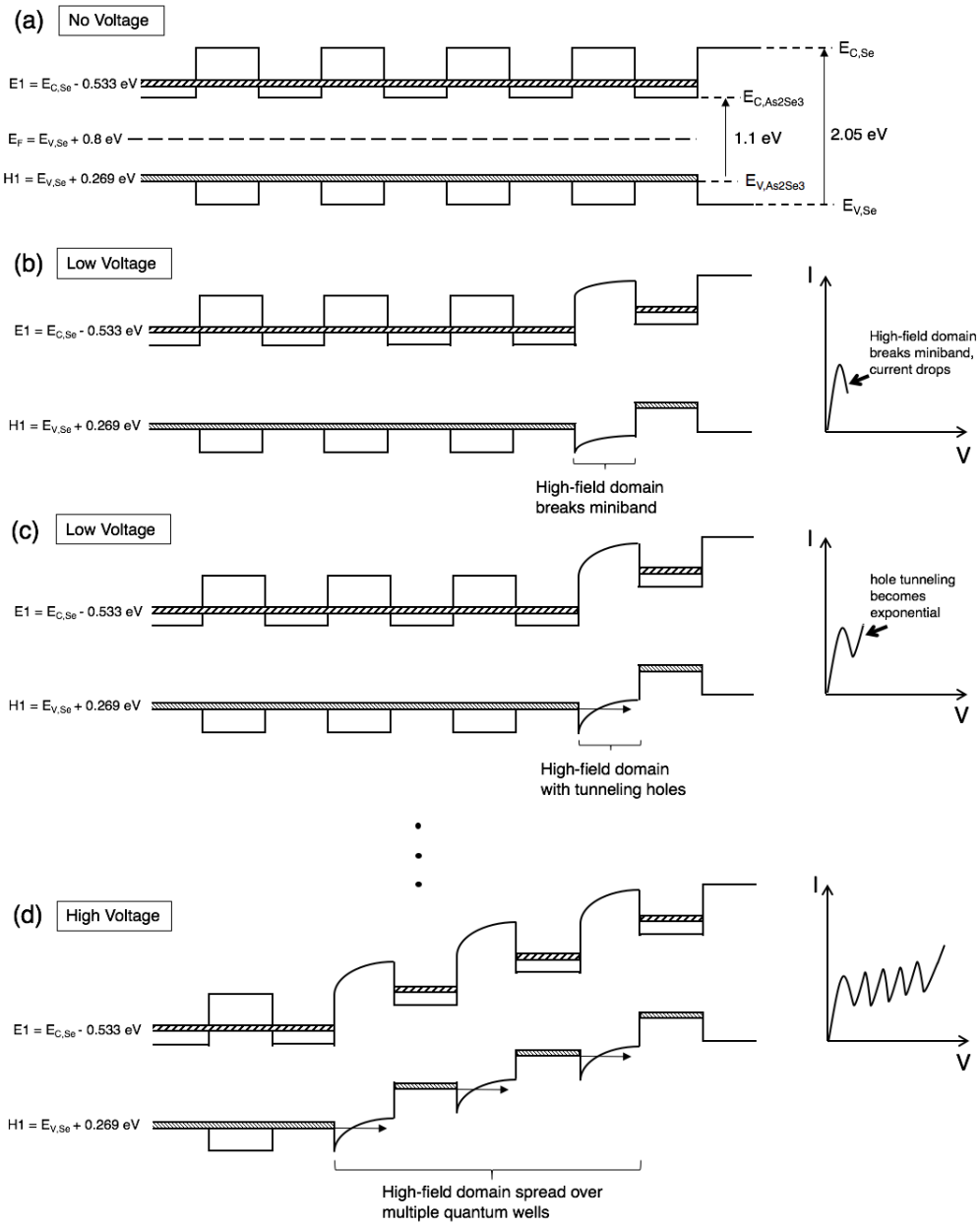

Figure 5.6: (a) The band diagram of the superlattice Se with the energy levels of the minibands obtained from DLTFS measurements, (b) the superlattice Se device with the n-type Si side under positive bias, with one region affected by a spontaneous high-field domain which breaks the miniband, and (c) the same region with holes tunneling though the Se barrier. Part (d) show the high-field domain spread over multiple quantum wells at high applied fields.

low rate of injection from n-type Si, emission will begin from the highest occupied band. This process occurs at each quantum well and cascades across the superlattice Se. As the field is increased, there is an exponential increase in the injection leading to an exponential increase in current flow.

For positive bias on the n-type Si the whole device is in reverse bias, including the individual quantum wells. In this case the band bending narrows the width of the barrier for holes tunneling into Se, as illustrated in Fig. 5.6 (b) and (c). The lowest occupied band has the highest tunneling probability. As the field increases across the structure, the tunneling probability increases and holes increasingly tunnel through the barrier resulting in an exponential increase in current flow.

The oscillation seen in the *I-V* characteristics (Fig. 5.4(b)) emanates from the appearance of high-field domains in the superlattice structure [19]. As a uniform field is applied across the device, a high-field domain will appear in some regions of the structure due to slight variations in the material distributions or random noise fluctuations. The region of the high-field domain will take a large proportion of the applied field and hence the cascade tunneling described before happens predominantly in this region. Figs. 5.6 (b) and (c) show one such region covering a single quantum well. The result is that there is a spike in the current the moment this phenomena happens. However, as the region is more conductive, the field relaxes. Nevertheless, the applied field also increases and the high-field domains will spread to other regions where the phenomena is repeated and more spikes appear in the *I-V* characteristic at increasing voltages (Fig. 5.6 (d)).

The number of peaks can be related to the number of such active regions of the quantum well structures. In this case this is the number of times the high-field domain activates some regions before the field is high enough for back contact injection to cause an exponential increase in the current. From *I-V* measurements of 2 μm samples (about 125 quantum wells) under positive bias there are about 12 - 14 peaks in the *I-V* characteristics. This suggests that the high-field domain appears 12 -14 times, over

one or more quantum well structures. Investigations are underway using methods such as Electron Beam Induced Current (EBIC) to verify these numbers. Nevertheless, a reasonable speculation is that the number of active regions of quantum wells is statistically related to the total thickness of the device with direct proportionality. Above a certain threshold, the applied field drives the back contact injection to exponential levels such that the conduction supersedes the cascade tunneling and thus the oscillations disappear. In the *I-V* characteristics of Fig. 5.4 (b) these thresholds are at about 45 V for negative bias and 85 V under positive bias.

The asymmetry in the *I-V* characteristics for positive compared to negative applied bias is explained by the difference in concentrations of majority and minority carriers in the n-type Si and their respective barrier heights with the superlattice Se. When the n-type Si is negatively biased, the majority electrons are driven towards the superlattice Se. Under low fields the barrier between n-type Si and superlattice Se is large such that there is a very low injection of electrons into the superlattice Se. As more field is applied, electrons will eventually be able to overcome the barrier and the injection rises exponentially since there is an excess of majority carrier electrons. After injection the carriers undergo the previously described cascading transport.

In the case of the n-type Si being positively biased, it is the minority holes that are driven towards the interface with the superlattice Se. These holes also face a barrier, which is lowered by the applied field, thereafter which the holes tunnel and cascade as discussed before. However, the minority carrier concentration is limited such that the injection rate remains low for longer before the exponential increase.

When the sample is illuminated, the light is expected to generate electron-hole pairs from photons absorbed in the n-type Si. The electron-hole pair is separated by the applied field and the hole drifts into the superlattice Se as described before. The illumination allows control of the injection rate by increasing the available minority holes. As is seen in the results in Fig. 5.5, as the intensity of 525 nm incident light increases from dark to 1 μW to 100 μW, there is an increase in holes and hole injection

results in the reduced number of oscillations, as well as the appearance of the exponential increase at much lower applied fields, as similarly observed for the majority carrier electrons.

For photo-detector applications, the heterostructural asymmetry is of interest for its blocking features, which are useful particularly for positive bias on the n-type Si. Using the same size contacts in terms of area, we measured at room temperature the resistivity of n-type Si and obtained a value of 9 Ωcm. The same procedure was performed for n-type Si with 2 μm superlattice Se and an effective resistivity of 2 $\times 10^{12}$ Ωcm was obtained. This suggests that the superlattice Se provides blocking features due to its well and barrier structure. In this case there is larger barrier for majority carrier electrons as more field is applied, both for the Si/superlattice Se interface and for individual well-barriers in the superlattice Se. This blocking of majority carriers means a reduced dark current and consequently low noise performance in photo-detector devices even at room temperature. Additionally, the asymmetry is known to improve photoconductivity by separating in space, the photogenerated holes from the electrons so that holes have a longer lifetime [20, 21].

Another well established and important feature of the superlattice Se device is avalanche multiplication, which gives the device inherent amplification capabilities. There have been attempts to explain these features using the Lucky drift model, Polaronic-Supersonic Transformations and the Cascade Multiplication model among others [4, 5, 6]. Here we highlight that Cascade Multiplication provides a clearer understanding of the origin of the avalanche features. The band arrangement of the superlattice predicts that under an applied field, generated holes become "hot" when they move from As_2Se_3 to amorphous Se and these hot holes are more likely to impact and ionize, producing a carrier multiplication. The superlattice model then clarifies why there is an exponential increase for higher applied fields. At low fields, the holes generated by impact ionization are "stuck" inside quantum wells and can only transport through sequential tunneling, which manifests as regions of negative resistance

and oscillations in the *I-V* characteristic. At high fields the barrier height for holes in the quantum wells is reduced such that they are able to overcome the barrier. Once over the barrier these holes also become hot when they move from As_2Se_3 to amorphous Se where impact ionization occurs. However, for high fields the holes from impact ionization also have a lower barrier height and continue the impact and ionization process resulting in an exponential increase. This gives a clear explanation along with evidence, for the phenomena suggested in the Cascade Multiplication model. It should therefore be possible to achieve variable amplification based on the number of active wells and barriers.

5.5 Conclusion

In conclusion, we investigated the electronic transport features of superlattice Se by measuring the *I-V* characteristics. The results showed oscillation in the *I-V* characteristics, a feature associated with sequential tunneling in superlattice structures. Measurements under illumination with visible light showed a reduction in the number of oscillation peaks as the intensity increased. The observations were explained by considering injection in a reverse bias Schottky barrier adapted for a series of well and barrier structures. The explanation also clarified the occurrence of avalanche multiplication which had been outlined earlier in the Cascade Multiplication model. The superlattice structure shows useful blocking and amplification features, which means it could be used as an "add-on" structure to photo-detector films. We are particularly interested in ultra-sensitive X-ray detectors and are investigating the effect of the "add-on" superlattice Se on Si as the X-ray absorbing film. The results discussed in this report already shows that such a device has low dark current due to its blocking capability, which makes it possible to obtain high SNR. With X-ray illumination, even though the attenuation depth of Si is limited, we expect significant photoconductivity from the amplification features of the "add-on" superlattice Se. Given that the structure is fabricated by rotational evaporation, we expect that superlattice-Se will be an

essential component to many types of wide area photo-detector materials such as CdTe or perovskites, significantly improving their SNR, and bringing closer the possibility of low dose, ultra-sensitive X-ray imaging.

References

[1] K. Tanioka, "Mechanism of the HARP imaging tube (translated)," *NHK Research News*, vol. 54, pp. 12–17, Jul 1994.

[2] M. J. Yaffe and J. A. Rowlands, "X-ray detectors for digital radiography," *Physics in Medicine and Biology*, vol. 42, pp. 1–39, Aug 1997.

[3] S. Kasap, J. B. Frey, G. Belev, O. Tousignant, H. Mani, J. Greenspan, L. Laperriere, O. Bubon, A. Reznik, G. DeCrescenzo, K. S. Karim, and J. A. Rowlands, "Amorphous and polycrystalline photoconductors for direct conversion flat panel X-ray image sensors," *Sensors*, vol. 11, pp. 5112–5157, May 2011.

[4] S. Kasap, J. Rowlands, S. D. Baranovskii, and K. Tanioka, "Lucky drift impact ionization in amorphous semiconductors," *Journal of Applied Physics*, vol. 96, pp. 2037–2047, Aug 2004.

[5] K. Tanaka, "A polaronic view of impact ionization in amorphous Se films," *Physica Status Solidi RRL*, vol. 11, pp. 1–3, Nov 2017.

[6] T. Masuzawa, S. Kuniyoshi, M. Onishi, R. Kato, I. Saito, T. Yamada, A. T. Koh, D. H. C. Chua, T. Shimosawa, and K. Okano, "Conditions for a carrier multiplication in amorphous-selenium based photodetector," *Applied Physics Letters*, vol. 102, no. 073506, pp. 1–4, 2013.

[7] I. Saito, T. Masuzawa, Y. Kudo, S. Pittner, T. Yamada, A. T. T. Koh, D. H. C. Chua, Y. Mori, D. R. T. Zahn, G. A. J. Amaratunga, and K. Okano, "Dura-

bility and photo-electric characteristics of a millie-feuille structured amorphous selenium (a-Se)-arsenic selenide (As_2Se_3) multi-layered thin film," *Journal of Non-Crystalline Solids*, vol. 378, pp. 96–100, Apr 2013.

[8] Y. C. Kim, H. Kim, K, D. Son, D. Jeong, J. Seo, I. T. Choi, Y. S. Han, Y. S. Lee, and N. Park, "Printable organometalic perovskite large-area, low-dose X-ray imaging," *Nature*, vol. 550, pp. 87–91, October 2017.

[9] J. A. Rowlands, "Material change for X-ray detectors," *Nature*, vol. 550, pp. 47–48, Oct 2017.

[10] G. Belev and S. Kasap, "Amorphous selenium as an X-ray photoconductor," *Journal of Non-Crystalline Solids*, vol. 345-346, pp. 484–488, 2004. Physics of Non-Crystalline Solids 10.

[11] M. Okuyama, H. Takakura, and Y. Hamakawa, "Fourier transformation analysis of deep level transient signals in semiconductors," *Solid-State Electronics*, vol. 26, pp. 689–694, Aug 1983.

[12] S. Weiss and R. Kassing, "Deep Level Transient Fourier Spectroscopy (DLTFS) - A technque for the analysis of deep level properties," *Solid-State Electronics*, vol. 31, pp. 1733–1742, Jun 1988.

[13] S. Q. Wang, F. Lu, H. D. Jung, C. D. Song, Z. Q. Zhu, H. Okushi, B. C. Cavenett, and T. Yao, "Electronic states in ZnSe/ZnTe type-II superlattice studied by capacitance transient spectroscopy," *Journal of Applied Physics*, vol. 82, no. 7, pp. 3402–3407, 1997.

[14] K. Okano, T. Yamada, A. Sawabe, S. Koizumi, J. Itoh, and G. A. J. Amaratunga, "Metal-insulator-vacuum type electron emission from N-containing chemical vapor deposited diamond," *Applied Physics Letters*, vol. 79, pp. 275–277, Jul 2001.

[15] M. W. Geis, N. N. Efremow Jr, K. E. Krohn, J. C. Twichell, T. M. Lyszczarz, R. Kalish, J. A. Greer, and M. D. Tabat, "Theory and experimental results of a

new diamond surface-emission cathode," *The Lincoln Laboratory Journal*, vol. 10, pp. 3–15, Oct 1997.

[16] G. S. Belev, *Electrical properties of amorphous selenium based photoconductive devices for application in X-ray image detectors*. PhD thesis, Department of Electrical and Computer Engineering, University of Saskatchewan, Saskatoon, SK, Canada, Jan 2007.

[17] M. Abkowitz, "Density of states in a-Se from combined analysis of xerographic potentials and transient transport data," *Philosophical Magazine Letters*, vol. 58, no. 1, pp. 53–57, 1988.

[18] N. F. Mott, "Electrons in non-crystalline materials: The last twenty five years," *Contemporary Physics*, vol. 26, pp. 203–215, Mar 1985.

[19] L. Esaki and L. L. Chang, "New transport phenomenon in a semiconductor "superlattice"," *Physical Review Letters*, vol. 33, pp. 496–498, Aug 1974.

[20] B. Abeles, "Amorphous semiconductor superlattices," *Superlattices and Microstructures*, vol. 5, pp. 473–480, Jul 1989.

[21] H. Kroemer, "Heterostructure devices: a device physicist looks at interfaces," *Surface Science*, vol. 132, pp. 543–576, 1983.

Chapter 6

Quantum device designing for future semiconductor engineering

6.1 Introduction

From the diode, transistor, thyristor, to the superlattice of Esaki, there is a trend that as the layers of a semiconductor device are increased, so does the functionality [1, 2, 3, 4]. Capasso proposed that this multiplicity of layers and materials presents opportunities to engineer the band structure of semiconductor structures and thus customize the features as required by applications [5]. Nevertheless, this form of band engineering usually requires selection of lattice-matched materials, and fabrication by Molecular Beam Epitaxy (MBE) or Atomic Layer Deposition (ALD), meaning there is a high technological barrier for widespread application of the concept. We explore a different design approach, using amorphous materials with no need for lattice matching, and fabrication using the technologically simple method of rotational evaporation. We adopted well-established amorphous materials Se and As_2Se_3 which have been applied for high sensitive photo-detectors and flat panel X-ray imagers [6, 7, 8]. In previous work, we showed that the multi-layer structure of amorphous Se and As_2Se_3 exhibits quantum features of confined energy levels and oscillations in current-voltage (I-V) characteristics, and showed that the carrier multiplication in these devices is related to the multi-layer structure [9, 10]. We presented a model that explained the transport properties as emanating from (1) generation in the absorbing material, and injection into the superlattice Se, (2) transport via sequential tunneling across Se barriers, and (3) energy gain at band discontinuities and impact ionization [11]. The model is summarized in Fig. 6.1. Based on this model we create a design paradigm for photodetectors where the photon absorbing material is chosen depending on the application wavelength, and the multiplication factor is determined from the desired application sensitivity *.

*Patent pending Number PCT/JP2020/032600

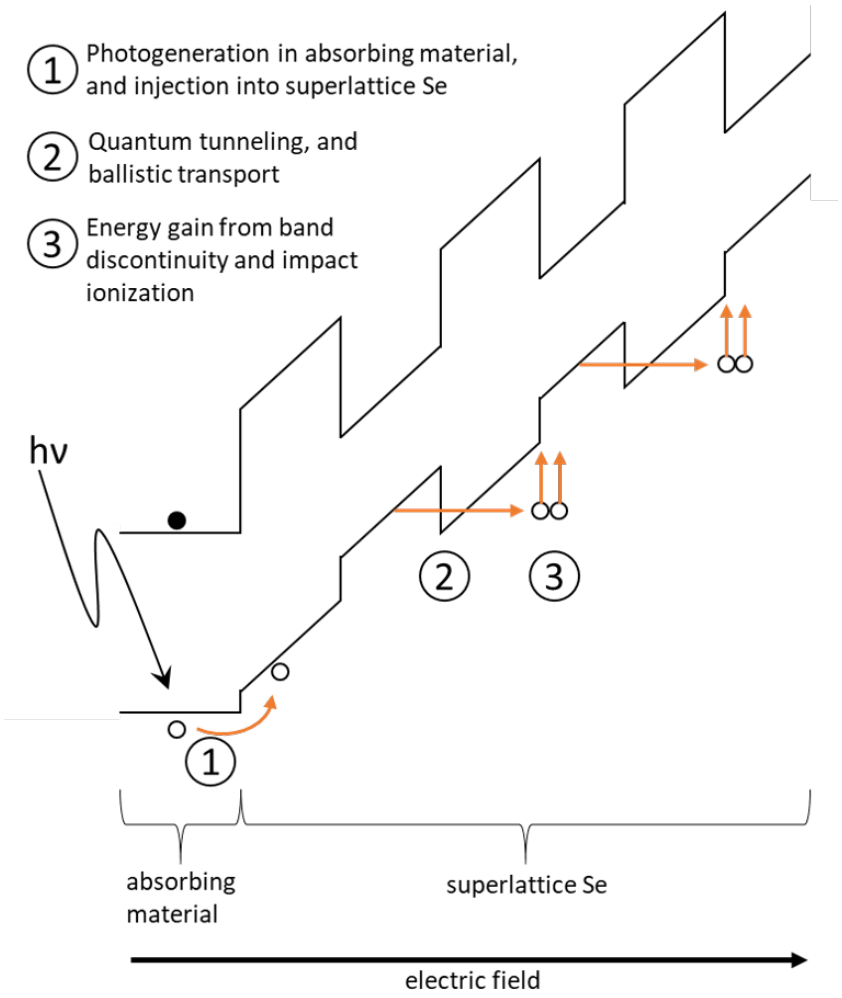

Figure 6.1: The band diagram of the superlattice Se structure under an applied field. The transport process is initiated by (1) photo-generation in the absorbing material (for example Si) and injection into the superlattice Se, (2) quantum tunneling across Se barriers and ballistic transport, (3) energy gain at band discontinuities, and impact ionization.

6.2 Design

The model presents design options for the absorbing material and the multiplication factor. Depending on the wavelength, the appropriate photon absorbing material can be chosen. Photon absorption spectra can be used to determine the optimum choice of material, for example InSb for infrared, Si for visible light, or Ge or high-Z materials for X-ray detection. For noise blocking, this material must either (1) have a narrow band gap such that its Fermi level aligning with that of Se leaves a sufficiently high barrier to block electrons entering the superlattice Se, or (2) be n-doped so that the Fermi level once again aligns leaving a high barrier for electrons. For carriers in the absorbing material, there are at least two possible ways for carriers to transit into the superlattice Se, either by thermionic emission over the Se barrier, or by quantum tunneling across the barrier via internal field emission. A band structure of the absorbing material/superlattice Se heterojunction can be drawn following Anderson's rule and assuming a common Fermi level from a thermal equilibrium achieved by carriers distributing by diffusion, residual tunneling and random thermal generation [12]. Thermionic emission follows a probability $\exp(-\frac{\Phi}{k_B T})$, while for internal field emission, the tunneling probability follows $\exp(-\frac{\Phi^{\frac{3}{2}}}{F})$, where Φ is the barrier height, k_B is the Boltzmann constant, T is the absolute temperature, and F is the applied field [13, 14]. We consider the cases for both electrons and holes with the device under dark conditions and under illumination on the n-type Si side.

Under dark conditions, electrons in the conduction band of the absorbing material face a high barrier according to the band structure of Fig. 6.1, meaning a low probability of thermal emission at 300 K. The tunneling probability is also low even as the applied field increases. When the applied field is positive, this has an effect of increasing the barrier for electrons even further (Fig. 6.1). Therefore the injection of electrons into the superlattice Se is significantly blocked. In this way, superlattice Se can act as a blocking layer, reducing the effect of thermal noise generated electrons.

On the other hand, minority holes in the valence band encounter a relatively small

barrier, which means holes are significantly injected into the superlattice Se largely by thermal generation. When the absorbing material is irradiated, electron hole-pairs are generated. As in the case under dark conditions, the photo-carrier electrons are blocked, while photo-generated holes are injected into the superlattice Se. This has the effect of separating in space, the transport of holes from that of electrons [15, 5].

In the periodic structure, a situation analogous to the absorbing material/Se barrier obtains at each interface of the As_2Se_3 quantum well to Se barrier. With reference to Fig. 6.1, and assuming occupation of the lowest energy level only, electrons at that level face a high barrier (0.533 eV from DLTS measurements), which means a low probability of thermal emission and tunneling when a positive bias is applied. Holes have a comparatively lower barrier (0.269 eV from DLTS measurements) for both thermal emission and tunneling [11]. Since the tunneling probability increases with applied field, it more likely that holes will transit through the barrier by quantum tunneling through internal field emission.

From the model it follows that the multiplication factor, M, is related to the number of Se barriers, N, encountered during the sequential tunneling transport process. This relationship can be expressed as $M = kN$, where k is a parameter describing some physical properties of the superlattice, which will be discussed later. Assuming a uniformly distributed field across the superlattice Se, and one impact ionization event at each barrier then $M = N$ and $k = 1$. For this case, we define a threshold field which can be estimated by considering the mean free path between collisions, the tunneling distance, barrier, height, and barrier width (6 - 9 nm) [16, 10]. The mean free path for amorphous Se is reported to be about 2.6 - 6 nm [17, 18]. Using the lower limit of the mean free path, and taking a barrier height of about 0.269 eV, the threshold field is $\approx$ 42 $\times 10^6$ Vm^{-1}.

Generated carriers will also take a time t to transit through the superlattice Se structure. This transition time is also related to the number of layers in the superlattice Se. The transition time $t = \frac{L}{v_d}$ where v_d is an average drift velocity and L is the total

thickness of the superlattice. Since the wells and barriers have similar width l, the total thickness can be expressed as $L = 2Nl$. Thus the transition time also depends on the number of Se barriers, N. This implies that there is a trade-off between M and t, such that increasing M by increasing the number of layers will also increase the transit time, thereby lowering the device response time. There is therefore need to optimize the performance with regards to sensitivity and response time.

Using the procedure above, we designed and fabricated a quantum-tunneling-assisted multiplication photo-detector (QMAP) for 525 nm 100 μW light. Based on absorption spectra, and electron blocking considerations we chose n-type Si as the absorbing material. A model of the device is shown in Fig. 6.2. Light is incident on the n-type Si side, and absorption occurs in the Si. The absorption profile in Si can be calculated using the Beer-Lambert law

$$\frac{I}{I_0} = \exp\left(-\alpha_{Si} x\right) \tag{6.1}$$

where x is the depth of penetration into the Si. For 525 nm light, the absorption coefficient $\alpha_{Si} = 8320.5$ cm^{-1}[19]. The absorption profile is shown in Fig. 6.3. The majority (99 %) of the photons incident onto the surface of the Si are absorbed within the first 10 μm.

The resulting carriers will then be transported by drift and diffusion mechanisms. We are interested in the drift and diffusion of minority carrier holes towards the superlattice Se. For a hole generated at a depth x in the absorbing material of total thickness L, the collection efficiency due to drift of photogenerated holes at the superlattice surface can be calculated from the Hecht formula [8, 20]

$$CP_{drift}(x) = \frac{\mu_{h,Si}\tau_{h,Si}F_{Si}}{L}\left[1 - \exp\left(-\frac{L-x}{\mu_{h,Si}\tau_{h,Si}F_{Si}}\right)\right] \tag{6.2}$$

Here $\mu_{h,Si}$ and $\tau_{h,Si}$ are the mobility and the lifetime for the minority holes, respectively [13]. To estimate the field in Si, F_{Si}, we assumed the sample structure as a series resistance connection between Si and the amorphous Se superlattice as shown

in Fig. 6.2. The superlattice Se has a high resistivity ($\approx$ 1 GΩ·cm) compared to the absorbing material Si ($\approx$ 10 Ω·cm for n-type Si). Considering these resistivities and the dimensions of the materials, at an applied voltage of 100 V across the whole device, the voltage distributed in the Si is $V_{Si} \approx 10\mu$V. As such, the majority of the applied field is distributed across the superlattice Se. The collection probability for holes generated within nanometer depths from the surface in the Si to reach the superlattice interface due to drift is $\approx$ 0.01 %.

For diffusion, assuming a zero surface recombination velocity, a collection probability can be calculated indicating how likely a carrier generated at a depth x will be collected at the boundary of a material with a total thickness L [21]:

$$CP_{diffusion}(x) = \exp\left(-\frac{(L-x)}{L_{Diff}}\right) \tag{6.3}$$

where $L_{Diff} = \sqrt{D_{h,Si}\tau_{h,Si}}$ is the diffusion length, $D_{h,Si}$ is the diffusivity of minority holes in Si, and $\tau_{h,Si}$ is the lifetime for the minority holes. The diffusivity $D_{h,Si}$ is calculated from the Einstein relation, and the lifetime $\tau_{h,Si}$ =2.5 $\times 10^{-3}$ s [13]. The collection probabilities of carriers generated within the first 10 μm from the surface of incidence are shown in Fig. 6.4. Carriers generated within nanometer depths from the surface have a probability of over 0.74 of reaching the boundary with the superlattice Se. Carriers that reach this boundary have a chance to be injected into the superlattice where carrier multiplication phenomena happen.

A band structure of the n-type Si/superlattice Se heterojunction was drawn following Anderson's rule and assuming a common Fermi level from a thermal equilibrium achieved by carriers distributing by diffusion, residual tunneling and random thermal generation. Figure 6.5 shows the band structure for n-type Si and superlattice Se in flat band condition. The Fermi level of the n-type Si was calculated from the resistivity (5 Ω·cm) and doping type, that of Se was determined from ultraviolet photo-electron spectroscopy (UPS) at 0.8 eV, and that of As_2Se_3 at the mid gap [11, 22, 23].

For a multiplication gain of $M = 12$, with a barrier width of 8 nm, the total thickness

following from $M = kN$ was 200 nm, taking $k = 1$. Similarly, to obtain a gain of $M = 125$, 2 μm superlattice Se is required. Thus, samples of n-type Si/superlattice Se with superlattice Se total thickness of 200 nm and 2 μm were fabricated using classical rotational evaporation and then characterized using current voltage (I-V) and current time (I-T) measurements.

6.3 Materials and Methods

Using rotational evaporation technique, samples with multi-nanolayers of amorphous Se and As_2Se_3 were fabricated. Details of the rotational evaporation process can be found in Chapter 2 [24].

6.3.1 n-type Si substrate preparation

The substrates were 10 mm square dices n-type Si (100), 5 - 8 Ω·cm, single side polished wafers. The Si substrates were cleaned in an ultrasonic bath using acetone, methanol and de-ionized water, and then immersed in 25 % diluted HF to remove surface oxide. The cleaned Si substrates were then attached to circular glass holders and placed into the rotational evaporation system, with the mirror polished surface as the target for deposition.

6.3.2 Rotational evaporation

The evaporation chamber was immediately pumped to high vacuum. When the target chamber pressure of 10^{-6} Torr was reached, the turntable holding the substrates was rotated at 80 rpm, so that the substrates trace a circular path, passing over two heated boats containing the evaporating materials. Using boat shutters, the deposition was controlled so that the first layer deposited on to the substrates was Se, as well as stopping the deposition when the target total thickness was reached. The deposition thickness was measured using a crystal oscillator which traced the same circular path

as the samples. In this way, samples with target thicknesses of 2 μm and 200 nm were fabricated.

6.3.3 Current-voltage (I-V) and current-time (I-T) measurements

Current-voltage (I-V) and current-time (I-T) characteristics were then measured for each type of sample after making electrical contacts to the samples using a W whisker to the n-type Si side and a 2 mm square graphene on Cu pad to the superlattice Se side. Given the temperature sensitivity of amorphous Se, which changes to crystalline phase at temperatures above 320 K, it was necessary to find a material that makes good ohmic contact without needing thermal annealing. Graphene has been reported to show good ohmic contact as an inserted contact in heterostructure device [25, 26]. We used a 2 mm square Graphenea CVD graphene on Cu pad to contact the superlattice Se side. To verify the nature of the contact, two graphene on Cu pads 1 mm apart were used as contacts to amorphous Se grown on quartz glass. The schematic of the setup is shown in Fig. 6.6. With this setup, I-V characteristics were measured on the HP4140B with voltages varying from -100 V to $+100$ V. The results are shown in Fig. 6.7. The current varies linearly with voltage, confirming a practically Ohmic contact between the graphene and the amorphous Se.

The n-type Si/superlattice Se samples were contacted using a W whisker on the n-type Si side and graphene on Cu on the superlattice Se side, and the device I-V characteristics measured on the HP4140B system. The measurement setup schematic is shown in Fig. 6.8. The 200 nm superlattice Se samples were measured with voltages varying from 0 V to +10 V in 0.1 V steps. The 2 μm samples were measured from 0 V to +100 V in 1 V steps.

With the same contacts, the sample I-T characteristics were also measured by streaming pulses of 525 nm 100 μW light on to the n-type Si side. The pulse stream was obtained by chopping the light from the laser diode using a rotating disk with a 3

mm through hole, with the disk rotating at 7200 rpm. The pulse duration was 89.51 μs. The schematic of the I-T measurement setup is shown in Fig. 6.9. The variation of output current with time was measured on an Agilent 54624A oscilloscope. The applied voltage across the sample was varied from +6 V to +10 V in 1 V steps for 200 nm samples, +60 V to +100 V in 10 V steps for 2 μm samples.

6.4 Results and Discussion

Samples of n-type Si/superlattice Se were characterized using I-V measurements under dark conditions and with the sample illuminated by a 100 μW 525 nm light. The results are shown in Fig. 6.10. There is a clear distinction between current in dark conditions and under illumination for both types of samples. This difference appears to be larger for the 2 μm samples compared to 200 nm. Under illumination, the I-V characteristic for the 2 μm sample also exhibits "steps" at 29 V and 40 V. These "steps" are associated with tunneling of carriers from occupied quantum well levels. Carriers photo-generated in the Si are injected into the superlattice where they occupy energy levels from the lowest one first. As the applied bias increases, the probability of tunneling across the triangular barrier increases. We calculated the energy levels, assuming the longest tunneling distance of 8 nm at each applied field, giving energy levels at 0.134 eV and 0.09 eV from the bottom of the As_2Se_3 quantum well for 29 V and 40 V applied bias respectively. The energy levels in the superlattice can be calculated using the Kronig-Penney model, taking the effective mass for holes at $0.27m_0$ and valence band discontinuity $\Delta E_V = 0.25$ eV, giving levels at 0.016 eV, 0.064 eV, 0.141 eV and 0.236 eV. Levels measured from the I-T characteristics are relatable to the levels calculated using the Kronig-Penney model at 0.064 eV and 0.141 eV respectively. At 45 V, the current feature resembles a series resistance limited model, where emission is now occurring from all occupied levels and the current is now only limited by the material transport characteristics. Similar "steps" could not be observed clearly in 200 nm samples. We speculate that for the same photon rate and injection, the narrower

superlattice had a reduced number of available states such that all energy levels were occupied, and the transport characteristic became dominated by thermionic emission, thus could not exhibit any tunneling emission features.

The samples were also characterized using I-T measurements by sending a stream of 100 μW 525 nm light pulses to the n-type Si side and measuring the output voltage at the output of a transimpedance amplifier with a 1 MΩ feedback resistor. The results are shown in Fig. 6.11. The results show the output voltage increasing in response to an incident pulse, and decaying after the pulse is released. For both samples, the magnitude of photo-response gets larger as the applied voltage across the sample increases. However, the 200 nm sample shows the dark current also increasing with applied voltage, in contrast to the 2 μm sample where the dark current remains low.

From these results, the multiplication factors for the 200 nm and 2 μm superlattice Se, M_{200nm} and $M_{2\mu m}$ respectively, were calculated using $M = \frac{\Delta I}{qN_0}$. Here ΔI is the difference between the dark current and photon induced current, N_0 is the number of photons.

The multiplication factors for 200 nm superlattice Se, M_{200nm}, and 2 μm superlattice Se, $M_{2\mu m}$, (about 12 and 125 Se barriers respectively) are shown in Fig. 6.12.

M_{200nm}, and $M_{2\mu m}$ are both greater than 2 from about 4×10^7 Vm^{-1} indicating a sufficient field to trigger multiplication events in at least one barrier of the superlattice. At the highest applied field of 5×10^7 Vm^{-1} during the measurements, M_{200nm}, and $M_{2\mu m}$ are 11 and 48 rounded to the nearest integer, respectively. This gives k_{200nm} of 0.916, and $k_{2\mu m}$ of 0.384. A $k_{2\mu m}$ which is significantly less than one suggests that multiplication events did not occur at most of the Se barriers. This can be explained by variations in the field distribution across the comparatively thicker superlattice Se. The appearance of static domains which cause uneven field distributions in superlattice structures has been discussed in literature [4, 27, 28]. These high field domains are often associated with non-uniformity in the structure of the superlattice. In our

case these may be small nanocrystal phases at interfaces or in some layers. As such, the parameter k may contain information on these non-uniformities which may be remedied by better fabrication methods. Having k_{200nm} close to 1 offers some support for this notion, reasonably assuming that in fabricating a fewer number of layers, the probability of irregularities between layers was reduced. Further investigation into the distribution of the field in the superlattice Se using methods such as cathodoluminescence spectroscopy or electron beam induced current (EBIC) is planned. We also are interested in characterizing multiplication factors for superlattice devices fabricated using a range of fabrication techniques, among them, high precision methods such as molecular beam epitaxy (MBE).

We thus expect that an ideal $k \geq 1$ if the field is evenly distributed, or modified such that some barriers perform at much higher multiplication rates. A realizable approach to controlling field in the superlattice is to add a third terminal along the transport axis of the superlattice. Such a terminal has to be carefully designed so that it does not inject additional carriers into the superlattice. If the multiplication factor can be controlled by a third electrode then the device can be configured for automatic gain control. Cases in which $k \geq 1$ imply that a certain multiplication factor M can be achieved for less number of layers N, which would reduce the device form factor.

The transit time for carriers across the superlattice Se was estimated from the decay of the transient when the light pulse is removed. The transit time was measured as the time it takes for the current to reduce to half its value from the time the light pulse was removed. The results of the decay times are shown in Fig. 6.12 (a). As the applied field is increased, the decay times decrease, indicating a faster response. This is due to an increase in the drift velocity v_d since it is related to applied field E and mobility μ as $v_d = E\mu$ [13]. The decay times are longer for the thicker 2 μm superlattice Se samples compared to the 200 nm samples. There is therefore a trade-off between getting a high multiplication factor by increasing the layer numbers, and the response time of the device. This is shown in Fig. 6.12 (b), where for the same

multiplication factor, say 10, the 200 nm sample has a response time which is about 1.5 times faster compared to the 2 μm sample. Thus the device design can be optimized for performance both in terms of multiplication factor and response time. Again, the trade-off in response time suggests that thinner samples would offer better performance if $k \geq 1$ with an additional advantage in form factor. We are investigating further the components contributing to the parameter k, as well as the possibility of controlling and increasing it.

We are investigating further the absorbing material, considering direct band gap materials such as GaAs and InSb and how this affects detection efficiency for visible and infrared light. We are also exploring high-Z materials such as CdTe and perovskites, towards detection of high energy photons. We also expect the superlattice structure to provide significant improvements in noise performance and signal multiplication if it can be added to standard p-n and p-i-n photodetector structures. This makes the superlattice a solid state amplifier, analogous to photomultiplier devices.

6.5 Conclusion

Based on the sequential quantum tunneling model for superlattice Se, we developed a design method for achieving a desired performance. Using $M = kN$, the device multiplication gain, M, can be predetermined by selecting the number of layers in the superlattice, N. However, as the number of layers increases, so does the transition time. The quantum tunneling assisted multiplication phenomenon discussed provides a platform for engineering the device performance characteristics. The additive nature of the superlattice Se means that there are many choices for the absorbing material, which can be chosen based on application. We are currently exploring devices using n-type Ge/superlattice Se for X-ray detection. In general, for photoelectronics applications, after link budget analysis determining the required detector operating wavelength and sensitivity, the photo-detector matching the required performance by providing the appropriate read out signal level can be optimally fabricated. If a third

terminal is added along the transport axis the multiplication gain could be controlled. Additionally and it also makes possible a quantum tunneling assisted transistor with high input impedance and customized gain. Another possible application is in opto-electronic switches where the sensitivity and response times can be customized. There are still issues with non-uniformities in structure and field distribution which are being investigated further. Nevertheless, the design method outlined herein provides a platform for applying quantum effects to device designing, and obtaining additional functionality from semiconductor devices even with technologically simple fabrication methods and materials. We hope this discussion reinvigorates investigations into band engineering techniques and inspires the engineering of practical quantum features for semiconductor devices.

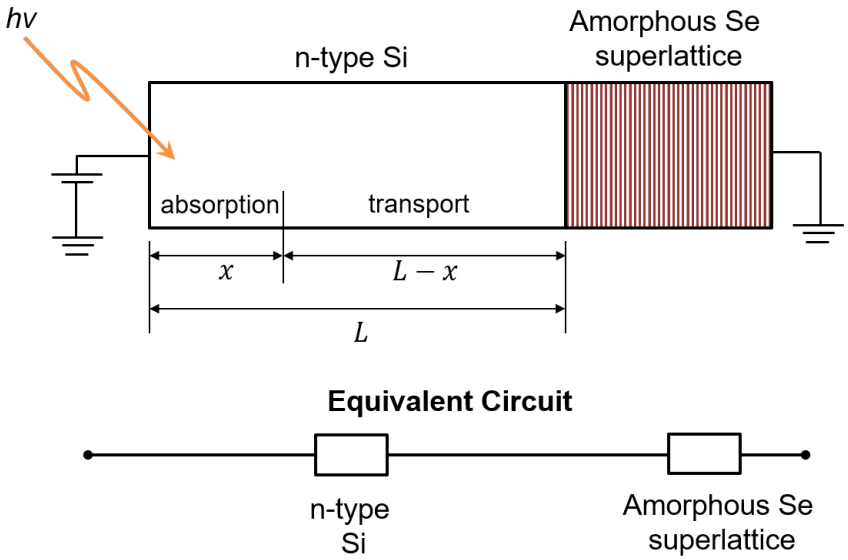

Figure 6.2: A model for the n-type Si/superlattice Se device showing regions of absorption and transport of the photo-generated carriers. The device is taken as an equivalent circuit of two resistors connected in series.

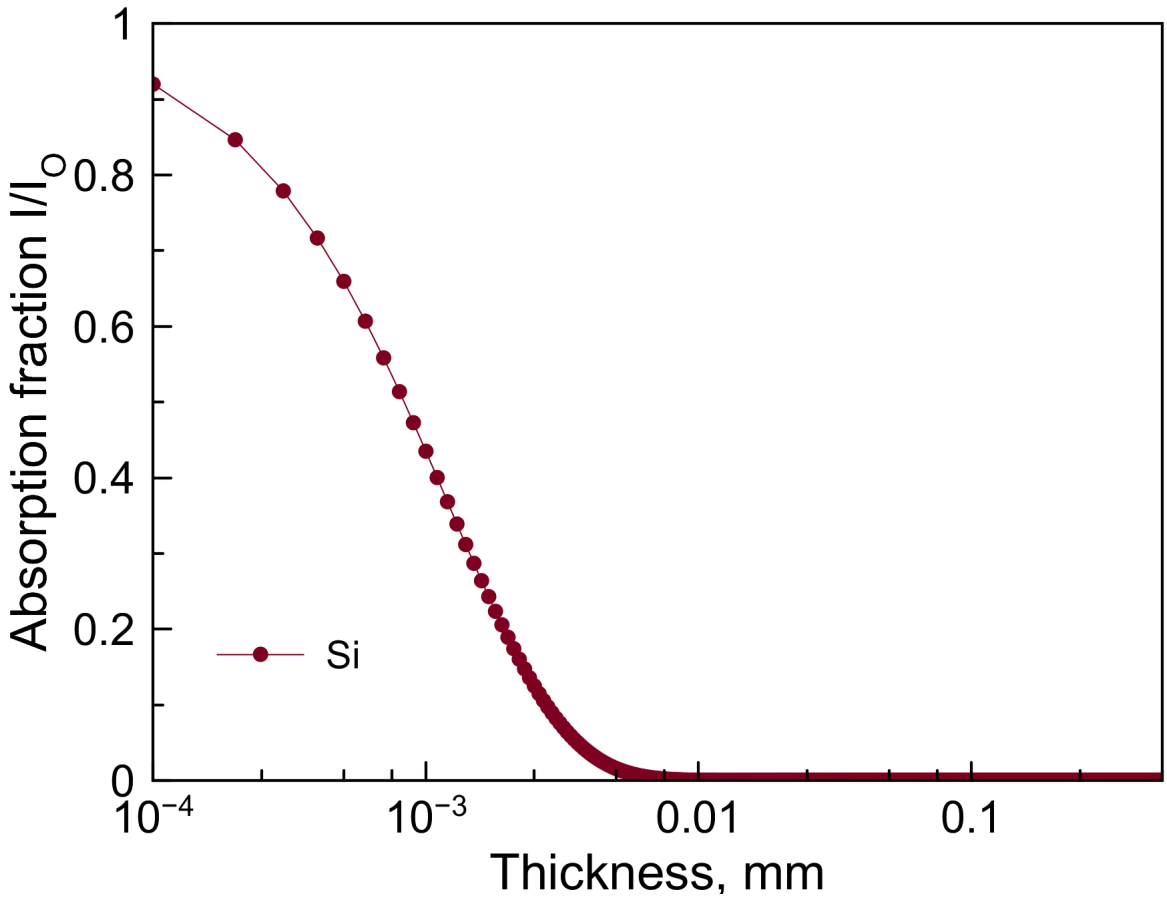

Figure 6.3: The absorption profile of 0.5 mm Si for 525 nm light (absorption coefficient $\alpha = 8320.5$ cm^{-1}). 99 % of the absorption occurs within 10 μm from the surface of incidence.

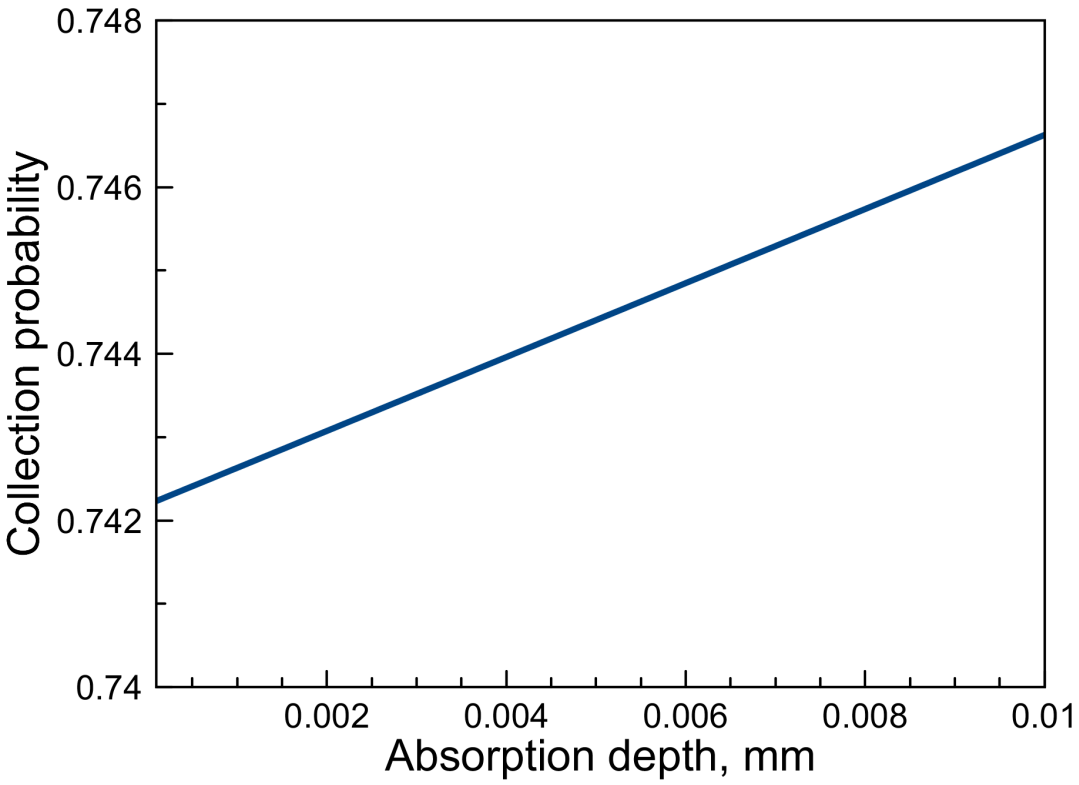

Figure 6.4: The minority carrier collection probability for holes generated in 0.5 mm thick n-type Si within 10 μm from the surface of incidence. Here, collection refers to the holes traversing to the boundary with the superlattice Se.

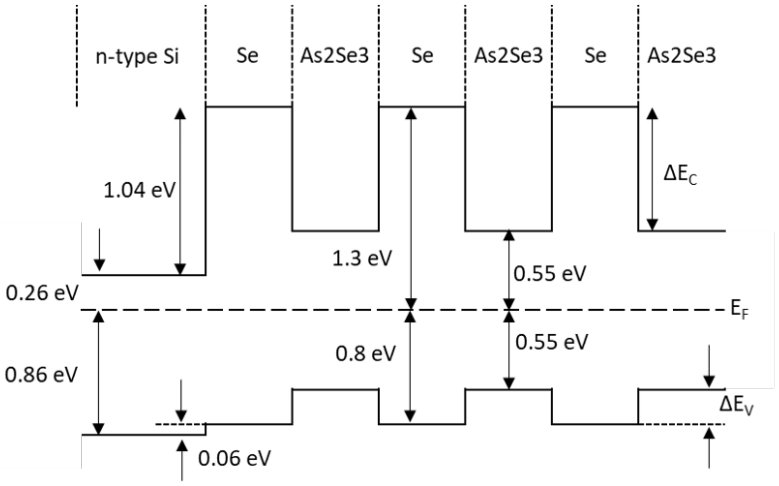

Figure 6.5: The band structure of the n-type Si/superlattice Se structure under flat band conditions.

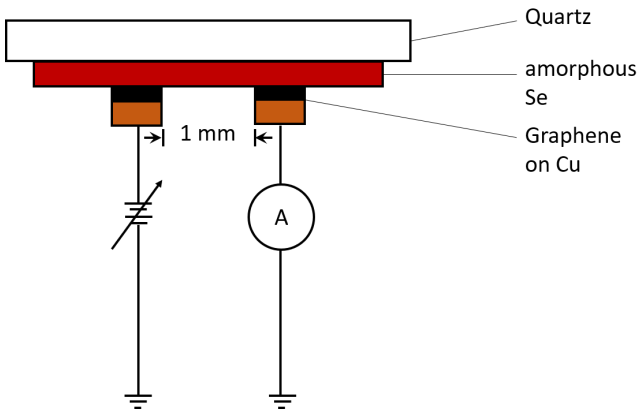

Figure 6.6: Set up to verify the graphene/amorphous Se contact. Two graphene on Cu pads 1 mm apart were used as contacts to amorphous Se grown on quartz glass, and current-voltage (I-V) characteristics measured with voltages varying from -100 V to $+100$ V. The results are shown in Fig. 6.7

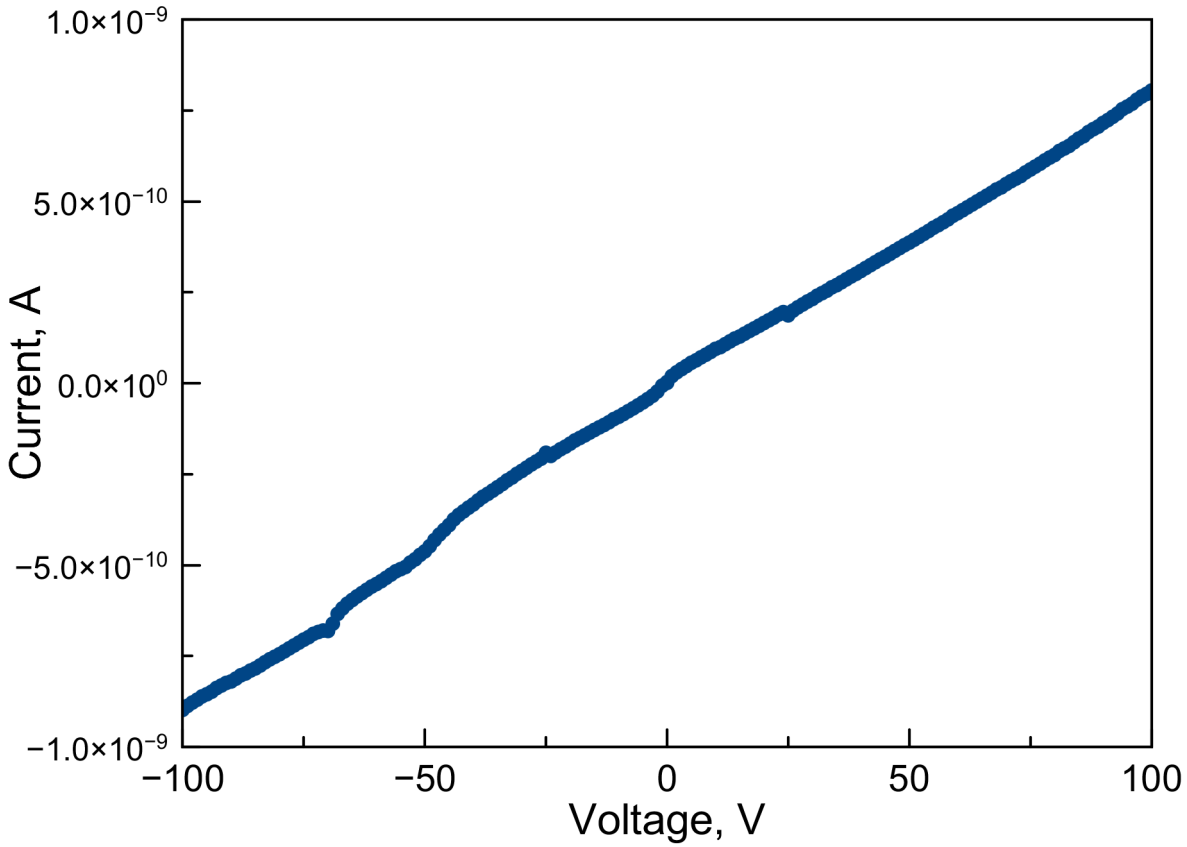

Figure 6.7: Current-voltage (I-V) characteristics measured for graphene on Cu contact to amorphous Se showing Ohmic contact between graphene and amorphous Se.

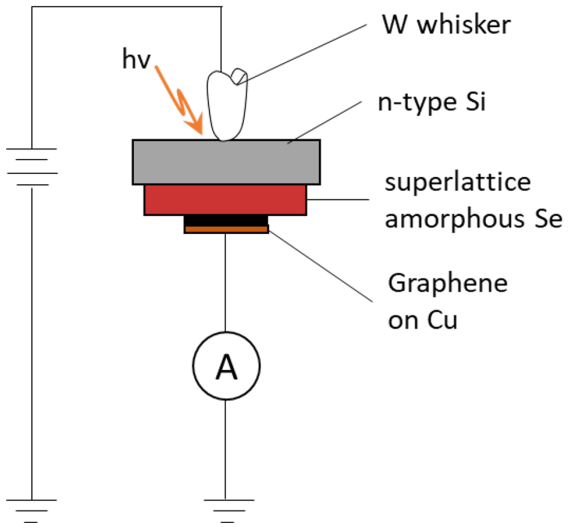

Figure 6.8: Schematic of the current-voltage ($I - V$) measurements of n-type Si/superlattice Se samples on the HP4140B system. The n-type Si side was contacted using a W whisker, and the superlattice Se was contacted using graphene. I-V characteristics were measured under dark conditions and under illumination with 100 μW 525 nm light.

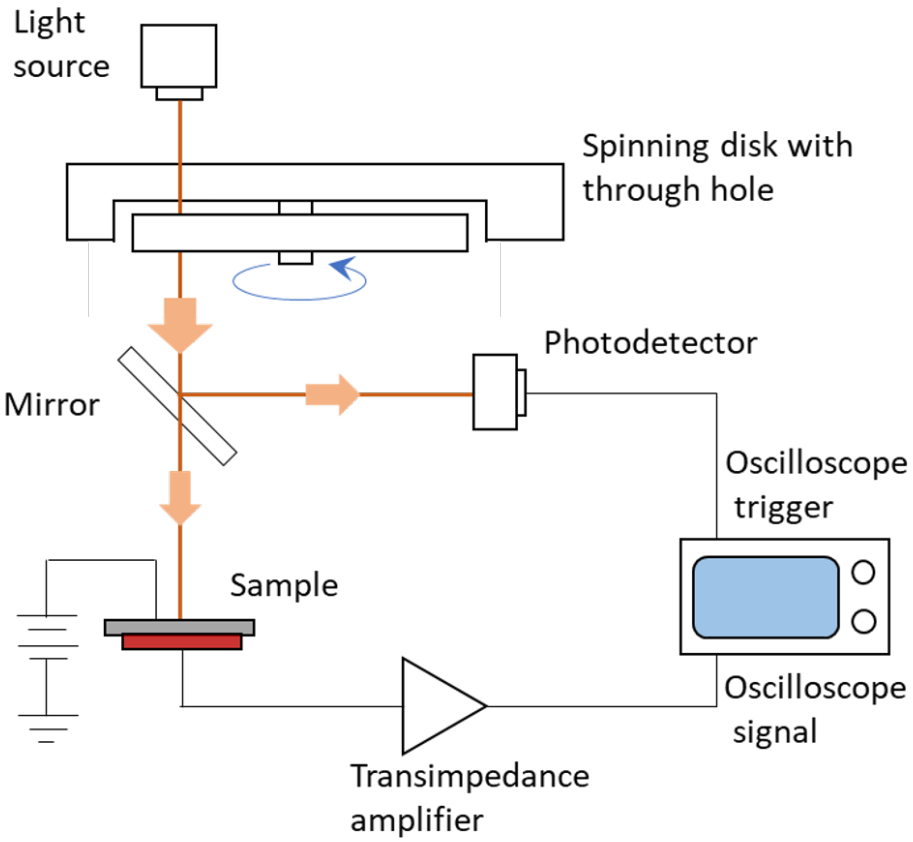

Figure 6.9: Measurement of current-time (I-V) characteristics by streaming pulses of 525 nm light onto the n-type Si side and measuring the output current variation on an Agilent 54624A oscilloscope. The measurements were done with the samples at an applied bias, +6 V to +10 V in 1 V steps for 200 nm samples, +60 V to +100 V in 10 V steps for 2 μm samples.

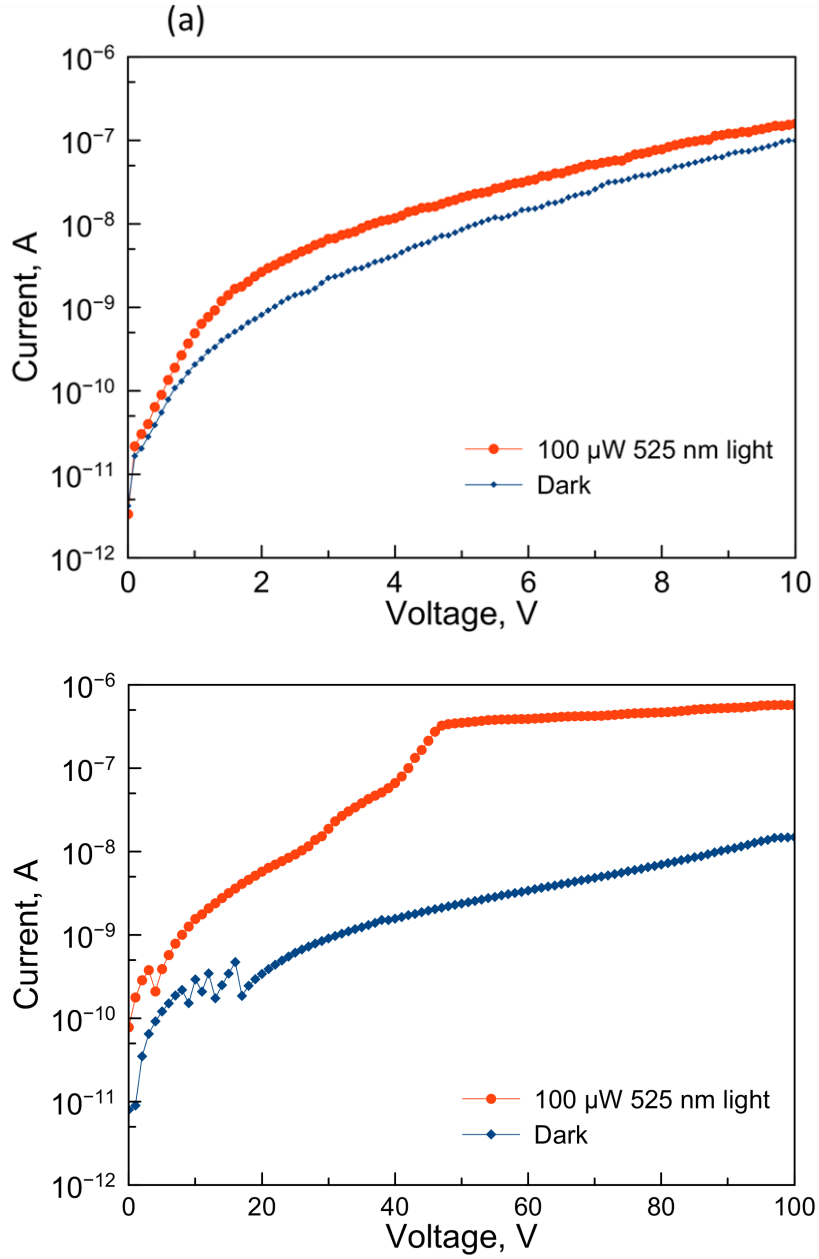

Figure 6.10: Current-voltage I-V characteristics measured for n-type Si/superlattice Se (a) 200 nm superlattice Se, and (b) 2 μm superlattice Se samples under dark conditions and irradiated by a 100 μW 525 nm light.

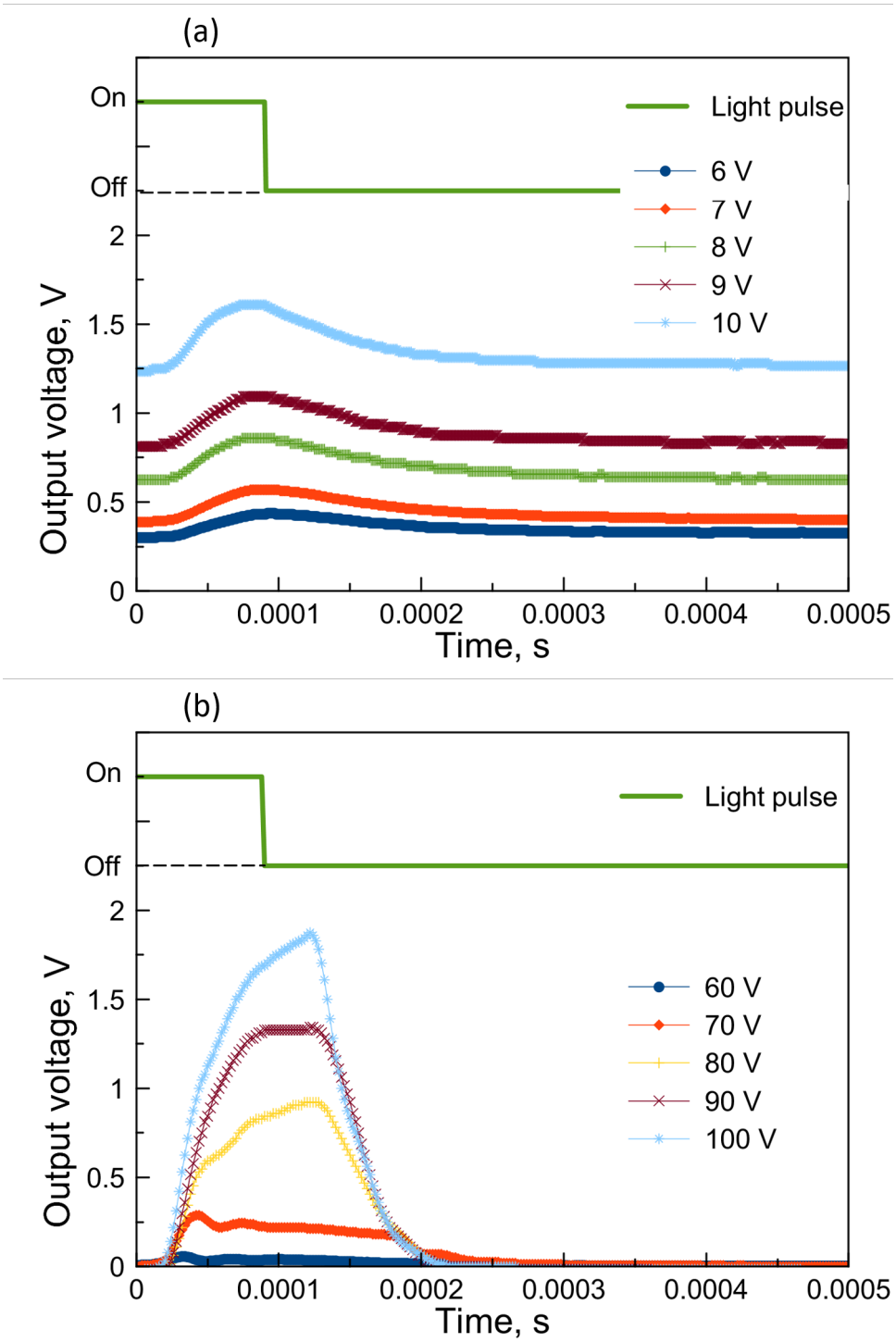

Figure 6.11: Current-time (I-T) characteristics measured for n-type Si/superlattice Se (a) 200 nm superlattice Se, and (b) 2 μm superlattice Se samples with the n-type Si side illuminated by a stream of pulses of 100 μW 525 nm light.

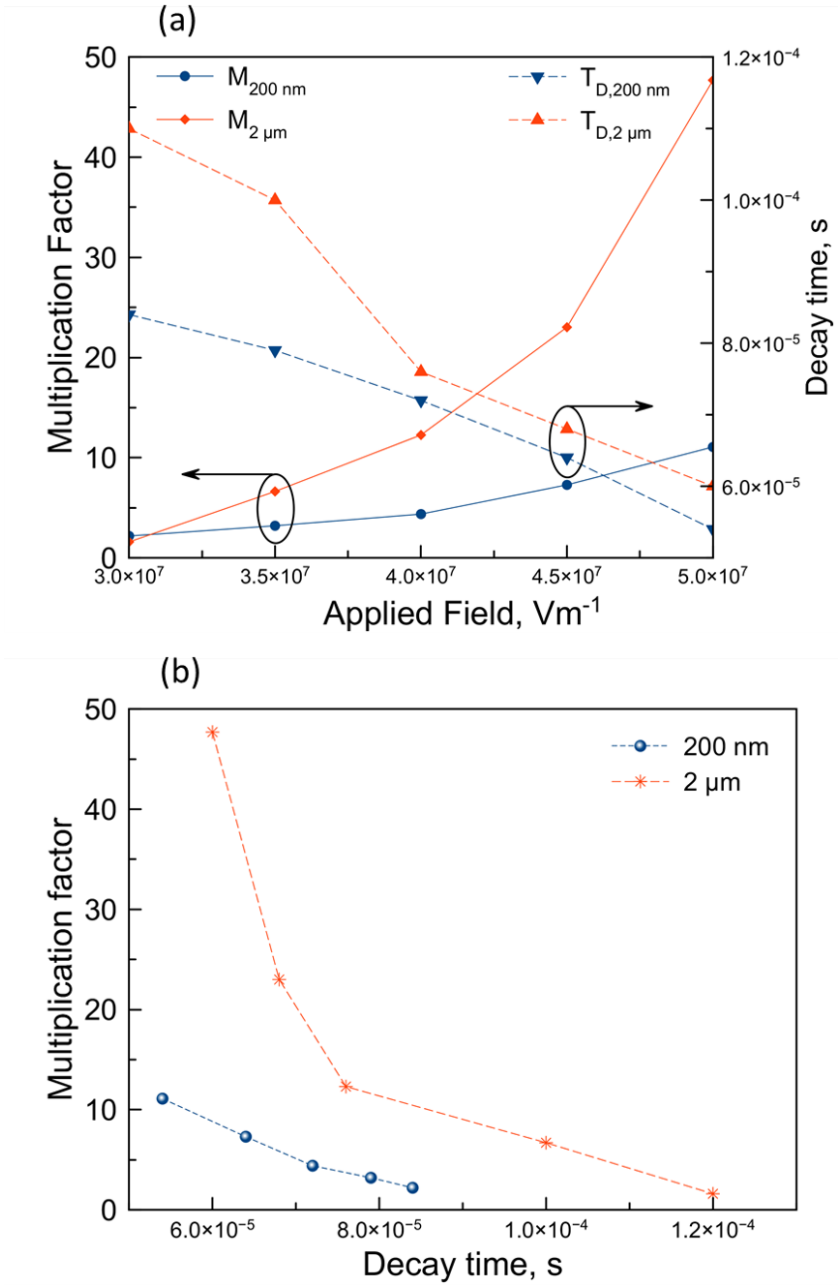

Figure 6.12: (a) The multiplication factors and decay times for n-type Si/superlattice Se samples with 200 nm and 2 μm thick superlattice. The multiplication factor is larger for the thicker samples, while the decay times are longer for thicker samples. In (b), the multiplication gain M is shown against the decay time. For a similar M between the 200 nm and 2 μm superlattice Se, the decay time is longer for the thicker sample. In both figures, the lines joining the points are to guide the reader's eye, and do not represent intermediate values.

References

[1] W. Shockley, "The theory of p-n junctions in semiconductors and p-n junction transistors," *The Bell System Technical Journal*, vol. 28, no. 3, pp. 435–489, 1949.

[2] J. Bardeen and W. H. Brattain, "The transistor, a semi-conductor triode," *Phys. Rev.*, vol. 74, pp. 230–231, Jul 1948.

[3] J. L. Moll, M. Tanenbaum, J. M. Goldey, and N. Holonyak, "P-N-P-N transistor switches," *Proceedings of the IRE*, vol. 44, no. 9, pp. 1174–1182, 1956.

[4] L. Esaki, "Advances in semiconductor superlattices, quantum wells and heterostructures," *Journal de Physique Colloques*, vol. 45, pp. C5–3–C5–21, Apr 1984.

[5] F. Capasso, "Band-gap engineering: From physics and materials to new semiconductor devices," *Science*, vol. 235, no. 4785, pp. 172–176, 1987.

[6] K. Tanioka, "Ultra-high-sensitivity new Super-HARP pickup tube," in *Proc. 2001 IEEE Workshop CCD and Advanced Image Sensors*, pp. 216–219, IEEE, 2001.

[7] T. Masuzawa, I. Saito, T. Yamada, M. Onishi, H. Yamaguchi, Y. Suzuki, K. Oonuki, N. Kato, S. Ogawa, Y. Takakuwa, A. Koh, D. Chua, Y. Mori, T. Shimosawa, and K. Okano, "Development of an amorphous Selenium-based photodetector driven by a diamond cold cathode," *Sensors*, vol. 13, pp. 13744–13778, Oct 2013.

[8] S. Kasap, J. B. Frey, G. Belev, O. Tousignant, H. Mani, J. Greenspan, L. Laperriere, O. Bubon, A. Reznik, G. DeCrescenzo, K. S. Karim, and J. A. Rowlands,

"Amorphous and polycrystalline photoconductors for direct conversion flat panel X-ray image sensors," *Sensors*, vol. 11, pp. 5112–5157, May 2011.

[9] T. Masuzawa, S. Kuniyoshi, M. Onishi, R. Kato, I. Saito, T. Yamada, A. T. Koh, D. H. C. Chua, T. Shimosawa, and K. Okano, "Conditions for a carrier multiplication in amorphous-selenium based photodetector," *Applied Physics Letters*, vol. 102, no. 073506, pp. 1–4, 2013.

[10] J. D. John, S. Okano, A. Sharma, O. Selyshchev, M. Rahaman, N. Miyachi, K. Enomoto, J. Ochiai, G. Saito, Ichitaro Salvan, T. Masuzawa, T. Yamada, D. H. C. Chua, D. R. T. Zahn, and K. Okano, "Observation of two-level defect system in amorphous Se superlattices," *Applied Physics Letters*, vol. 116, p. 192104, 2020.

[11] J. D. John, S. Okano, A. Sharma, O. Selyshchev, M. Rahaman, N. Miyachi, K. Enomoto, J. Ochiai, I. Saito, T. Masuzawa, T. Yamada, D. H. C. Chua, D. R. T. Zahn, and K. Okano, "Transport properties of Se/As_2Se_3 nanolayer superlattice fabricated using rotational evaporation," *Advanced Functional Materials*, vol. 29, no. 40, p. 1904758, 2019.

[12] R. L. Anderson, "Experiments on Ge-GaAs heterojunctions," *Solid-State Electronics*, vol. 5, pp. 341–351, 1962.

[13] S. M. Sze, *Physics of semiconductor devices*. Wiley, New York, 1990.

[14] A. Modinos, *Field, Thermionic, and Secondary Electron Emission Spectroscopy*. Plenum Press, New York, 1984.

[15] B. Abeles, "Amorphous semiconductor superlattices," *Superlattices and Microstructures*, vol. 5, pp. 473–480, Jul 1989.

[16] I. Saito, T. Masuzawa, Y. Kudo, S. Pittner, T. Yamada, A. T. T. Koh, D. H. C. Chua, Y. Mori, D. R. T. Zahn, G. A. J. Amaratunga, and K. Okano, "Durability and photo-electric characteristics of a millie-feuille structured amorphous

selenium (a-Se)-arsenic selenide (As_2Se_3) multi-layered thin film," *Journal of Non-Crystalline Solids*, vol. 378, pp. 96–100, Apr 2013.

[17] K. Tanaka, "Avalanche breakdown in amorphous selenium (a-Se) and related materials: Brief review, critique, and proposal," *Journal of Optoelectronics and Advanced Materials*, vol. 16, pp. 243–251, Apr 2014.

[18] S. Kasap, J. Rowlands, S. D. Baranovskii, and K. Tanioka, "Lucky drift impact ionization in amorphous semiconductors," *Journal of Applied Physics*, vol. 96, pp. 2037–2047, Aug 2004.

[19] M. A. Green and M. J. Keevers, "Optical properties of intrinsic silicon at 300 K," *Progress in Photovoltaics: Research and Applications*, vol. 3, no. 3, pp. 189–192, 1995.

[20] S. Kasap, M. Z. Kabir, K. O. Ramaswami, R. E. Johanson, and R. J. Curry, "Charge collection efficiency in the presence of non-uniform carrier drift mobilities and lifetimes in photoconductive detectors," *Journal of Applied Physics*, vol. 128, no. 12, p. 124501, 2020.

[21] C. Donolato, "On the analysis of diffusion length measurements by SEM," *Solid-State Electronics*, vol. 25, no. 11, pp. 1077–1081, 1982.

[22] M. Abkowitz, "Density of states in a-Se from combined analysis of xerographic potentials and transient transport data," *Philosophical Magazine Letters*, vol. 58, no. 1, pp. 53–57, 1988.

[23] N. F. Mott, "Electrons in non-crystalline materials: The last twenty five years," *Contemporary Physics*, vol. 26, pp. 203–215, Mar 1985.

[24] I. Saito, W. Miyazaki, M. Onishi, Y. Kudo, T. Masuzawa, T. Yamada, A. Koh, D. Chua, K. Soga, M. Overend, M. Aono, G. A. J. Amaratunga, and K. Okano, "A transparent ultraviolet triggered amorphous selenium p-n junction," *Applied Physics Letters*, vol. 98, p. 152102, Apr 2011.

[25] P. S. Park, K. M. Reddy, D. N. Nath, Z. Yang, N. P. Padture, and S. Rajan, "Ohmic contact formation between metal and AlGaN/GaN heterostructure via graphene insertion," *Applied Physics Letters*, vol. 102, pp. 153501–1 – 153501–4, Apr 2013.

[26] H. Zhong, Z. Liu, L. Shi, G. Xu, X. Fan, Z. Huang, J. Wang, G. Ren, and K. Xu, "Graphene in ohmic contact for both n-GaN and p-GaN," *Applied Physics Letters*, vol. 104, pp. 212101–1 – 212101–4, Mar 2014.

[27] H. T. Grahn, *Hot electrons and space-charge waves in superlattices.* Clarendon Press, Oxford, 1998.

[28] A. Wacker, "Semiconductor superlattices: a model system for nonlinear transport," *Physics Reports*, vol. 357, no. 1, pp. 1–111, 2002.

Chapter 7

X-ray detector device based on the amorphous Selenium superlattice

7.1 Introduction

In the current Covid-19 pandemic, X-ray imaging has proved to be a useful modality for monitoring the progression of the disease in the patient's chest as the patient undergoes treatment [1, 2, 3]. In such cases, repeated measurements are necessary in short spans of time to track the progression of pneumonia symptoms and provide effective treatment to patients. However, such accumulated exposure to X-rays is risky due to the ionizing nature of the radiation, with a likely increase in the prevalence of cancer. Therefore, it is necessary to reduce the total exposure by reducing the dosage per reading from the X-ray source. This is only possible if the corresponding detector is sensitive enough to produce a good quality signal for the reduced number of source photons. Direct conversion detectors, which directly convert incident X-ray photons into charges, offer improvement in sensitivity and response [4, 5]. Amorphous Se is one of the well established materials for direct X-ray detection, and has been applied for practical flat panel X-ray imagers (FPXI) [6, 7]. Progress is being made in developing high-Z materials and perovskite based detectors [8, 9, 10, 11]. Nevertheless, conventional materials Si and Ge are still significant for developing practical devices.

We have developed a design paradigm for photo-detectors where the photon absorbing material is chosen depending on the application wavelength, and the multiplication factor is determined from the desired application sensitivity*. A detector can then be optimally fabricated using the appropriate absorbing material and the appropriate number of layers of the superlattice Se. We apply this method to design a sensitive detector for X-rays by considering the appropriate absorbing material and the required noise suppression and signal gain to successfully detect X-rays.

A lowered X-ray dose requires that its signal be resolvable above the dark current noise. For this reason, devices using high purity mono-crystalline intrinsic semiconductors are preferable, for example high purity Ge (HPGe) [4]. We consider Ge as the absorbing material due to its comparably high attenuation factor for X-rays with

*Patent pending Number PCT/JP2020/032600

energies below 100 keV. Fig. 7.1 shows the linear absorption coefficients of 0.5 mm thickness Si and Ge up to 100 keV using data from the National Institute of Standards and Technology (NIST) database [12]. Ge is also preferable since it is a 'conventional' material, with well established methods of purification and fabrication such that high purity mono-crystalline forms of the material are reasonably available. Conventional materials may also allow fabrication, on the same wafer, of other passive and active components for readout and signal processing.

For a detector device fabricated using Ge, the dark current performance can be improved by cooling, since the intrinsic carrier concentration, $n_i \propto \exp(\frac{E_G}{2k_BT})$ where E_G is the band gap, k_B is the Boltzmann constant and T is the absolute temperature [4, 13]. If however, the majority carrier concentration N_D can be blocked, then the dark current emanates from the minority carriers. In this case, the noise can be lower compared to that caused by intrinsic carriers. For an n-type semiconductor, the minority carrier concentration, $p_0 = \frac{n_i^2}{N_D}$, at equilibrium, where n_i is the intrinsic carrier concentration and N_D is the dopant concentration [13]. For n-type Ge at 300 K, with $N_D = 2.48 \times 10^{14}$ cm^3 (measured from Hall effect), p_0 is one order lower compared to n_i. Thus an effective blocking structure could significantly improve the noise performance. We consider the superlattice Se structure as a blocking device [14]. Using Anderson's rules, a band structure of the n-type Ge/superlattice Se device was drawn, assuming a common Fermi level from a thermal equilibrium achieved by diffusion, residual tunneling and/or random thermal generation [15]. The Fermi level of the n-type Ge was calculated from the Hall measured carrier concentration, N_D, that of Se was determined from ultraviolet photo-electron spectroscopy (UPS) at 0.8 eV, and that of As_2Se_3 at the mid gap [14, 16]. Fig. 7.2 shows a band structure of n-type Ge/superlattice structure under flat band conditions. The barrier for majority carrier electrons is 1.04 eV, which is high enough to limit thermal emission of electrons at room temperatures and lower into the superlattice Se.

In addition to suppressing dark currents, the superlattice Se offers possible multipli-

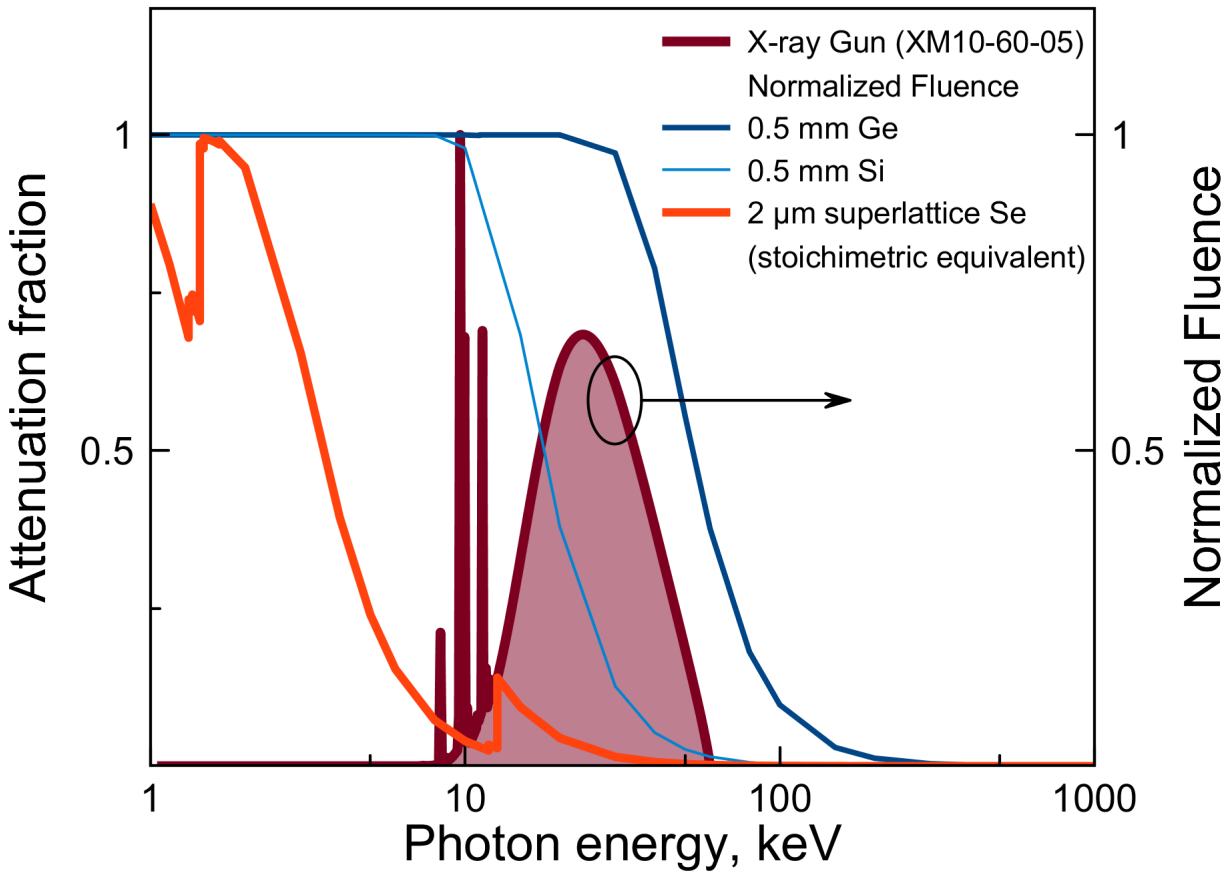

Figure 7.1: The attenuation fractions of Ge and Si for high energy photons. The normalized fluence of the X-ray source used in the experiments is included for reference. 0.5 mm Ge is sufficient to cover the spectrum of available photons from the source.

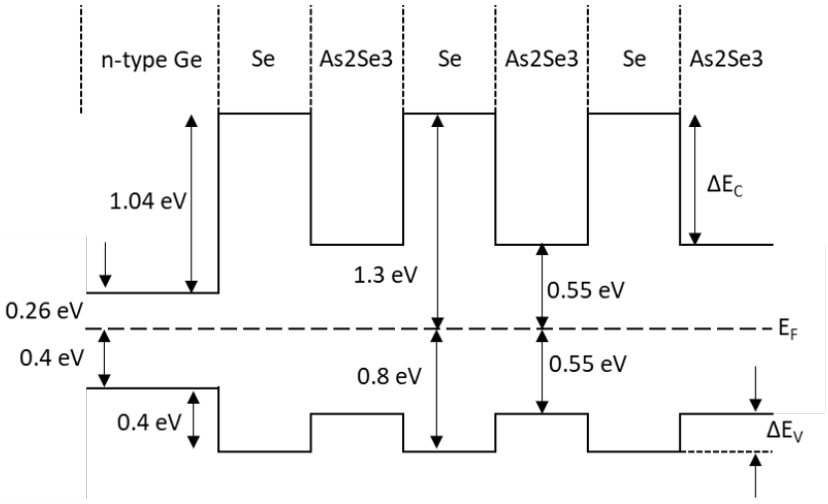

Figure 7.2: The band structure of the n-type Ge/superlattice Se structure under flat band conditions, showing a relatively high barrier for majority electrons such that the superlattice acts in effect as a blocking layer at room temperatures or lower.

cation gain from impact ionization at band discontinuities [17, 14]. We have shown that the multiplication factor, M, depends on the number of Se barriers, N, as $M = kN$ where k is a parameter depending on the uniformity of the field along the sample thickness, charge collection efficiency and other possible factors under further investigation. Based on this formula, for equal barrier and well widths of 8 nm, a 2 μm superlattice Se film should have $M = 125$ assuming a $k = 1$. We therefore fabricated 2 μm superlattice Se film onto n-type Ge substrate using classical rotational evaporation, and characterized the resulting samples using current-voltage (I-V) and current-time (I-T) measurements.

7.2 Materials and methods

7.2.1 Fabrication

The rotational evaporation technique was used to fabricate samples with multi-nanolayers of amorphous Se and As_2Se_3 as described in Chapter 2 [18]. We describe preparation and cleaning procedures for Ge substrates. The substrates were 8 mm square diced 500 μm thickness, n-type Ge (111) single-side polished wafers with a resistivity of 5-40 Ω·cm. The wafers were cleaned in an ultrasonic bath using acetone, methanol and deionized water, before being submerged alternately, for 15 s each time, in 9:1 diluted H_2O_2, then 9:1 diluted HF, repeating the cycle three times [19]. With the polished surface as the target of deposition, the cleaned substrates were then placed into the rotational evaporation system and the evaporation chamber was immediately pumped to high vacuum and then the deposition proceeded in the manner described in Chapter 2.

7.2.2 Characterization

The n-type Ge/superlattice Se samples were contacted using a Au whisker on the n-type Ge side with graphene contacting the superlattice Se. The devices were characterized

using current-voltage (I-V) measurement with voltages varying from 0 V to +100 V in 1 V steps on the HP4140B system. The I-V characteristics were measured with the devices under dark conditions and under irradiation with X-rays on the n-type Ge side. The X-ray source was a XM-10-60-05 10 W X-ray gun operated at 60 kV and 166 μA. For safety, the measurement setup was enclosed in a box with 1 mm thick steel walls. All measurements were in room temperature conditions.

The n-type Ge/superlattice Se devices were also measured for current-time (I-T) characteristics by streaming a sequence of chopped X-ray pulses onto the n-type Ge side. These characteristics were also measured at room temperature. The X-ray pulses were obtained by rotating a half-sectioned block in line with the X-ray line, as described in the schematic shown in Fig. 7.3. The rotation speed of the chopping block was 250 mHz providing pulses in 2 s intervals.

7.3 Results and Discussion

The results of I-V measurements are shown in Fig. 7.4. The results show a higher current when the sample is irradiated compared to current under dark conditions, indicating successful detection of X-rays. The magnitude difference in current between dark and X-ray irradiation gets smaller as the applied voltage increases. Beyond 90 V, the dark current and the photon induced current become indistinguishable such that photo detection is no longer possible.

Figure 7.5 shows results of I-T characterization. The results show current peaks that are synchronized to the input X-ray pulses, indicating successful detection of the X-ray pulses.

Transport in superlattice Se based device is described by a process of absorption and photo-generation in the n-type Ge and transport of photo-generated carriers towards the interface with the superlattice Se. At the interface, carriers are injected into the superlattice Se, followed by quantum tunneling through Se barriers and ballistic transport, and impact ionization at band discontinuities [20, 21, 14]. The injection

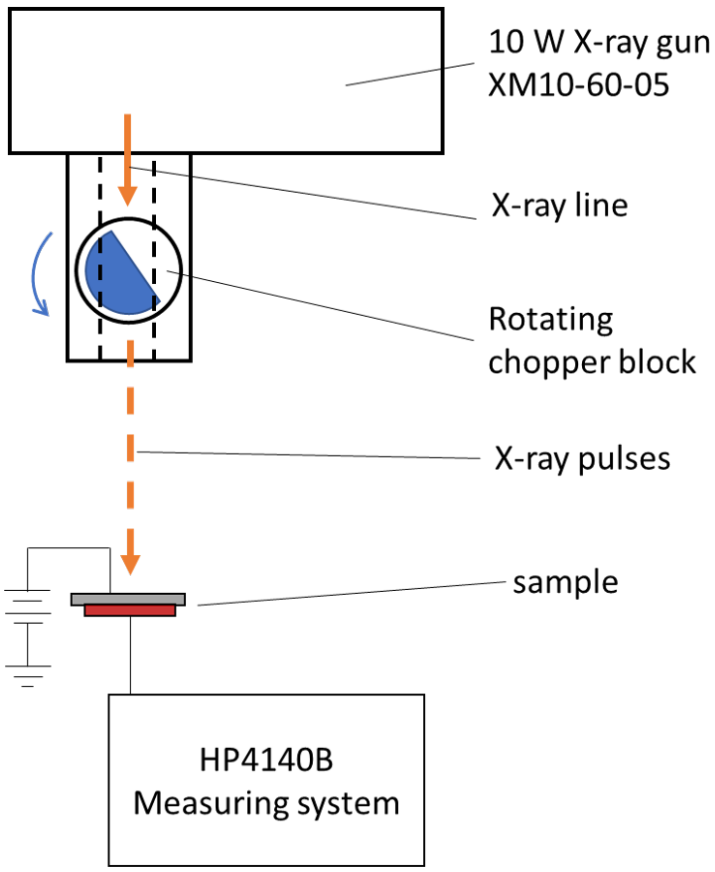

Figure 7.3: Schematic for the measurement of current-time (I-T) characteristics of n-type Ge/superlattice Se samples at room temperature. The sample under test is irradiated by a stream of X-ray pulses from an X-ray gun, through a rotating chopper block.

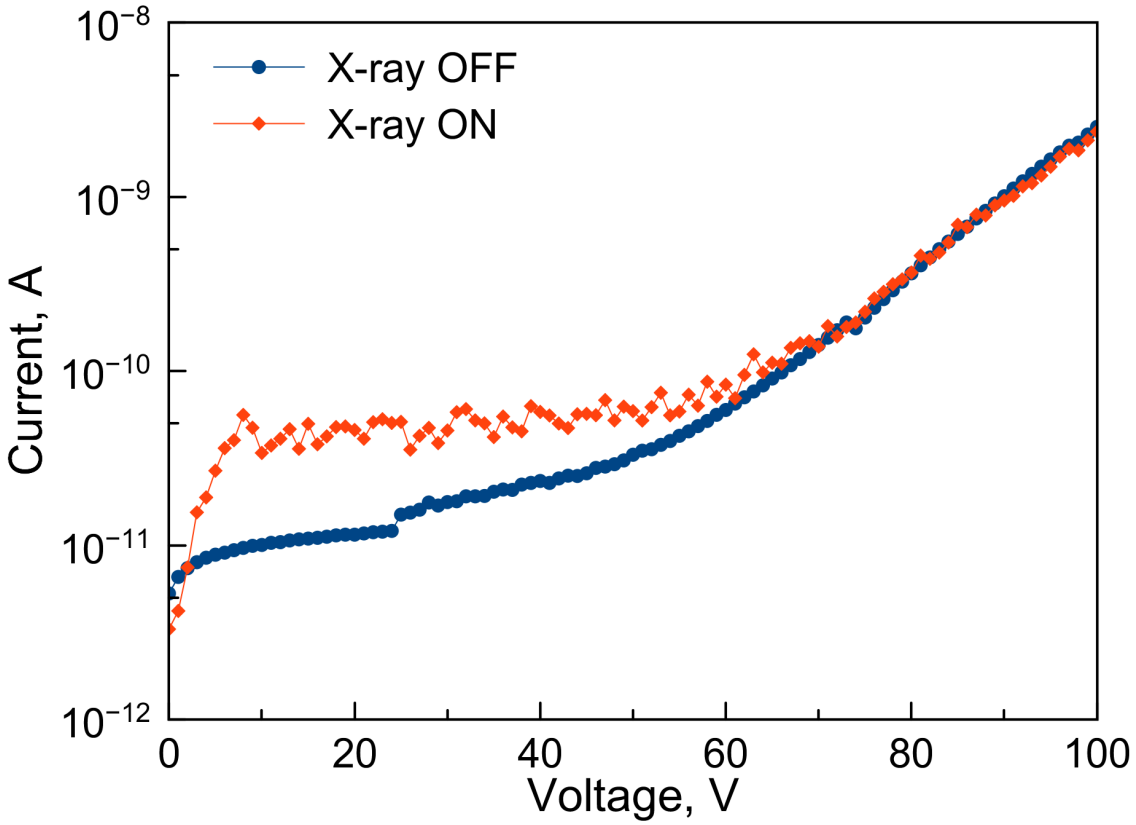

Figure 7.4: Current-voltage (I-V) characteristics measured for n-type Ge/superlattice Se samples under dark conditions and irradiated by X-rays.

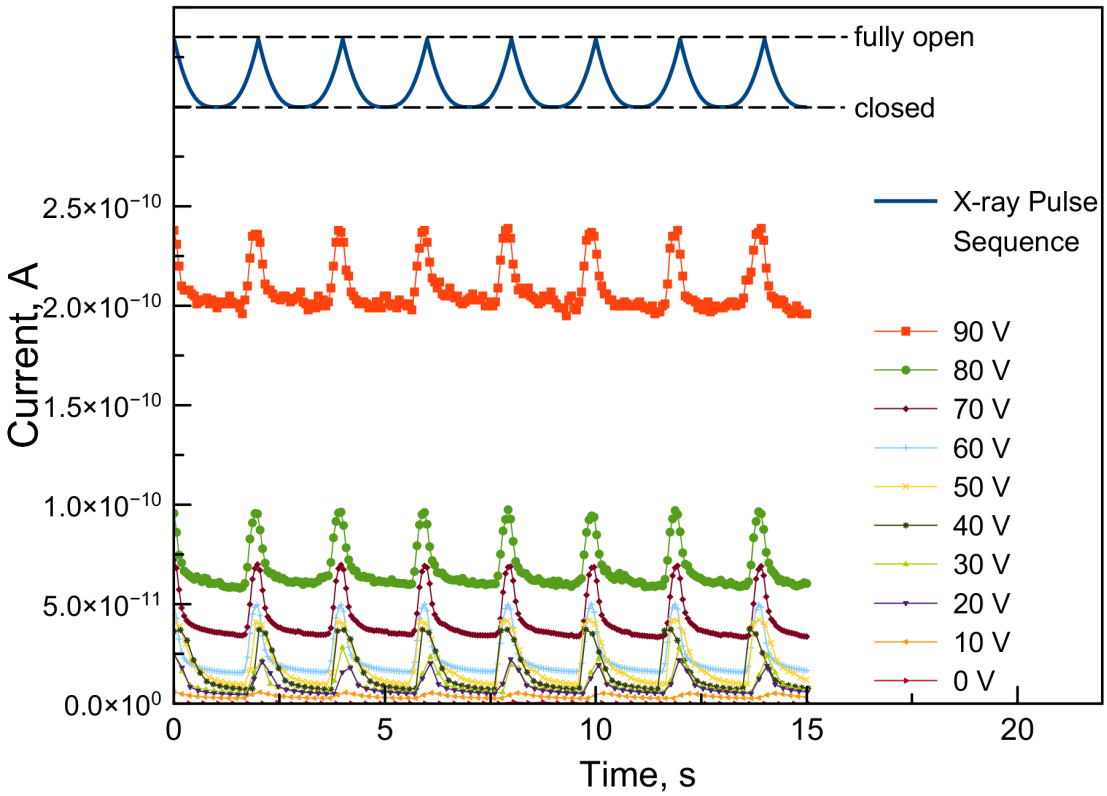

Figure 7.5: Typical current-time (I-T) characteristics of n-type Ge/superlattice Se samples irradiated by X-ray pulses. The characteristics are measured with the sample applied bias varied from +10 V to +90 V in 10 V steps. The current peaks are in sync with the X-ray pulse peaks indicating successful detection.

process affects the blocking and noise performance, and the transport process affects the multiplication gain.

A model of the n-type Ge/superlattice Se device is shown in Fig. 7.6. Incident photons into the Ge undergo photoelectric absorption and generate electron-hole pairs. The photo-generated carriers transport to the boundaries of the Ge by drift and diffusion. In this case, we are interested in the transport of photo-generated holes being transported towards the boundary n-type Ge and superlattice Se. Assuming monochromatic X-rays causing photo-generation at a single point at a depth x, a collection probability can be calculated indicating how likely a carrier generated at a depth x will be collected at the boundary of a material with a total thickness L. The collection efficiency for holes at this boundary due to drift can be calculated using the modified Hecht formula [22].

$$CP_{drift}(x) = \frac{\mu_{h,Ge}\tau_{h,Ge}F_{Ge}}{L}\left(1 - \frac{\left[\exp\left(-\frac{L}{\mu_{h,Ge}\tau_{h,Ge}F_{Ge}}\right) - \exp\left(-\frac{L}{\delta_{Ge}}\right)\right]}{\left[1 - \exp - \left(\frac{L}{\delta_{Ge}}\right)\right]\left[1 - \frac{\delta_{Ge}}{\mu_{h,Ge}\tau_{h,Ge}F_{Ge}}\right]}\right) \tag{7.1}$$

where $\tau_{h,Ge}$ and $\mu_{h,Ge}$ are the lifetime and the mobility for the minority holes, respectively [13]. The attenuation depth of 30 keV X-ray photons, $\delta_{Ge} = 71.7$ cm^{-1} [12]. The field distribution in Ge, F_{Ge} is estimated assuming the device as series connected resistances of Ge and the superlattice as shown in Fig. 7.6. Given the large differences between the resistivities ($\approx$ 1:10^7 Ge with respect to the superlattice Se), there is a very small field in the Ge compared to the superlattice. For an applied voltage of +100 V across the whole device, there is approximately only 10 μV dropped in the Ge. As such, the collection efficiency due to drift is very small, order of 0.5 %.

The collection probability for holes at the boundary due to diffusion (assuming a zero surface recombination velocity) can be calculated as [23]

$$CP(x) = \exp\left(-\frac{(L-x)}{L_{Diff}}\right) \tag{7.2}$$

where $L_{Diff} = \sqrt{D_{h,Ge}\tau_{h,Ge}}$ is the diffusion length, $D_{h,Ge}$ is the diffusivity of minority holes in Ge, and $\tau_{h,Si}$ is the lifetime for the minority holes. The diffusivity $D_{h,Ge}$ is calculated from the Einstein relation, and the lifetime $\tau_{h,Ge}$ =1 $\times 10^{-3}$ s [13].

At the boundary between n-type Ge and superlattice Se, carriers in the n-type Ge transit into the superlattice Se, either by thermal emission over the Se barrier, or by quantum tunneling across the barrier via internal field emission. A band structure of the n-type Ge/superlattice Se heterojunction is shown under flat band condition in Fig. 7.2.

Under dark conditions, majority electrons in the conduction band of n-type Ge face a barrier of 1.04 eV, meaning a low probability of thermal emission at 300 K. Due to the barrier height, the tunneling probability is also low even as the applied field increases. As the applied field is positive, it increases the barrier for electrons even further, significantly blocking them, and reducing the effect of thermal noise generated electrons.

Minority holes in the valence band of n-type Ge encounter a barrier of 0.4 eV. For the same applied field, this is a comparably smaller barrier, meaning holes are significantly injected into the superlattice Se by internal field emission.

When the n-type Ge side is irradiated, electron hole-pairs are generated. As in the case under dark conditions, the photo-carrier electrons are blocked, while photo-generated holes are injected into the superlattice Se. This has the effect of separating in space, the transport of holes from that of electrons [24].

In the periodic structure, a situation analogous to the n-type Ge/Se barrier obtains at each interface of the As_2Se_3 quantum well to Se barrier. Deep Level Transient Spectroscopy (DLTS) measurements have revealed occupied energy levels at $E_{C,Se}$ − 0.533 eV for electrons, and $E_{V,Se} - 0.269$ eV for holes. Therefore, electrons have a low probability of thermal emission and tunneling when a positive bias is applied. Holes have a comparatively lower barrier for both thermal emission and tunneling. Since the tunneling probability increases with applied field, it more likely that holes will transit

through the barrier by quantum tunneling through internal field emission.

After tunneling through the Se barrier, the injected carrier holes experience an abrupt change in force, becoming "hot", and for a short time transport without any collisions through quasi-ballistic transport [21]. During this transport, the energy distribution of the carriers is maintained. At the band discontinuity with As_2Se_3 the holes gain energy even further (the band discontinuity energy $\Delta E_V = 0.25$ eV). The probability of an impact ionization has the form $\exp(\frac{E_i}{k_B T})$ where E_i is the ionization threshold energy. The energy E_i depends on the location in energy where the impact ionization occurs, either shallow states near the band edges, deep states near the mid gap, and band to band ionization [25, 26]. As such, these holes have a higher probability to impact and ionize, most likely with shallow states and some deep states, and thus multiply the number of carriers.

The results were used to calculate the sensitivity S_x in terms of charge generated collected with respect to incident radiation measured in Kinetic Energy Released per Mass Attenuation in air (air KERMA). The air KERMA, K_{air}, was calculated as [27]

$$K_{air} = \int_0^{E_{max}} \Psi(E) \cdot \left(\frac{\mu_{tr}}{\rho}\right)_{E,air} dE \tag{7.3}$$

where $\Psi(E)$ is the differential distribution of photon energy fluence, and $\left(\frac{\mu_t r}{\rho}\right)_{E,air}$ is the mass energy-transfer coefficient as a function of photon energy E for air, obtained from the NIST database [12]. We used the SpekPy software program to calculate the energy fluence based on the X-ray tube parameters [28], the normalized spectrum is shown in Fig. 7.1 along with attenuation fractions for Ge and Si. The results of the sensitivity calculations are shown in Fig. 7.7. The charge collected was calculated from the I-T peaks as $Q = \int \Delta I \mathrm{d}t$ where ΔI is the X-ray signal current after subtracting the dark current. The sensitivity was then

$$S_x = \frac{Q}{K_{air}} \tag{7.4}$$

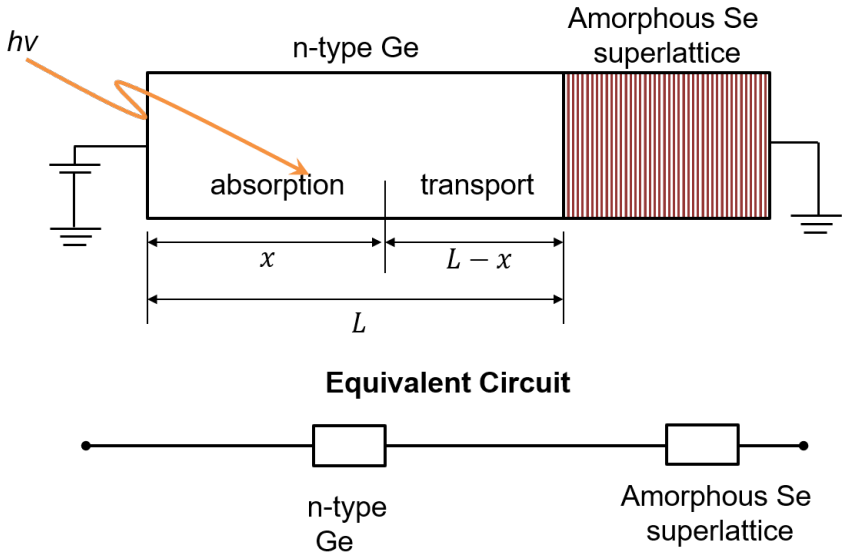

Figure 7.6: A model for the n-type Ge/superlattice Se device showing regions of absorption and transport of the photo-generated carriers. The device is taken as an equivalent circuit of two resistors connected in series.

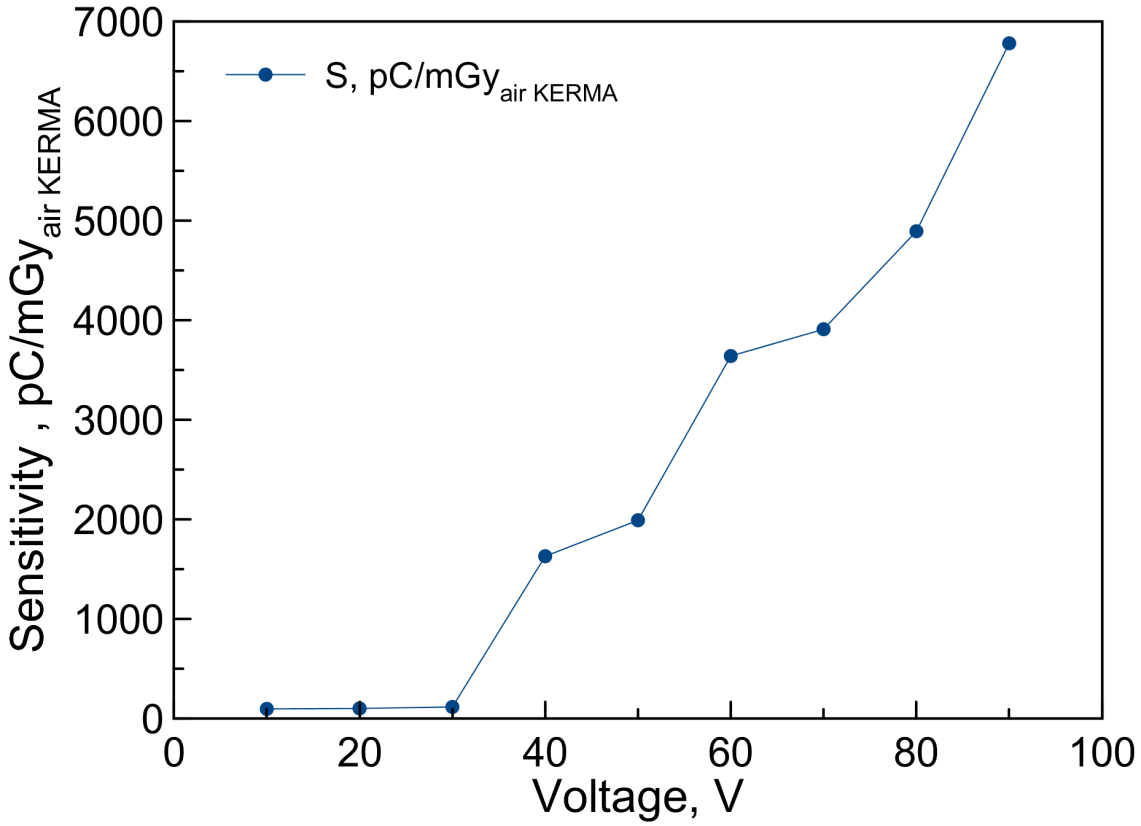

Figure 7.7: The sensitivity of the n-type Ge/superlattice Se X-ray detector for applied voltages from 10 V to 90 V.

The sensitivity S_x ranged from 96 pCmGy$^{-1}_{airKERMA}$ at 10 V to 6688 pCmGy$^{-1}_{airKERMA}$ at 90 V, comparable to values of about 250 pCmGy$^{-1}_{airKERMA}$ obtained in experiments with amorphous Se based detectors [29]. We speculate that this performance could be further improved by increasing the superlattice layer thickness, using n-type Ge with a higher dopant concentration, a Ge p-n junction, intrinsic Ge, or operating the device at even lower temperatures. We are also investigating applying the superlattice Se structure high Z absorbing materials such as CdTe and perovskites.

7.4 Conclusion

Using the quantum device design methods, we fabricated a detector for X-ray photons using n-type Ge/superlattice Se. The detector was characterized using I-V and I-T measurements, and the results showed successful detection of X-ray photons at room ambient. The characteristics were explained using a transport model that follows a sequence of injection, quantum tunneling, ballistic transport and impact ionization. The n-type Ge/superlattice Se devices showed sensitivity values of up to $\approx$ 6700 pCmGy$^{-1}_{airKERMA}$, comparable to state of the art devices. This demonstrates the possibility of augmenting the performance of conventional material by adding the superlattice Se structure. This additive nature of the structure means it may be possible to add it to high Z materials like CdTe, PbO, or perovskites like $MAPbI_3$. We hope this approach inspires the design and development of high performance devices using superlattices of amorphous materials.

References

[1] R. Yasin and W. Gouda, "Chest X-ray findings monitoring COVID-19 disease course and severity," *Egyptian Journal of Radiology and Nuclear Medicine*, vol. 51, no. 193, 2020.

[2] J. Cleverley, J. Piper, and M. M. Jones, "The role of chest radiography in confirming covid-19 pneumonia," *BMJ*, vol. 370, 2020.

[3] L. Rousan, E. Elobeid, M. Karrar, and Y. Khader, "Chest X-ray findings and temporal lung changes in patients with COVID-19 pneumonia," *BMC Pulmonary Medicine*, vol. 20, no. 245, 2020.

[4] G. Lutz, *Semiconductor Radiation Detectors*. Springer, Berlin, 1999.

[5] S. Kasap and M. Zangahir Kabir, "Photoconductors for X-ray Image Detectors," in *Handbook of Electronic and Photonic Materials*, pp. 1125–1147, Springer US, 2017.

[6] S. Kasap, J. Yang, B. Simonson, E. Adeagbo, M. Walornyj, G. Belev, M. P. Bradley, and R. E. Johanson, "Effects of X-ray irradiation on charge transport and charge collection efficiency in stabilized a-Se photoconductors," *Journal of Applied Physics*, vol. 127, no. 8, p. 084502, 2020.

[7] J. B. Frey, K. Sadasivam, G. Belev, H. Mani, L. Laperriere, and S. Kasap, "Dark current - voltage characteristics of vacuum deposited multilayer amorphous

selenium-alloy detectors and the effect of X-ray irradiation," *Journal of Vacuum Science & Technology A*, vol. 37, no. 6, p. 061501, 2019.

[8] J. A. Rowlands, "Material change for X-ray detectors," *Nature*, vol. 550, pp. 47–48, Oct 2017.

[9] Y. C. Kim, H. Kim, K, D. Son, D. Jeong, J. Seo, I. T. Choi, Y. S. Han, Y. S. Lee, and N. Park, "Printable organometalic perovskite large-area, low-dose X-ray imaging," *Nature*, vol. 550, pp. 87–91, October 2017.

[10] H. Tsai, F. Liu, S. Shrestha, K. Fernando, S. Tretiak, B. Scott, D. T. Vo, J. Strzalka, and W. Nie, "A sensitive and robust thin-film X-ray detector using 2D layered perovskite diodes," *Science Advances*, vol. 6, no. 15, 2020.

[11] O. Grynko, T. Thibault, E. Pineau, G. Juska, and A. Reznik, "Bilayer lead oxide X-ray photoconductor for lag-free operation," *Scientific Reports*, vol. 10, no. 20117, pp. 1 –9, 2020.

[12] M. J. Berger, J. H. Hubbell, S. M. Seltzer, J. Chang, J. S. Coursey, R. Sukumar, D. S. Zucker, and K. Olsen, "XCOM: Photon Cross Section Database (version 1.5)," *National Institute of Standards and Technology*, 2010.

[13] S. M. Sze, *Physics of semiconductor devices*. Wiley, New York, 1990.

[14] J. D. John, S. Okano, A. Sharma, O. Selyshchev, M. Rahaman, N. Miyachi, K. Enomoto, J. Ochiai, I. Saito, T. Masuzawa, T. Yamada, D. H. C. Chua, D. R. T. Zahn, and K. Okano, "Transport properties of Se/As_2Se_3 nanolayer superlattice fabricated using rotational evaporation," *Advanced Functional Materials*, vol. 29, no. 40, p. 1904758, 2019.

[15] R. L. Anderson, "Experiments on Ge-GaAs heterojunctions," *Solid-State Electronics*, vol. 5, pp. 341–351, 1962.

[16] N. F. Mott, "Electrons in non-crystalline materials: The last twenty five years," *Contemporary Physics*, vol. 26, pp. 203–215, Mar 1985.

[17] T. Masuzawa, S. Kuniyoshi, M. Onishi, R. Kato, I. Saito, T. Yamada, A. T. Koh, D. H. C. Chua, T. Shimosawa, and K. Okano, "Conditions for a carrier multiplication in amorphous-selenium based photodetector," *Applied Physics Letters*, vol. 102, no. 073506, pp. 1–4, 2013.

[18] I. Saito, W. Miyazaki, M. Onishi, Y. Kudo, T. Masuzawa, T. Yamada, A. Koh, D. Chua, K. Soga, M. Overend, M. Aono, G. A. J. Amaratunga, and K. Okano, "A transparent ultraviolet triggered amorphous selenium p-n junction," *Applied Physics Letters*, vol. 98, p. 152102, Apr 2011.

[19] K. Prabhakarana, T. Ogino, R. Hull, J. Bean, and L. Peticolas, "An efficient method for cleaning Ge(100) surface," *Surface Science*, vol. 316, no. 1, pp. L1031–L1033, 1994.

[20] K. Okano, S. Koizumi, S. Ravi, P. Silva, and G. A. J. Amaratunga, "Low-threshold cold cathodes made of nitrogen-doped chemical-vapor-deposited diiamond," *Nature*, vol. 381, pp. 140–141, May 1996.

[21] P. H. Cutler, N. M. Miskovsky, P. B. Lerner, and M. S. Chung, "The use of internal field emission to inject electronic charge carriers into the conduction band of diamond films: a review," *Applied Surface Science*, vol. 146, pp. 126–133, May 1999.

[22] S. Kasap, M. Z. Kabir, K. O. Ramaswami, R. E. Johanson, and R. J. Curry, "Charge collection efficiency in the presence of non-uniform carrier drift mobilities and lifetimes in photoconductive detectors," *Journal of Applied Physics*, vol. 128, no. 12, p. 124501, 2020.

[23] C. Donolato, "On the analysis of diffusion length measurements by SEM," *Solid-State Electronics*, vol. 25, no. 11, pp. 1077–1081, 1982.

[24] B. Abeles, "Amorphous semiconductor superlattices," *Superlattices and Microstructures*, vol. 5, pp. 473–480, Jul 1989.

[25] S. Kasap, J. Rowlands, S. D. Baranovskii, and K. Tanioka, "Lucky drift impact ionization in amorphous semiconductors," *Journal of Applied Physics*, vol. 96, pp. 2037–2047, Aug 2004.

[26] K. Tanaka, "Avalanche breakdown in amorphous selenium (a-Se) and related materials: Brief review, critique, and proposal," *Journal of Optoelectronics and Advanced Materials*, vol. 16, pp. 243–251, Apr 2014.

[27] F. H. Attix, *Introduction to Radiological Physics and Radiation Dosimetry.* WILEY-VCH Verlag, Weinheim, 2004.

[28] R. Bujila, A. Omar, and G. Poludniowski, "A validation of SpekPy: A software toolkit for modelling X-ray tube spectra," *Physica Medica*, vol. 75, pp. 44–54, 2020.

[29] S. Kasap, J. B. Frey, G. Belev, O. Tousignant, H. Mani, J. Greenspan, L. Laperriere, O. Bubon, A. Reznik, G. DeCrescenzo, K. S. Karim, and J. A. Rowlands, "Amorphous and polycrystalline photoconductors for direct conversion flat panel X-ray image sensors," *Sensors*, vol. 11, pp. 5112–5157, May 2011.

Chapter 8

Conclusion

We investigated the optical and electronic properties of amorphous Se superlattices fabricated using rotational evaporation. Samples measured using TOF-SIMS confirmed the multi-layer structure, with each layer measured to be 6-9 nm thick. Such thicknesses are within sizes of quantum structures. Using DLTS, energy levels were measured at $E_{C,Se}-0.533$ eV and $E_{V,Se}+0.269$ eV. These levels were attributed to minibands formed due to the superlattice structure. Spectroscopic ellipsometry measurements showed a series of "steps" in the absorption coefficient at 1.72 eV, 1.82 eV, 1.89 eV, 1.97 eV and 2.04 eV. This staircase structure in the absorption coefficient is associated with transitions in two dimensional quantum structures. Electronic transport properties were characterized using I-V measurements, revealing oscillations and regions of negative dynamic resistance. These features were explained by a model involving injection, sequential quantum tunneling and impact ionization. The model also showed a relationship between the multiplication factor, M, and the number of superlattice barrier layers, N, $M = kN$. This relationship was the basis of a design method for optimally engineered photo-detectors. The design method was demonstrated by fabricating a detector for 100 μW 525 nm light, using n-type Si and superlattice Se with expected multiplication gains of 12 (200 nm superlattice Se) and 125 (2 μm superlattice Se). The results showed gains of 11 and 48 at applied field of 5×10^7 Vm^{-1}, confirming $M = kN$.

Further investigation is needed to provide more understanding of the field distribution in the superlattice structure. At a material level, there is need to understand the atomic distribution in the multi-layer structure, particularly at transition interfaces. Characterization using methods such as Electron Diffraction spectroscopy (EDS), Dynamic SIMS or Rutherford Backscattering spectroscopy (RBS) may reveal material distribution from layer to layer.

When an external field is applied, the distribution of the field and the active zones of the superlattice can be investigated using methods such as Cathodoluminescence spectroscopy or Electron Beam Induced Current (EBIC). It is expected that the quan-

tized energy levels of the superlattice will broaden due to Wannier-Stark effects, so spectroscopic ellipsometry with samples under bias may also reveal active areas of the superlattice.

There is also interest in the fabrication and characterization of these technologically simple superlattices based on amorphous materials. Besides the combination of Se and As_2Se_3, there are several other possibilities, each offering unique and interesting properties. The immediate likely combination is the inclusion of Te in combination with either As_2Se_3 or Se, or in a tri-layer structure of the three materials. The rotational evaporation chamber already houses a third evaporation drum dedicated for Te. A superlattice including Te is interesting given the narrow band gap of the material of about 0.4 eV. Another possible superlattice includes Se with a high-Z material. Such material has to have the three properties of a smaller band gap than Se, be a Se based compound and have relatively low boiling point so that it can be used in rotational evaporation. Thallium(I)Se is one likely candidate, with a band gap of 1.2 eV, and boiling point of 1746 K.

We demonstrated X-ray detection under room temperature conditions using n-type Ge with amorphous Se superlattice. However, performance is expected to improve further by using high purity Ge (HPGe) and operating at liquid nitrogen (LN_2) temperatures. It is therefore necessary to investigate the transport characteristics of the superlattice Se under low temperatures. Variations of carrier mobility with temperature can be investigated using temperature based Hall effect measurements or Time of Flight measurements.

The additive nature of the superlattice, especially to conventional materials means that it can be used to improve the performance of conventional photo-detector structures if it can be co-opted into the device geometry. For example, the superlattice structure can be evaporated as an additional layer onto a strip detector before producing the readout structures. In this way, photo-generated charge can be multiplied by a custom gain before being readout, significantly improving the SNR of a basic strip

detector. A similar strategy may be adopted for other photo-detector device geometries such as p-n and p-i-n photodiodes.

Based on the models discussed, it is possible to innovate devices with novel features. It may be possible to add a third contact along the transport axis of the superlattice, which controls the field distribution. This may allow field variation of the multiplication factor, allowing for features like automatic exposure control and dynamic range control in photo-detectors. From the same concept, a field multiplication transistor is possible. Such a device would have a high input impedance since only a small amount of carriers need to be injected, which are then multiplied to a larger signal.

Amorphous Se superlattice is made from phase-changeable chalcogenide materials. As such it may be possible to develop mixed phase crystalline amorphous superlattices (CASL) and phase switching superlattice structures. The associated electronic, optical and quantum features of the superlattices should vary between phases, providing an additional degree of features. Such features may prove vital in the development of technologies such as phase change memories (PCM) and non-von Neuman in-memory computing.

We anticipate that ultra-sensitive detectors based on design concepts discussed herein will make already existing imaging systems safer by allowing operation under very low X-ray exposure. This means that X-ray imaging can be safely used during pregnancy, on infants and children without severe concerns associated with current systems. Additionally, such a system will open opportunity for innovation in X-ray imaging. One such possibility is real-time X-ray imaging which could be useful during surgeries such as device implantations. Real-time X-ray could also provide information on the stresses and strains associated with the movement of the skeleton and organs, helping health practitioners to optimize healing processes after injury or surgery. Another possible innovation from this detector is automatic exposure (AE) control. X-ray image quality could be made consistent regardless of X-ray source quality, target body size or operator skill. Overall, this type of detector promises significant evolution in

X-ray imaging.

Appendix A

Superlattice theory

In 1970 Esaki and Tsu proposed a periodic structure in one dimension, made from ultra-thin layers of different semiconductor materials in terms of band gap, and named it a "superlattice" [1, 2, 3]. The ultra-thin layers are expected to have a period of less than the mean free path of an electron such that de Broglie electron waves would result in resonant tunneling through the barriers of the superlattice. Such characteristics meant that the superlattice would exhibit unusual features, different from its source materials. Due to the sizes of the layers, quantum effects were expected, such as quantized energy levels and two-dimensional density of states, and negative differential conductivity.

Practically it was difficult to fabricate good quality superlattices, until the introduction of Molecular Beam Epitaxy (MBE) as a fabrication process for the superlattices [3]. MBE allowed fabrication of good interfaces and as such, some of the predicted superlattice characteristics could be observed. A plethora of applications of these superlattices have been proposed including high speed transistors, quantum cascade lasers, and low noise avalanche photodiodes, among many others. [4, 1, 5, 6, 7]. These devices, though fabricated and successfully demonstrated have not been put to widespread use due to the high technology barrier for fabrication, and the requirement for high quality crystalline materials for good quality interfaces. These challenges prompted examination into superlattices of amorphous materials, particularly amorphous Si [8, 9, 10]. There were some works investigating superlattices of amorphous chalcogenide materials [11, 12, 13]. Much of the work focused on structural properties and make significant progress even though there were challenges in characterizing the details of these less predictable superlattices. Recently, there is renewed interest in superlattices of amorphous chalcogenides particularly for applications in phase change memories [14, 15, 16]

A.1 Superlattice theory

A superlattice has a periodic energy structure and thus can be analyzed following the Kronig-Penney model.

A.1.1 The Kronig-Penney model

In 1931 a paper by R. de L. Kronig and W. G. Penney was published in the Proceedings of the Royal Society, describing the behavior of electrons in a periodic potential [17, 18]. Following the work of Bloch, Kronig and Penney specifically aimed at the mechanics of electrons in periodic fields found in practice, meaning in crystalline materials. Furthermore, they wanted to provide computable values of energy and eigenfunctions of the wave-equations of such electrons. Their analysis is relevant to artificial periodic structures such as quantum wells. We review and summarize the model and apply it to evaluate amorphous Se superlattices.

Energy Values

To obtain the energy levels E, Kronig and Penney considered a one-dimensional periodic potential shown in Fig. A.1

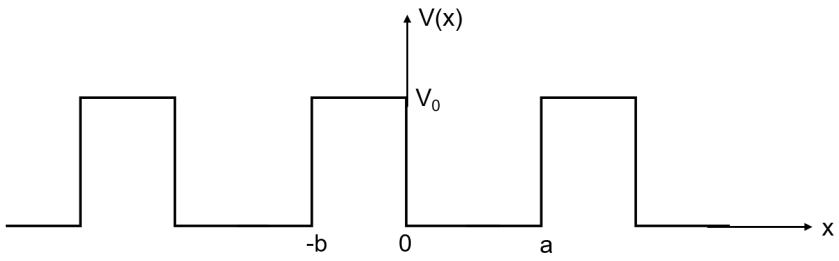

Figure A.1: The periodic potential considered in the Kronig-Penney model. The potential $V(x)$ is 0 in the regions $0 < x \leq a$, and takes the value V_0 for the regions $-b < x \leq 0$. The period for this potential is $L = G(a + b)$ where $G \in \mathbb{Z}$.

The Schrodinger equation can be analyzed for this potential

$$\frac{d^2\psi}{dx^2} + \kappa^2[E - V(x)]\psi = 0 \tag{A.1}$$

where $\kappa = \frac{\sqrt{2m}}{\hbar}$, m is the electron mass, and $\hbar$ is the reduced Planck's constant. Following Bloch's theorem, any wave function for a periodic potential with a period L

will have the form [18]

$$\psi(x) = u(x)\mathrm{e}^{i\alpha x} \tag{A.2}$$

where $u(x)$ with period L in x, $\alpha = \frac{2\pi k}{L}$ and $k \in \mathbb{Z}$. This conditions allows the consideration of the solutions of $u(x)$ in one period, for example $-b < x < a$ shown in Fig. A.1. Making the assumption $0 < E < V_0$ and substituting equation A.2 into equation A.1 gives

$$\begin{cases} \frac{d^2u}{dx^2} + 2i\alpha\frac{du}{dx} - (\alpha^2 + \gamma^2)u = 0 \quad -b \leq x \leq 0 \\ \frac{d^2u}{dx^2} + 2i\alpha\frac{du}{dx} - (\alpha^2 + \beta^2)u = 0 \quad 0 \leq x \leq a \end{cases} \tag{A.3}$$

where $\gamma = \kappa\sqrt{V_0 - E}$ and $\beta = \kappa\sqrt{E}$, both being real values. These equations have solutions

$$u = \begin{cases} A\mathrm{e}^{(-i\alpha+\gamma)x} + B\mathrm{e}^{(-i\alpha-\gamma)x} \\ C\mathrm{e}^{i(-\alpha+\beta)x} + D\mathrm{e}^{i(-\alpha-\beta)x} \end{cases} \tag{A.4}$$

The integration constants A, B, C, D can be found from boundary conditions. The first two conditions are that the wave function ψ is the same across a discontinuity of the periodic potential (at $x = 0$), and similarly the first derivative of ψ. The second pair of conditions is from Bloch's theorem, that u is periodic, and so is its first derivative. The four conditions yield four linear equations

$$A + B = C + D, \tag{A.5}$$

$$(-i\alpha + \gamma)A + (-i\alpha - \gamma)B = i(-\alpha + \beta)C + i(-\alpha - \beta)D, \tag{A.6}$$

$$A\mathrm{e}^{(i\alpha-\gamma)b} + B\mathrm{e}^{(i\alpha+\gamma)b} = C\mathrm{e}^{i(-\alpha+\beta)a} + D\mathrm{e}^{i(-\alpha-\beta)a} \tag{A.7}$$

$$(-i\alpha + \gamma)A\mathrm{e}^{(i\alpha-\gamma)b} + (-i\alpha - \gamma)B\mathrm{e}^{(i\alpha+\gamma)b} = i(-\alpha + \beta)C\mathrm{e}^{i(-\alpha+\beta)a} + i(-\alpha - \beta)D\mathrm{e}^{i(-\alpha-\beta)a} \tag{A.8}$$

The nontrivial solution to these equations can be obtained from equating the determi-

nant of the coefficients to zero

$$\begin{vmatrix} 1 & 1 & 1 & 1 \\ (-i\alpha+\gamma) & (-i\alpha-\gamma) & i(-\alpha+\beta) & i(-\alpha-\beta) \\ \mathrm{e}^{(i\alpha-\gamma)b} & \mathrm{e}^{(i\alpha+\gamma)b} & \mathrm{e}^{i(-\alpha+\beta)a} & \mathrm{e}^{i(-\alpha-\beta)a} \\ (-i\alpha+\gamma)\mathrm{e}^{(i\alpha-\gamma)b} & (-i\alpha-\gamma)\mathrm{e}^{(i\alpha+\gamma)b} & i(-\alpha+\beta)\mathrm{e}^{i(-\alpha+\beta)a} & i(-\alpha-\beta)\mathrm{e}^{i(-\alpha-\beta)a} \end{vmatrix} = 0 \tag{A.9}$$

which gives an equivalent expression

$$\frac{\gamma^2-\beta^2}{2\beta\gamma}\sinh\gamma b\sin\beta a+\cosh\gamma b\cos\beta a=\cos\alpha(a+b) \tag{A.10}$$

Later, Esaki and Chang quoted this equation in the form [3]

$$-1\leq\cos\frac{a\sqrt{2mE}}{\hbar}\cosh\frac{a\sqrt{2m(V-E)}}{\hbar}+\left(\frac{V}{2E}-1\right)\left(\frac{V}{E}-1\right)^{\frac{1}{2}} \sin\frac{a\sqrt{2mE}}{\hbar}\sinh\frac{a\sqrt{2m(V-E)}}{\hbar}\leq 1 \tag{A.11}$$

from which the energy states E_n (n becomes a quantum number) in the potential wells in the x-direction could be obtained. We used this equation to calculate the energy levels in the amorphous Se superlattice. Amorphous chalcogenide materials are known to have different electrical and optical band gaps [19, 20], and given this fact, we calculated the energy structures separately based on electrical and optical band gaps. To determine the periodic potential, the Anderson Rule was used [21]. For the electrical case, the amorphous Se mobility gap is 2.05 eV [20], and the Fermi level determined from Ultraviolet Photoelectron Spectroscopy (UPS) is about $\mathrm{E}_{V,Se}$ + 0.8 eV within ±0.1 eV, in close agreement to values reported in literature [22]. The electrical band gap of As_2Se_3 is 1.1 eV, with the Fermi level taken to be at the mid-gap [19, 23, 24, 25]. For the optical case, the band gap for Se and As_2Se_3 were 2.0 eV and 1.7 eV respectively, with the Fermi level set to be at E_V + 0.8 eV for Se and at the mid gap for As_2Se_3. In both electrical and optical case, the effective masses in the quantum

well material As_2Se_3 were set as 0.27 and 0.28 for electrons and holes respectively [26]. The energy levels were calculated over a range of quantum well thicknesses from 4 nm to 10 nm. The results of the calculations are shown in Fig. A.2. The calculation was done using the SageMath mathematical software system, and the notebook is available on GitHub at https://github.com/JoshDumo/SuperlatticeEnergyLevels.

Equation A.10 can be made more convenient by considering the barrier region $(-b \leq x \leq 0)$ as delta functions. This is the limiting case

$$\lim_{b\to 0,\gamma\to+\infty} \frac{\gamma^2 ab}{2} = P \tag{A.12}$$

at which Equation A.10 reduces to a transcendental equation of βa

$$P\frac{\sin\beta a}{\beta a} + \cos\beta a = \cos\alpha a \tag{A.13}$$

This is the commonly quoted equation of the Kroning-Penney model which is particularly used in calculating energy versus crystal momentum $(E - k)$ diagrams for crystalline materials [18].

Wave-functions

Continuing with the limiting case $b \to 0$, only the lower part of equation A.4

$$u = C\mathrm{e}^{i(-\alpha+\beta)x} + D\mathrm{e}^{i(-\alpha-\beta)x} \tag{A.14}$$

is of concern. In this case

$$D = -C\frac{1 - \mathrm{e}^{-i(\alpha-\beta)a}}{1 - \mathrm{e}^{-i(\alpha+\beta)a}} \tag{A.15}$$

Accordingly, the wave-equation for a generalized case between a region ra to $(r+1)a$ then becomes

$$\psi = C\mathrm{e}^{i\beta x + ir(\alpha-\beta)a} + D\mathrm{e}^{-i\beta x + ir(\alpha+\beta)a} \tag{A.16}$$

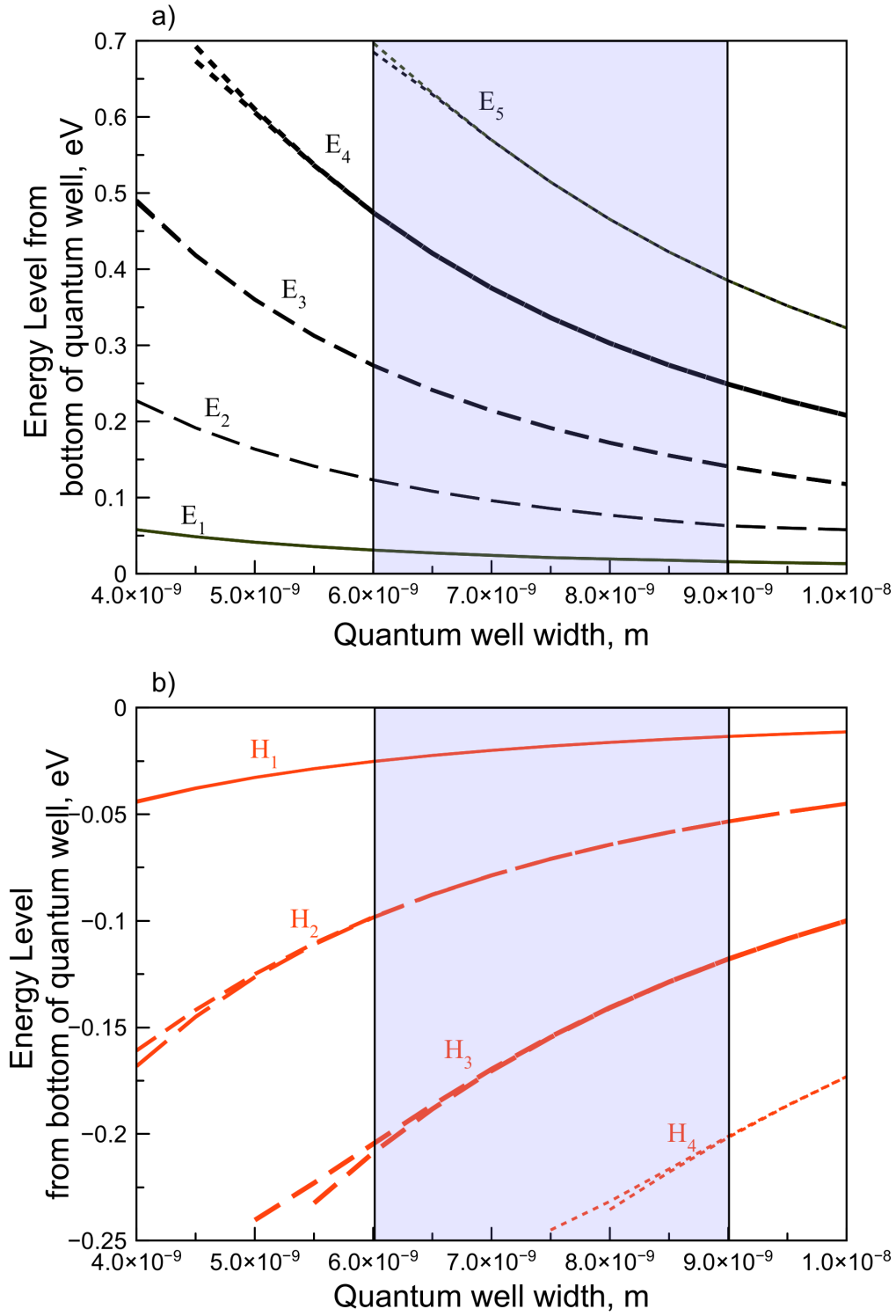
a)
Energy Level from bottom of quantum well, eV
0.7
0.6
0.5
0.4
0.3
0.2
0.1
0
E5
E4
E3
E2
E1
4.0×10−9
5.0×10−9
6.0×10−9
7.0×10−9
8.0×10−9
9.0×10−9
1.0×10−8
Quantum well width, m
b)
Energy Level from bottom of quantum well, eV
0
−0.05
−0.1
−0.15
−0.2
−0.25
H1
H2
H3
H4
4.0×10−9
5.0×10−9
6.0×10−9
7.0×10−9
8.0×10−9
9.0×10−9
1.0×10−8
Quantum well width, m

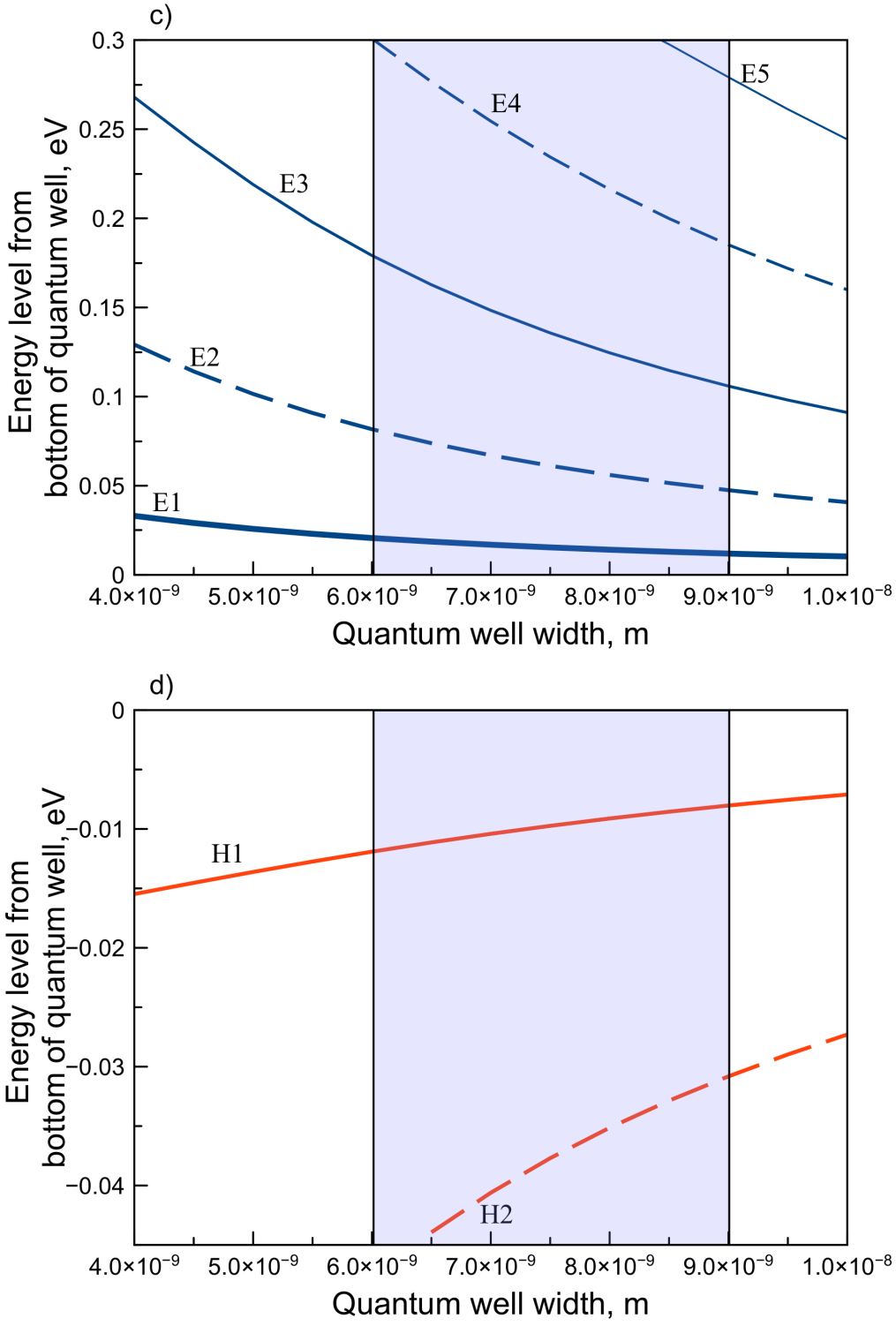

Figure A.2: Calculated energy levels for the amorphous Se superlattice structure based on the Kronig-Penney model. (a) and (b) are conduction band and valence band quantum well energy levels, respectively, based on electrical band gaps. (c) and (d) are conduction band and valence band quantum well energy levels, respectively, based on optical band gaps.

As $P \to \infty$

This case basically refers to an infinite potential for the barriers. In this case $\beta = n\pi$ where $n \in \mathbb{Z}$ and $D = -C$ so that equation A.16 becomes

$$\psi = C\mathrm{e}^{in\pi x + ir(\alpha - n\pi)a} + C\mathrm{e}^{in\pi x + ir(\alpha + n\pi)a} \tag{A.17}$$

$$= C\mathrm{e}^{ir\alpha a}(\mathrm{e}^{in\pi x} - \mathrm{e}^{-in\pi x}) \tag{A.18}$$

$$= 2iC\mathrm{e}^{2ir\alpha a} \sin n\pi x \tag{A.19}$$

This is a solution commonly referred to as the "particle in a constant potential box" in which the wave-functions of electrons are confined between an infinite impenetrable potential barriers separated by distance a [18].

As $P \to 0$

This case then refers to conditions in which the potential of the barrier has some finite value. Equation A.13 shows that for a valid value of βa there is a value αa that satisfies the equation, along with its cycles $\alpha a \mp 2n\pi$. However, the cycles of αa do not produce any new solutions, rather repeating the same solutions obtained for βa and αa. Thus there is a one-to-one relationship between βa and αa, and conventionally we can equate them and thus distinguish energy states based only on α.

In the case $P \to 0$, since $\beta a = \alpha a$, $D = 0$ except for $\alpha a = n\pi$. Starting with the $D = 0$ case, the wave-function becomes

$$\psi = C\mathrm{e}^{i\beta x + ir(\alpha - \beta)a} \tag{A.20}$$

$$= C\mathrm{e}^{i\alpha x + ir(\alpha - \alpha)a} \tag{A.21}$$

$$= C\mathrm{e}^{i\alpha x} \tag{A.22}$$

The wave function is seen to have an exponential decay even into the potential barrier. This means that there is a probability of the electrons penetrating into the barrier and even appearing in the adjacent potential well even though they have energy W which

is less than V_0 the barrier potential.

For the exception $\alpha a = n\pi$, $D \mp C$ such that the wave-function is expressed as

$$\psi = C\mathrm{e}^{i\beta x + ir(\alpha-\beta)a} \mp C\mathrm{e}^{-i\beta x + ir(\alpha+\beta)a} \tag{A.23}$$

$$= C\mathrm{e}^{i\alpha x + ir(\alpha-\alpha)a} \mp C\mathrm{e}^{-i\alpha x + ir(\alpha+\alpha)a} \tag{A.24}$$

$$= C[\mathrm{e}^{i\alpha x} \mp \mathrm{e}^{-i\alpha x + 2ir\alpha a}] \tag{A.25}$$

$$= C[\mathrm{e}^{i\alpha x} \mp \mathrm{e}^{-i\alpha x + 2irn\pi}] \tag{A.26}$$

$$= C[\mathrm{e}^{i\alpha x} \mp \mathrm{e}^{-i\alpha x}] \tag{A.27}$$

so that in general

$$\psi = \begin{cases} C\cos\alpha x: & n \text{ is odd} \\ C\sin\alpha x: & n \text{ is even} \end{cases} \tag{A.28}$$

From the analysis, Kroning and Penney concluded that the energy and wave-functions could be computed particularly for the practical case where of a finite periodic potential. Their analysis also concluded that electrons could transport through the lattice (x-direction) since there was a probability of finding the electron in the potential barrier and even penetrating to adjacent potential wells. Kronig and Penney also concluded that it was possible for the electron to transition in energy to other stationary states if there is emission or absorption of energy.

Optical Transitions in Superlattices

Radiative transitions in the periodic potential occur between stationary states that consist of a confined wave-function in the x-direction and a free plane wave in the yz direction [27]. To derive an expression for the transition rate, The Fermi Golden rule is applied [28]. It states that for optical transitions from the initial state $|i\rangle$ at energy E_i to the final state $|f\rangle$ at energy E_f, the probability is

$$T(i \to f) = \frac{2\pi}{\hbar} \left|\langle f| \, e\mathbf{r}\cdot\mathbf{E} \, |i\rangle\right|^2 \rho(\hbar\omega) \tag{A.29}$$

where $\rho(\hbar\omega)$ is the joint density of states at photon energy $\hbar\omega$, $\mathbf{E}$ is the electric field of the optical wave $e\mathbf{r}$ is the electronic dipole. Transitions will occur in accord with the Law of Conservation of Energy. This means that to transition to a higher final state energy is absorbed from a photon ($E_f = E_i + \hbar\omega$), whereas a transition to a lower final state energy is emitted as a photon ($E_f = E_i - \hbar\omega$).

Considering a transition from a confined hole state with in the valence band with energy $E_{\mathrm{h}n}$, to a confined electron state in the conduction band at energy $E_{en'}$, where n and n' are quantum numbers, and using Bloch's theorem, the wave-functions become

$$|i\rangle = u_v(\mathbf{r})\mathrm{e}^{i\mathbf{k}_{yz(v)}\cdot r_{yz}}\psi_{\mathrm{h}n}(x), \tag{A.30}$$

$$|f\rangle = u_c(\mathbf{r})\mathrm{e}^{i\mathbf{k}_{yz(c)}\cdot r_{yz}}\psi_{en'}(x) \tag{A.31}$$

where $u_c(\mathbf{r})$ and $u_v(\mathbf{r})$ represent conduction and valence band envelop functions respectively. The respective in-plane wave function k-vectors are given as $\mathbf{k}_{yz(c)}$ and $\mathbf{k}_{yz(v)}$, with r_{yz} as the position vector. Finally, $\psi_{\mathrm{h}n}(x)$ and $\psi_{en'}(x)$ are the wavefunctions of the confined electron and hole in the x-direction.

The wave-functions are substituted into equation A.29. Since the wave vector for the photon is small, the Law of Conservation of Momentum requires that the wave vectors of the electron and hole be the same

$$\mathbf{k}_{yz(c)} = \mathbf{k}_{yz(v)}. \tag{A.32}$$

This is k-selection and implies that transitions are only possible between states that have the same in-plane k-vectors. Only under this condition does the overlap integral involving these k-vectors have a value of unity, being zero everywhere else.

The transition can then be shown to be proportional to the joint density of states $\rho(\hbar\omega)$ and the overlap integral of the wave-functions squared.

$$T \propto \left|\langle\psi_{en'}(x)|\psi_{\mathrm{h}n}(x)\rangle\right|^2 \rho(\hbar\omega) \tag{A.33}$$

The density of states for two-dimensional structures is independent of energy [29, 30]. Instead it exhibits a staircase structure with each step associated with an energy state E_n. Referring to equation A.28 it can be seen that the overlap integral for the wave functions is zero when $n \neq n'$. The wave functions in this case are orthogonal such that the overlap integral vanishes. Only when $n = n'$ (or $\Delta n = n - n' = 0$) is the integral valid, and this becomes selection rule commonly referred to as the $\Delta n = 0$ selection rule. In general, transitions will only occur for energy states with the same quantum number index. It is noted that this rule applies only to envelop functions that are symmetrical about the center of the well, therefore does not apply for potential wells under an external bias, or for triangular shaped potential wells.

Thus, for an absorptive transition to occur, a photon must have a threshold energy

$$\hbar\omega = E_g + E_{\mathrm{hn}} + E_{en} \tag{A.34}$$

where, E_g is the energy gap of the potential well material. The threshold energy is minimum at $n = 1$.

Since the optical absorption coefficient $\alpha(\hbar\omega)$ is proportional to the transition probability [31, 32, 33], its characteristics for the periodic potential can be inferred following the discussion above:

- The absorption coefficient has a series of steps where it is constant, giving it a staircase shape,
- The stairs "climb" at threshold energies given by $\hbar\omega = E_g + E_{\mathrm{hn}} + E_{en}$, with the first step at $n = 1$

This can be compared to the absorption coefficient of a three-dimensional bulk material in which [31, 33]

$$\alpha(\hbar\omega) = (\hbar\omega - E_g)^{\frac{1}{2}}. \tag{A.35}$$

In this case the absorption coefficient has a parabolic dependence on energy with a

single threshold at E_g Thus a two-dimensional structure changes the absorption characteristics of the bulk material by shifting minimum the threshold energy to a higher value $E_g + E_{\mathrm{h1}} + E_{\mathrm{e1}}$ and giving it a staircase shape due to additional quantized energy states and a joint density of states that is independent of energy.

References

[1] L. Esaki, "Advances in semiconductor superlattices, quantum wells and heterostructures," *Journal de Physique Colloques*, vol. 45, pp. C5–3–C5–21, Apr 1984.

[2] L. Esaki and R. Tsu, "Superlattice and negative differential conductivity in semiconductors," *IBM Journal of Research and Development*, vol. 14, pp. 61–65, Jan 1970.

[3] L. Esaki and L. L. Chang, "New transport phenomenon in a semiconductor "superlattice"," *Physical Review Letters*, vol. 33, pp. 496–498, Aug 1974.

[4] F. Capasso, W. T. Tsang, A. L. Hutchinson, and G. F. Williams, "Enhancement of electron impact ionization in a superlattice: A new avalanche photodiode with a large ionization rate ratio," *Applied Physics Letters*, vol. 40, no. 1, pp. 38–40, 1982.

[5] F. Capasso, J. Allam, A. Y. Cho, K. Mohammed, R. J. Malik, A. L. Hutchinson, and D. Sivco, "New avalanche multiplication phenomenon in quantum well superlattices: Evidence of impact ionization across the band ‐ edge discontinuity," *Applied Physics Letters*, vol. 48, no. 19, pp. 1294–1296, 1986.

[6] F. Capasso, "Band-gap engineering: From physics and materials to new semiconductor devices," *Science*, vol. 235, no. 4785, pp. 172–176, 1987.

[7] K. Sawada, M. Akiyama, and M. Ishida, "Excess noise characteristics of amorphous silicon staircase photodiode films," *Applied Physics Letters*, vol. 75, pp. 1470–1472, Jul 1999.

[8] B. Abeles and T. Tiedje, "Amorphous semiconductor superlattices," *Physical Review Letters*, vol. 51, pp. 2003–2006, Nov 1983.

[9] B. Abeles, "Amorphous semiconductor superlattices," *Superlattices and Microstructures*, vol. 5, pp. 473–480, Jul 1989.

[10] S. Miyazaki, "Amorphous semiconductor superlattices (in Japanese)," *New Glass*, vol. 5, no. 1, pp. 45–56, 1990.

[11] R. Ionov, "Interface-induced structural changes in amorphous chalcogenide superlattices," *Thin Solid Films*, vol. 221, no. 1, pp. 39–43, 1992.

[12] R. I. Ionov, "Structural properties of amorphous chalcogenide SeTe/CdSe superlattices," *Journal of Non-Crystalline Solids*, vol. 159, no. 3, pp. 222–228, 1993.

[13] E. Vateva and D. Nesheva, "Small-angle X-ray diffraction studies on interface sharpness of amorphous Se/CdSe superlattices," *Journal of Non-Crystalline Solids*, vol. 191, no. 1, pp. 205–208, 1995.

[14] T. C. Chong, L. P. Shi, X. Q. Wei, R. Zhao, H. K. Lee, P. Yang, and A. Y. Du, "Crystalline amorphous semiconductor superlattice," *Phys. Rev. Lett.*, vol. 100, p. 136101, Mar 2008.

[15] M. L. Gallo and A. Sebastian, "An overview of phase-change memory device physics," *Journal of Physics D: Applied Physics*, vol. 53, p. 213002, mar 2020.

[16] L. Zhou, Z. Yang, X. Wang, H. Qian, M. Xu, X. Cheng, H. Tong, and X. Miao, "Resistance drift suppression utilizing GeTe/Sb2Te3 superlattice-like phase-change materials," *Advanced Electronic Materials*, vol. 6, no. 1, p. 1900781, 2020.

[17] d. L. R. Kronig and W. G. Penney, "Quantum mechanics of electrons in crystal lattices," *Proceedings of the Royal Society London A*, vol. 130, pp. 499–513, 1931.

[18] A. J. Dekker, *Solid State Physics*. Prentice-Hall, New York, 1957.

[19] A. Zakery and S. R. Elliot, *Optical Nonlinearities in Chalcogenide Glasses and their Applications*. Springer, Berlin Heidelberg, 2007.

[20] E. A. Davis, "Optical absorption, transport and photoconductivity in amorphous selenium," *Journal of Non-Crystalline Solids*, vol. 4, pp. 107–116, 1970.

[21] R. L. Anderson, "Experiments on Ge-GaAs heterojunctions," *Solid-State Electronics*, vol. 5, pp. 341–351, 1962.

[22] G. S. Belev, *Electrical properties of amorphous selenium based photoconductive devices for application in X-ray image detectors*. PhD thesis, Department of Electrical and Computer Engineering, University of Saskatchewan, Saskatoon, SK, Canada, Jan 2007.

[23] M. Abkowitz, "Density of states in a-Se from combined analysis of xerographic potentials and transient transport data," *Philosophical Magazine Letters*, vol. 58, no. 1, pp. 53–57, 1988.

[24] G. Pfister and M. Morgan, "Defects in chalcogenide glasses I. The influence of thermally induced defects on transport in a-As_2Se_3," *Philosophical Maganize Part B*, vol. 41, pp. 191–202, Jul 1980.

[25] N. F. Mott, "Electrons in non-crystalline materials: The last twenty five years," *Contemporary Physics*, vol. 26, pp. 203–215, Mar 1985.

[26] E. Antonelli, A. Tarnow and J. D. Joannopoulos, "New insight into the electronic structure of As_2Se_3," *Physical Review B*, vol. 33, pp. 2968–2971, Feb 1986.

[27] P. Blood, *Optical transitions in quantum wells*. Oxford: Oxford University Press, 2015.

[28] M. Fox and R. Ispasoiu, *Quantum Wells, Superlattices, and Band-Gap Engineering*. Cham: Springer International Publishing, 2017.

[29] V. V. Mitin, V. A. Kochelap, and M. A. Stroscio, *Quantum heterostructures : microelectronics and optoelectronics*. Cambridge University Press, Cambridge, 1999.

[30] S. M. Sze, *Physics of semiconductor devices*. Wiley, New York, 1990.

[31] J. I. Pankove, *Optical Processes in Semiconductors*. Dover Publications, 1975.

[32] S. R. Elliot, *Physics of amorphous materials*. Longman Scientific, New York, 1990.

[33] H. Fujiwara, *Spectroscopic Ellipsometry: Principles and Applications*. John Wiley and Sons, 2007.

Appendix B

Deep Level Transient Fourier Spectroscopy (DLTFS)

B.1 Background

In 1974, D. V. Lang introduced a method of characterizing deep levels using capacitance transients and thermal scanning [1]. This method can reveal the nature of deep levels, whether they are majority or minority carrier traps, as well as their concentrations, capture and emission rates as well as their energy level. This method has been applied to evaluating energy levels in amorphous materials and in superlattice structures [2, 3]. The method is based on the variable capacitance of a material junction. A basic understanding can be built up from the p-n junction. The capacitance, C, of a p-n junction is characteristically similar to that of a parallel plate capacitor, expressed as

$$C = \frac{\epsilon_s A}{W} \tag{B.1}$$

where ϵ_s is the material dielectric constant and W is the width of the space charge region. The width of the space charge region depends on the built-in potential of the junction, V_{bi}, the doping concentrations of the p-side and n-side, N_A and N_D respectively, and the applied reverse voltage V_R [4, 5],

$$W^2 = \frac{2\epsilon_s(V_{bi} - V_R)(N_D + N_A)}{qN_D N_A} \tag{B.2}$$

If one side is much more heavily doped than the other a one-sided junction is formed. Taking the case where $N_A >> N_D$, the space charge width is much larger in the n-side and has the form

$$W^2 = \frac{2\epsilon_s(V_{bi} - V_R)}{qN_D} \tag{B.3}$$

If there are deep level trap states in the space charge region, they will capture some carriers, and in this case the value of N_D has to be adjusted for the filled trap levels n_T,

$$N_D^{'} = N_D - n_T \tag{B.4}$$

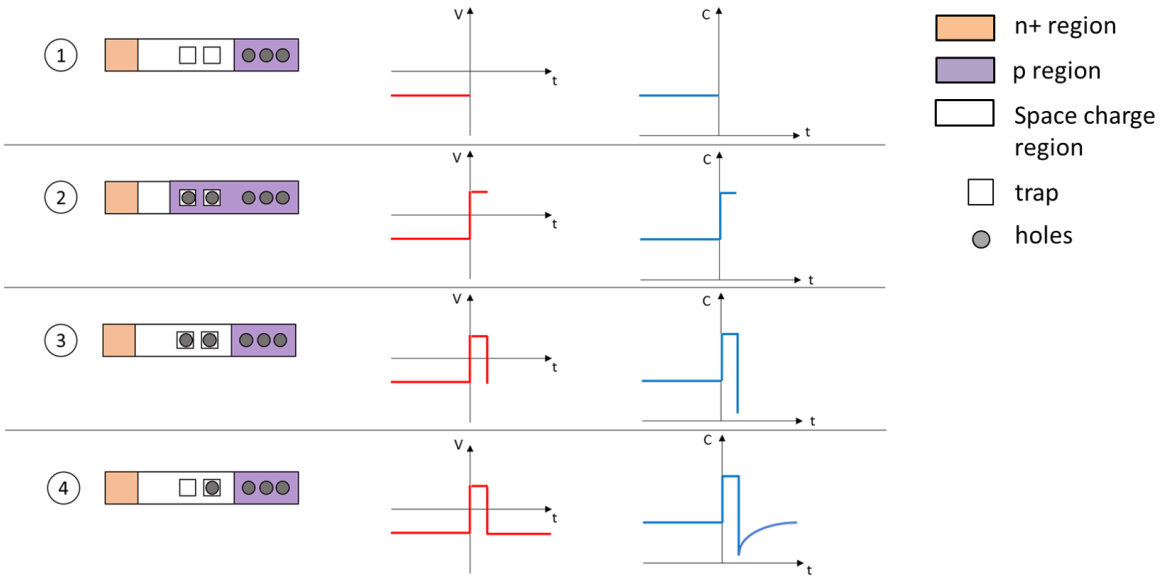

Figure B.1: The sequence of steps during a DLTS measurement. (1) the initial state with the junction in equilibrium mode, (2) a trap filling pulse is applied which narrows the junction and introduces carriers into traps available in the junction, (3) upon release of the pulse, the junction once again depletes with an added consequence that trapped carriers will emit at a different rate, and (4) The capacitance shows a transient related to the emission from trap levels, which can be used to find the energy levels of the traps.

so that the space charge width becomes

$$W^2 = \frac{2\epsilon_s(V_{bi} - V_R)}{qN_D'} \tag{B.5}$$

The space charge region may contain a total density of traps, N_T, of which a density n_T may be filled. In steady state conditions, if electrons are emitted from the traps at a rate e_n, and holes emitted at a rate e_p, then the ratio of filled states to the total density is related to the ratio of the rate of emission of holes to the total emission,

$$\frac{n_T}{N_T} = \frac{e_p}{e_p + e_n} \tag{B.6}$$

A transient condition can be applied to the junction by initially holding the junction at a reverse bias V_R, then applying a short pulse before reverting to the reverse bias, as shown in Fig. B.1.

When the pulse is applied (Fig. B.1 stages 1 to 2) the previously unoccupied traps will capture electrons. Assuming that the electrons are not immediately emitted, the rate of change of filled traps is the same as the rate of capture of electrons, c_n by the unoccupied traps,

$$\frac{dn_T}{dt} = c_n(N_T - n_T) \tag{B.7}$$

When the pulse is released (Fig. B.1 stage 3), the space charge region will once again be depleted of any free carriers. The traps which had captured electrons will now emit the electrons with time, The change in electron filled traps with time is the difference between the emission of electrons from filled states from the emission of holes from captured in the states unoccupied by electrons,

$$\frac{dn_T}{dt} = e_p(N_T - n_T) - e_n n_T \tag{B.8}$$

$$= e_p N_T - (e_p + e_n)n_T \tag{B.9}$$

This is a linear first-order differential equation,

$$\frac{dn_T}{dt} + (e_p + e_n)n_T = e_p N_T \tag{B.10}$$

A solution can be obtained using the initial conditions $t = 0$, $n_T = N_T$

$$n_T(t) = \frac{e_p}{(e_p + e_n)}N_T + \frac{e_n}{(e_p + e_n)}N_T \exp\left[-(e_p + e_n)t\right] \tag{B.11}$$

Therefore the electron filled traps decrease exponentially (Fig. B.1 stage 4) with a time constant

$$\tau = \frac{1}{(e_p + e_n)} \tag{B.12}$$

For an electron emitting trap, the emission rate of electron will be much greater

than that for holes ($e_n >> e_p$). The time constant becomes $\tau = \frac{1}{e_n}$, so that

$$n_T(t) = N_T \exp(-e_n t) \tag{B.13}$$

Since the capacitance per unit area depends on filled traps n_T, the capacitance will reflect the transient feature,

$$C_A = C_{A0}\left[1 - \frac{N_T}{2N_D}\exp\left(-\frac{t}{\tau}\right)\right] \tag{B.14}$$

In this way, capacitance measurements reveal the trap concentration and the emission rates of trapped carriers.

Arrhenius Equation

The emission rate constant can also be expressed in terms of activation energy, E_a using the Arrhenius equation,

$$e_n = A\exp\left(-\frac{E_a}{k_B T}\right) \tag{B.15}$$

An electron is considered emitted when it acquires enough energy to leave the trap level and reach the conduction band where it can be transported to the contacts. Thus the activation energy,

$$E_a = E_C - E_T \tag{B.16}$$

where E_C is the conduction band energy and E_T is the energy at the trap level. The exponential term becomes

$$\exp\left(-\frac{(E_C - E_T)}{k_B T}\right) \tag{B.17}$$

and represents the fraction of carriers with enough energy to emit from the trap level to the conduction band.

The pre-exponential factor A contains the thermal velocity v_{th}, capture cross-section

σ, and the effective density of states in the conduction band N_C,

$$A = \sigma v_{th} N_C \tag{B.18}$$

$$v_{th} = \frac{3k_B T}{m_n^*} \tag{B.19}$$

$$N_C = 2\left[\frac{2\pi m_n^* k_B T}{h^2}\right]^{\frac{3}{2}} \tag{B.20}$$

The complete form of the emission rate is then

$$\frac{1}{\tau_n} = e_n = \sigma v_{th} N_C \exp\left[-\frac{(E_C - E_T)}{k_B T}\right] \tag{B.21}$$

Thus, if the capacitance transient time constants are observed at varying temperatures, it is possible to determine the energy level of trap states.

B.1.1 Fourier transform of the transient

The capacitance transient in Equation B.14 has the form of a real exponential law of time

$$f(t) = A\exp\left(-\frac{t + t_0}{\tau}\right) + B \tag{B.22}$$

where A is the amplitude and B is the offset, τ is the time constant and $-t_0$ is the time at the end of the charging pulse [6].

Fourier coefficients for the function over a time window $[0, T_W]$ are obtained as

$$a_0 = \frac{2A}{T_W}\exp(-t_0/\tau) \times [1 - \exp(-T_W/\tau)]\tau + 2B \tag{B.23}$$

$$a_n = \frac{2A}{T_W}\exp(-t_0/\tau) \times [1 - \exp(-T_W/\tau)]\frac{1/\tau}{1/\tau^2 + n^2\omega^2} \tag{B.24}$$

$$b_n = \frac{2A}{T_W}\exp(-t_0/\tau) \times [1 - \exp(-T_W/\tau)]\frac{n\omega}{1/\tau^2 + n^2\omega^2} \tag{B.25}$$

By taking the ratio between coefficients, there are three possible combinations of the

coefficients that give the time constants [6]:

$$\tau(a_n, a_k) = \frac{1}{\omega}\sqrt{\frac{a_n - a_k}{k^2 a_k - n^2 a_n}} \tag{B.26}$$

$$\tau(b_n, b_k) = \frac{1}{\omega}\sqrt{\frac{kb_n - nb_k}{k^2 nb_k - n^2 kb_n}} \tag{B.27}$$

$$\tau(a_n, b_n) = \frac{1}{n\omega}\frac{b_n}{a_n} \tag{B.28}$$

These time constants can then be used in the Arrhenius equation to give energy levels, as in Equation B.21.

The motivations and advantages for using the Fourier transform are discussed in detail in literature [7, 6]. One advantage is the automation of the measurement and analysis methods, which remove the need to manually determine peaks. Another benefit is the reduced error since there is no dependence on amplitude, as can be seen in the time constants equations B.26. Our interest in this method was in its ability to distinguish plural trap energy levels. It is difficult just by manual observation to distinguish a decay curve as having one or more time constants, and similarly whether a peak is single or has adjacent peaks. DLTFS measures the whole transient, and taking the Fourier transform reveals if there are additional time constants to the transient. As such, DLTFS results in a higher resolution compared to DLTS.

References

[1] G. L. Miller, D. V. Lang, and L. C. Kimerling, "Capacitance transient spectroscopy," *Annual Review of Material Science*, vol. 7, no. 1, pp. 377–448, 1977.

[2] S. R. Elliot, *Physics of amorphous materials*. Longman Scientific, New York, 1990.

[3] S. Q. Wang, F. Lu, H. D. Jung, C. D. Song, Z. Q. Zhu, H. Okushi, B. C. Cavenett, and T. Yao, "Electronic states in ZnSe/ZnTe type-II superlattice studied by capacitance transient spectroscopy," *Journal of Applied Physics*, vol. 82, no. 7, pp. 3402–3407, 1997.

[4] S. M. Sze, *Physics of semiconductor devices*. Wiley, New York, 1990.

[5] D. A. Neamen, *Semiconductor physics and devices : basic principles*. McGraw-Hill, New York, 2003.

[6] S. Weiss and R. Kassing, "Deep Level Transient Fourier Spectroscopy (DLTFS) - A technque for the analysis of deep level properties," *Solid-State Electronics*, vol. 31, pp. 1733–1742, Jun 1988.

[7] M. Okuyama, H. Takakura, and Y. Hamakawa, "Fourier transformation analysis of deep level transient signals in semiconductors," *Solid-State Electronics*, vol. 26, pp. 689–694, Aug 1983.

Appendix C

Spectroscopic Ellipsometry

C.1 Spectroscopic Ellipsometry

Ellipsometry in an optical characterization technique that uses polarized incident light to probe the material surfaces and characterize their properties by measuring the reflected light from the sample [1, 2]. Incident light with parallel polarization (p-polarization) and perpendicular polarization (s-polarization) (with respect to the sample) is directed to the surface of a sample under measurement. This light is reflected (and/or transmitted) and usually the polarizatio changes to an ellipse. Measuring the polarization of this ellipse gives information on the characteristics of the sample surface, hence the name [1]. Specifically, it is the ratio of the reflection coefficients for p-polarized and s-polarized, R_p and R_s, respectively, which are measured [3], and these parameters are given as

$$\rho = \frac{R_p}{R_s} = \tan(\Psi)\exp(i\Delta) \tag{C.1}$$

where Ψ and Δ are the amplitude and phase of the complex ratio. The spectroscopy aspect of the measurement is that the energy of the incident photons can be varied, from visible light, to ultraviolet light, providing an additional degree of measurement. Since reflection depends on the angle of incidence, Φ, this angle can also be used as a measurement parameter in Variable Angle Spectroscopic Ellipsometry (VASE) [3, 2].

To analyze the measurement, a model is assumed and the measured data is numerically fitted to the calculated assumed model [4, 1]. Using regression analysis the model parameters are varied until the calculated model and measured data converge as closely as possible, as measured by a goodness of fit parameter, for example a minimum mean square error (MSE) [3]:

$$\text{MSE} = \frac{1}{N}\sum_i [(\Psi_{ci} - \Psi_{mi})^2 + (\Delta_{ci} - \Delta_{mi})^2]^{1/2} \tag{C.2}$$

where, the subscripts c and m represent the ith data element for the calculated model and measured data, respectively.

The measured values are then used to obtain the complex dielectric function ϵ, or

the complex refractive index $\tilde{n}$, as

$$\langle\epsilon\rangle = \langle\epsilon_1\rangle + i\langle\epsilon_2\rangle \tag{C.3}$$

$$(\tilde{n})^2 = (\langle n\rangle - i\langle k\rangle)^2 \tag{C.4}$$

$$= \left[\left(\frac{1-\rho}{1+\rho}\right)\sin^2\Phi\tan^2\Phi + \sin^2\Phi\right] \tag{C.5}$$

where, ϵ_1 and ϵ_2 are the real and imaginary parts, respectively, of the complex dielectric function, n is the refractive index, and k is the extinction coefficient [4]. Here, the angle braces $\langle\rangle$ indicate that these are not the intrinsic optical parameters, but rather pseudo-optical parameters, since the samples are measured under assumptions that they have no surface roughness, no oxide, no overlayers nor additional films [1, 2].

Mathematical and physics-based models have been developed that can be used to parameterize the measured dielectric function. Here we discuss the mathematical B-Spline model and the physics-based Lorentz and Cody-Lorentz models.

C.2 B-Spline model

The basis spline (B-Spline) model represents a basis set of polynomial splines which have basis functions defined by [5, 6]

$$B_i^0(x) = \begin{cases} 1 & t_i \leq x < t_{i+1} \\ 0 & \text{otherwise} \end{cases} \tag{C.6}$$

$$B_i^k(x) = \left(\frac{x - t_i}{t_{i+k} - t_i}\right) B_i^{k-1}(x) + \left(\frac{t_{i+k+1} - x}{t_{i+k+1} - t_{i+1}}\right) B_{i+1}^{k-1}(x) \tag{C.7}$$

where k is the degree of the B-Spline, t_i is the ith knot location on the x-axis. Knots also known as nodes are locations on the x-axis where the polynomial segments connect. A spline curve $S(x)$ is then a linear sum of N basis functions weighted with coefficients

c_i:

$$S(x) = \sum_{i=1}^{N} c_i B_i^k(x) \tag{C.8}$$

In spectroscopic ellipsometry, B-Splines can be applied to parameterize arbitrary dielectric functions which could not be directly or immediately identified with a particular physical model, as is the case in investigating new materials or material combinations. The dielectric function is mapped to the B-Spline as

$$\epsilon_2(\omega) = \sum_{i=1}^{N} c_i B_i^k(\omega) \tag{C.9}$$

where ω is the frequency of the light. The real part of the dielectric function can then be obtained using Kramers-Kronig causality relations [5, 7]. From the convex hull property, the B-Spline curve coefficients c_i can be used to enforce $\epsilon_2 \geq 0$ so that the model maintains physical sense [5]. CompleteEASE analysis software uses degree $k = 3$ B-Splines with the number of nodes set by selecting the resolution of the spline [6, 2].

C.3 Lorentz model

The Lorentz model is a classical model in which an atom is considered as a positively charged nucleus binding a negatively charged electron with spring, like a mass-spring system [1]. An alternating electric field from light, in the plane of the mass-spring will cause dielectric polarization,and the electron will oscillate as if it is in a viscous fluid. The nucleus is taken to be much heavier than the electron such that the nucleus is stationary and only the electron oscillates. The resulting oscillations represent the polarization which in turn represents the dielectric properties.

The Lorentz oscillator gives the dielectric function ϵ as [1, 2]

$$\epsilon = \frac{A_n E_{0n} \Gamma_n}{E_{0n}^2 + E^2 - iE\Gamma_n} \tag{C.10}$$

where, for the nth oscillator,

- A_n is the amplitude of the Lorentzian peak,
- Γ_n is the Full Width Half Maximum (FMHW) of the Lorentzian peak,
- E_{0n} is the energy at the peak position ,

This model is symmetrical and has a resonant feature and thus could be used to represent interband transitions.

C.4 Cody-Lorentz model

The Cody-Lorentz model is usually applied for semiconductor amorphous materials [2]. It models a zero absorption below a defined optical band gap, and a main absorption broad Lorentzian peak. In addition to absorption at energies above the optical band gap, the Cody-Lorentz model takes into account the Urbach absorption below the band gap, which is expected for amorphous materials [1, 2]. In the Cody-Lorentz oscillator, the imaginary part of the dielectric function $\epsilon_2(E)$ has the form [8]

$$\epsilon_2(E) = \begin{cases} \frac{E_l}{E} \exp\left[\frac{(E - E_{gn} + E_{tn})}{E_{un}}\right] & : 0 < E \leq (E_{gn} + E_{tn}) \\ \\ \frac{(E - E_{gn})^2}{(E - E_{gn})^2 + E_{pn}^2} \cdot \frac{A_n E_{0n} \Gamma_n E}{(E^2 - E_{0n}^2) + \Gamma_n^2 E^2} & : E > (E_{gn} + E_{tn}) \end{cases}$$

where, for the nth oscillator,

- A_n is the amplitude of the Lorentzian peak,
- Γ_n is the Full Width Half Maximum (FMHW) of the Lorentzian peak,
- E_{0n} is the energy at the peak position ,
- E_{pn} is the transition from Lorentzian absorption to Cody absorption,
- E_l is the demarcation energy between band to band and Urbach tail transitions,

- E_{tn} is the transition from Cody absorption to Urbach absorption, and
- E_{un} is the exponential rate of the transition E_t.

Spectroscopic ellipsometry provides an accurate, non-destructive method for evaluating the optical properties of layered semiconductor structures [1]. The method has been successfully applied to superlattice structures, showing excitonic peaks associated with sub-band transitions, and also reliably evaluating the quality of superlattice structures from different deposition conditions [3, 9].

References

[1] H. Fujiwara, *Spectroscopic Ellipsometry: Principles and Applications*. John Wiley and Sons, 2007.

[2] J. A. Woolam, *CompleteEASE Software Manual*. J. A. Woolam Co., Lincoln, USA, 2014.

[3] J. A. Woolam, P. G. Snyder, K. G. Merkel, and S. A. Alterovitz, "Ellipsometric characterization of multilayer transistor structures," *Materials Science and Engineering*, vol. B5, pp. 291–294, 1990.

[4] H. Yao, J. A. Woolam, , P. J. Wang, M. J. Tejwani, and S. A. Alterovitz, "Spectroscopic ellipsometric characterization of $Si/Si_{1-x}Ge_x$ strained-layer supperlattices," *Applied Surface Science*, vol. 63, pp. 52–56, 1993.

[5] B. Johs and J. S. Hale, "Dielectric function representation by B-splines," *physica status solidi (a)*, vol. 205, no. 4, pp. 715–719, 2008.

[6] J. Weber, T. Hansen, V. de Sanden, and R. R. Engeln, "B-spline parametrization of the dielectric function applied to spectroscopic ellipsometry on amorphous carbon," *Journal of Applied Physics*, vol. 106, p. 123503, 2009.

[7] J. I. Pankove, *Optical Processes in Semiconductors*. Dover Publications, 1975.

[8] A. S. Ferlauto, G. M. Ferreira, J. M. Pearce, C. R. Wronski, R. W. Collins, X. Deng, and G. Ganguly, "Analytical model for the optical functions of amorphous semi-

conductors from the near-infrared to ultraviolet: Applications in thin film photovoltaics," *Journal of Applied Physics*, vol. 92, no. 5, pp. 2424–2436, 2002.

[9] P. G. Snyder, B. N. De, K. G. Merkel, and J. A. Woolam, "Measurement of superlattice optical properties by variable angle spectrocopic ellipsometry," *Superlattices and Microstructures*, vol. 4, no. 1, pp. 97–99, 1987.

Appendix D

Radiation detection

D.1 Radiation interaction with matter

Photons

Photons interact with matter in three possible ways [1, 2]:

- Photoelectric effect - primary photon is completely absorbed and the interaction occurs with the entire electron cloud surrounding the the atomic nucleus.
- Compton scattering - photon scatters on atomic electrons which are treated as quasi-free since the electron binding energy is ignored.
- Pair production - photon has energy high enough to create electron-positron pair in the Coulomb field of an electron or a nucleus.

Each of the methods will be reviewed in detail.

A monochromatic beam of photons of intensity I_0 incides on the surface of an absorbing material in the x-direction, as shown in Fig. D.1. Suppose that the material

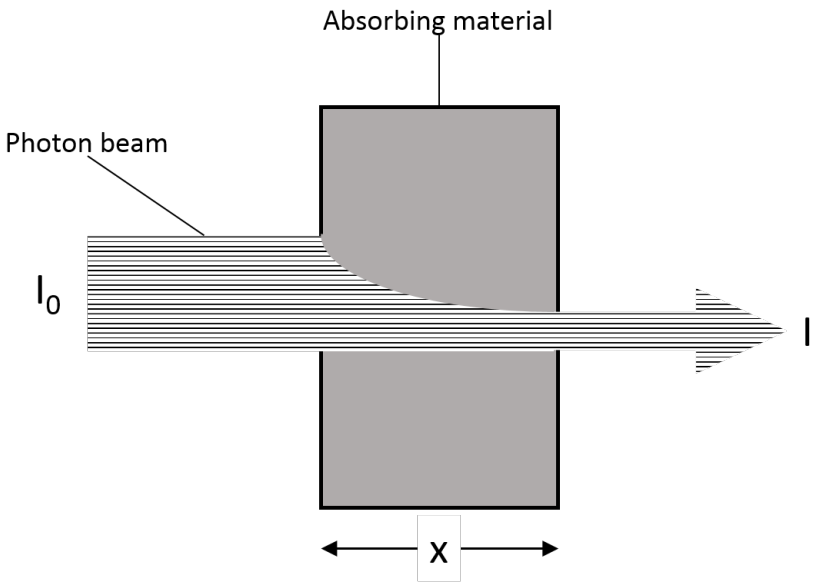

Figure D.1: A beam of monochromatic photons traversing through an absorbing medium (adapted from [1]).

has an atomic cross-section, σ_a, for absorbing or scattering photons with energy equal

to the monochromatic beam. As the beam traverses through the absorber, the aforementioned interactions (Sec. D.1) will occur for individual photons, removing them from the beam. As a result the beam will have its intensity (photon rate) decrease by dI after a distance dx. This rate at which the intensity decreases is then proportional to the atomic cross-section σ_a, the number of atoms per unit volume n_A and the beam intensity I' at a depth x'.

$$-dI = \sigma_a n_A I' dx' \Rightarrow \int_{I_0}^{I} \frac{dI}{I'} = \int_0^x \sigma_a n_A dx' \tag{D.1}$$

This gives the Beer-Lambert law

$$I = I_0 \exp[-(\mu_{att,l} x)] \tag{D.2}$$

where $\mu_{att,l} = \sigma_a n_A$ [cm^{-1}] is the linear attenuation coefficient. The number of atoms per unit volume $n_A = (\rho N/A)$ where

- N is the Avogadro number,
- ρ is the density of the material,
- Z is the atomic number of the material,
- A is the atomic weight of the material.

Using these substitutions the mass attenuation length is obtained as $\mu_{att,m} = \sigma_a n_A/\rho$ [g^{-1}cm^2], or in other words $\mu_{att,m} = \mu_{att,l}/\rho$. For chemical compounds the mass attenuation coefficient is a weighted average of the individual elements

$$\mu_{att,m} = \sum_i w_i \mu_{att,m,i} \tag{D.3}$$

For photon detection the general requirement is that the absorption be high, which means that $\mu_{att,l}$ must be large. We examine the absorption cross-section σ_a in more detail for each of the possible interactions of photons with electrons.

Photoelectric effect - The photoelectric effect is the dominant interaction process for photons with energy under 100 keV. In this process, atomic electrons absorb the total energy of the incoming photon, provided that the photon energy is higher than the binding energy E_B of the atomic electron, which can be expressed as

$$\gamma + atom \rightarrow atom^+ + e^- \tag{D.4}$$

where γ is the photon and e^- is the electron.

It can be shown that the absorption cross-section has a dependence on Z^5. This has at least two implications. First is that at low energies, an interaction between photons and isolated electrons is almost impossible. This interaction basically requires a nuclear presence. Second is that the absorption cross-section is vastly improved for higher numbers of Z. This is why recent research in absorbing materials has focused on the so called high-Z materials such as CdZnTe, HgI_2, PbO and perovskite materials like $MAPbI_3$ [3, 4, 5, 6].

If the photoelectric effect occurs in the inner shells of the atom, say the K-shell, there is a possibility of secondary effects. The electron ejected from the K-shell leaves a hole, and the whole atom is in an excited state. An electron from a higher shell, say L-shell, can drop to fill the hole and release energy in the form of a photon with energy difference between the higher L-shell and K-shell, $E_K - E_L$. This photon usually is within X-ray energy range and can cause another photoelectric absorption in the same atom or neighboring atoms. If this new photon has energy higher than the binding energy of some shell, say L1, ($E_K - E_L > E_{L1}$) of the atom, another electron will then be released from the atom. This is the Auger effect, and the Auger electron will of course have smaller energy, $E_K - 2E_L$, than the initial/primary electron.

Compton scattering - Compton scattering is the dominant interaction in the energy ranges close to 1 MeV. The incident photon interacts with an electron as

$$\gamma + e^- \rightarrow \gamma + e^- \tag{D.5}$$

While Compton scattering is applicable to other charged particles, for detection we are concerned mostly with the interaction with atomic electrons.

Pair production - Above 1 MeV, interactions of photons with matter result in the formation electron-positron pair. This interaction occurs in the electric field of the nucleus, described as

$$\gamma + \text{nucleus} \rightarrow e^- + e^+ + \text{nucleus} \tag{D.6}$$

This interaction only occurs when the energy exceeds a certain threshold. This threshold is obtained by considering the rest masses of the electron and positron and the recoil energy that is transferred to the atomic nucleus. Since momentum is conserved the threshold energy is

$$E_\gamma \geq 2m_e c^2 + 2\frac{m_e}{m_{nucleus}} m_e c^2 \tag{D.7}$$

but since $m_{nucleus} >> m_e$ the threshold is

$$E_\gamma \geq 2m_e c^2 \tag{D.8}$$

which is 1.02 MeV.

Using data from the National Institute of Standards and Technology (NIST) XCOM webpage (https://www.physics.nist.gov/PhysRefData/Xcom/html/xcom1.html) [7]. We used this data to plot the attenuation for our materials of interest, Si, Ge and a stoichiometric equivalent of the amorphous Se superlattice. We assume an equal number of layers and each layer of material to be the same width so that the Se and As_2Se_3 have equal volume. The attenuation characteristics are shown in Fig. D.2.

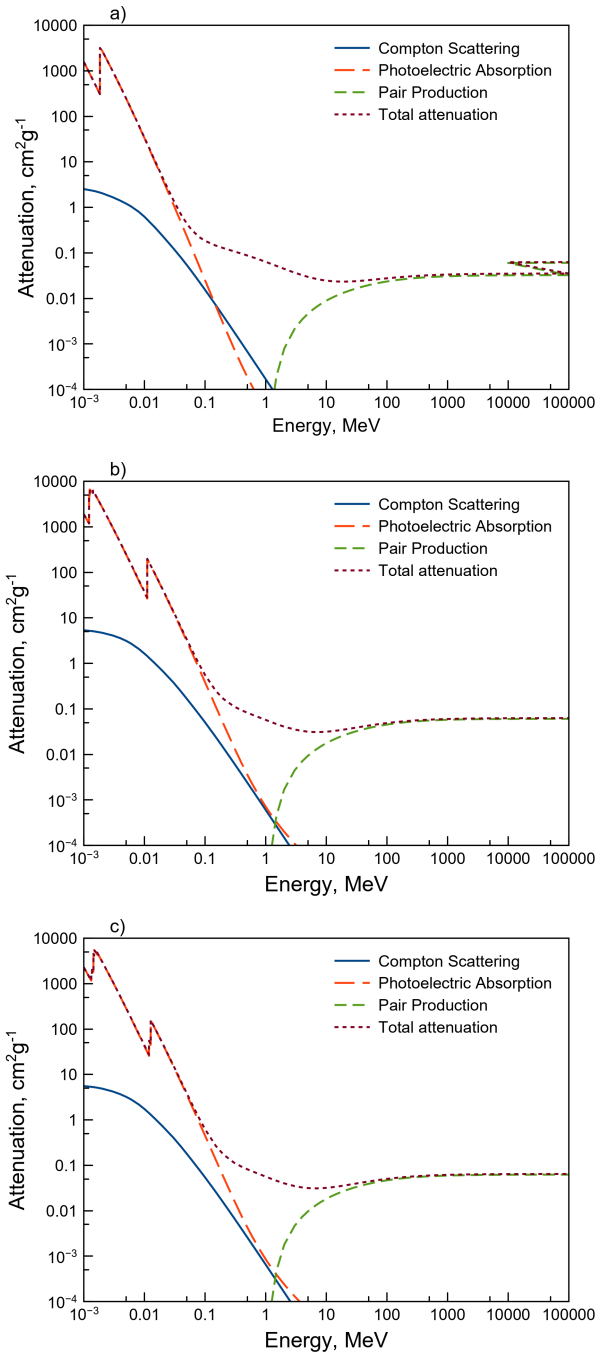

Figure D.2: The attenuation characteristics of high energy photons in (a) Si, (b) Ge, and (c) a stoichiometric equivalent of the amorphous Se superlattice, due to photoelectric absorption, Compton scattering and pair production. The data is obtained from the NIST XCOM website https://www.physics.nist.gov/PhysRefData/Xcom/html/xcom1.html

D.1.1 Radiation-generated charge

Upon interacting with matter, radiation generates charge. Here we describe interactions of radiation with semiconductor materials which we can then use for detection [8, 1].

Visible and ultraviolet photons

An inciding photon generally produces a single electron-hole pair. The photon is absorbed in regions within micrometers from the exposed surface.

X-ray photons

Similar to visible and ultraviolet photons, X-rays will interact at a point, however with the difference that they will produce many electron-hole pairs in the small region of the point. The number of electron-hole pairs from an X-ray interaction can be estimated if the ionisation energy i.e. average energy required to create a single electron-hole pair. For Si, the ionization energy is 3.6 eV.

The next part of the review now discusses the practical application of the foregoing properties and phenomena for radiation detection. The interactions of radiation with matter are used to identify and measure the properties of specific particles.

D.2 Solid state detector materials

D.2.1 Solid state scintillators

Scintillator materials are in the category of so called indirect conversion materials. In indirect conversion, the incident photon is down-converted in energy before being detected. In the case of X-rays, the keV photon is down-converted to energy in the visible photon range which is then detected. The main advantage of scintillators is that they allow taking advantage of well established visible light detectors such as Si CCD or CMOS. However there is cost of efficiency since the mechanism inherently has two

absorption stages, first for the high energy photon and then for the low energy photon after down-conversion.

The basic operation of scintillators depends on activation sites in the band gap of an absorbing material, usually a wide gap material, as illustrated in Fig. D.3. A well

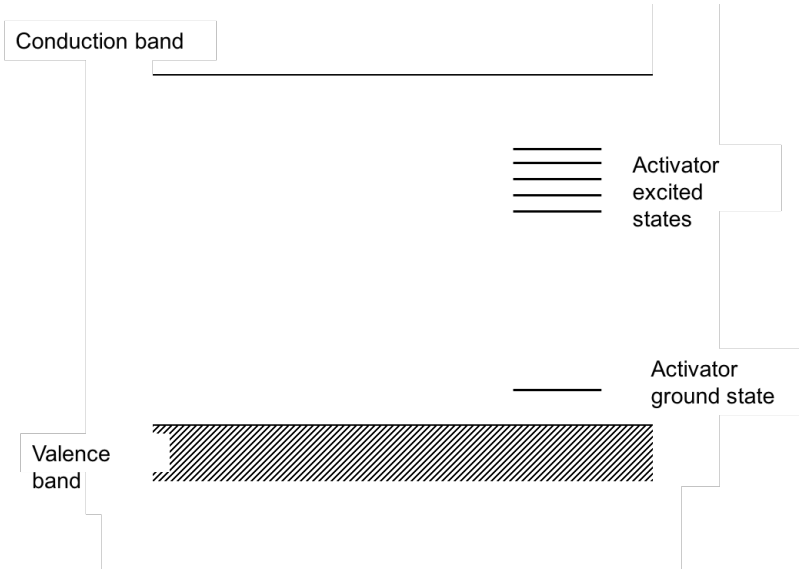

Figure D.3: The band diagram of a scintillator.

known solid state scintillator is NaI which has a direct band gap of 5.8 eV. Were it to emit photons, they would be in the middle ultraviolet range. To use this material as a scintillator producing visible photons, a dopant of Tl is added to the NaI crystal and the material is referred to as NaI(Ti). The addition of Tl creates activator sites in the band gap separated by about 3 eV between activator excited states and the activator ground state.

Solid-state scintillator down-conversion mechanism involves three stages: absorption, transport and luminescence [9]. When an incident radiation particle has enough energy it generates electron-hole pairs whereby electrons are excited to the conduction band. The electrons are transported in the conduction band and may experience trapping depending on the defect structure of the material. Similarly, holes transport in the valence band. When eventually these carriers encounter an activator site where they ionize the site. The electron is in an excited state and de-excites to the ground state. The de-excitation has a high probability of emitting a photon, and since the

activator was specifically chosen, the photon is within visible light range. The timing of the light output depends on the half-life of the activator excited state, represented by a decay time constant.

The emitted photons have lower energies compared to the band gap of the crystal and the photons that caused the original excitation, and this shift in energy is referred to as the Stokes Shift, illustrated in Fig. D.4. This allows the scintillated light to propagate through the crystal without being reabsorbed.

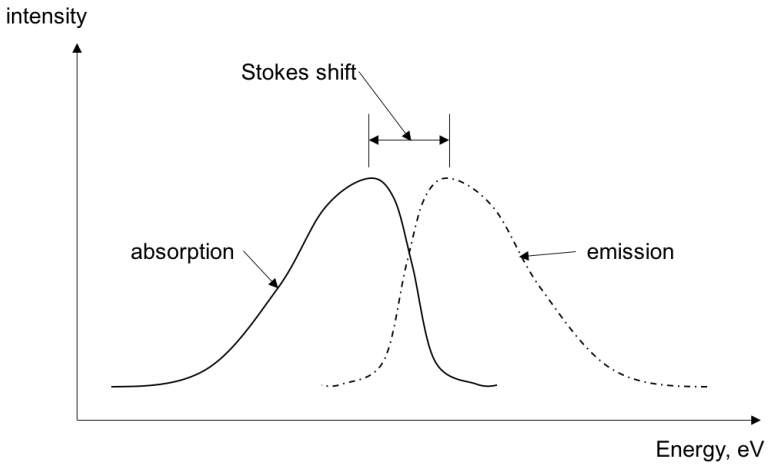

Figure D.4: An intensity vs. photon energy plot showing the Stokes shift.

Scintillators are evaluated using the following criteria

- Emission spectrum and peak wavelength - Ideally this should be within the visible range so that conventional light detectors e.g. CCD can be used.
- Light yield - This should be high as it indicates the efficiency with which ionization energy is converted to visible light.
- Decay time constant - this is a measure of how long it takes for activator excited states to de-excite to the ground state. A short time constant is good for the response time of the device.
- Density and Z - These characteristics determine the response to the energy of the incident photon. As we have seen before, high Z and density make for a more efficient absorber.

Scintillators have challenges due to the many stages of conversion of particles before the signal is eventually read out. This limits their potential for applications that require ultrahigh sensitivity, or where the number of particles to be measured are low. To illustrate the limitation the following analysis is usually presented [9]. The number of visible photons, N_{ph}, produced from an X-ray photon of energy E in a material of band gap E_g is

$$N_{ph} = \left(\frac{E}{\beta E_3}\right) SQ \tag{D.9}$$

S and Q are the efficiencies of transport and visible photon generation respectively, and $\beta \approx 3$ from Klein's rule. The relative efficiency can then be

$$\eta = \frac{E_{vis} N_{ph}}{E} \tag{D.10}$$

where E_{vis} is the energy of the visible light photons. Since we always want visible photons from the scintillator, $E_g > 3$ eV. Furthermore, the efficiencies S and Q are also limited so is the number of visible photons, and the relative efficiency is usually less than 20%.

This analysis makes a case for direct conversion so as to eliminate the dependence on Q and subsequently the case for small E_g absorbers. Materials such as Si and Ge fit this description.

D.2.2 Conventional materials: Silicon and Germanium

Successful detection can be discussed in terms of signal to noise ratio (SNR), where detection is successful if the SNR is greater than one. This implies that the signal must always be greater than the noise.

As previously discussed, the signal comes from the radiation particle interacting with the material and generating electrons. Electrons in the material can only be generated if the radiation particle provides a certain threshold amount of energy to the

material. This relationship of energies has been described by the Klein rule [10]

$$W_{\pm} \approx 3E_G \tag{D.11}$$

where W is the ionization energy, or the energy required to generate an electron-hole pair. This is the minimum energy that a radiation particle must supply, and if a particle has more energy then more electron-hole pairs will be generated. E_G is the material band gap. From the Klein rule, materials with small band gap are desirable so as to get a larger signal, which is why Ge and Si have become conventional, among other reasons.

Noise in the detector refers to any carriers that are not generated by the radiation particle. The semiconductor material has an intrinsic carrier concentration. These carriers exist because the band gap in semiconductors is small enough for some electrons to be excited to the conduction band from the valence band even at room temperatures. In the valence band holes are left in place of the excited electron. Therefore in a semiconductor in its intrinsic form, the number of electrons is the same as holes, $n_e = n_h = n_i$, and this intrinsic carrier concentration is

$$n_i = \sqrt{N_C N_V} \exp\left(-\frac{E_G}{2kT}\right) \propto T^{\frac{3}{2}} \exp\left(-\frac{E_G}{2kT}\right) \tag{D.12}$$

where N_C and N_V are the effective density of states in the conduction and valence bands respectively. The intrinsic carrier concentration depends on the band gap and on the temperature. From this relationship large band gap materials are required if noise is to be limited at room temperatures, otherwise the detector device has to be operated at low temperatures.

From the foregoing analysis we arrive at two contradictory conditions: a large signal requires a material with a small band gap; reduced noise required a material with a large band gap. There are optimizations that can be done to still obtain performance despite the contradiction. First, the detector could be operated at lower temperature,

which reduces the noise without affecting the signal. This strategy is applied in Ge detectors and some Si detectors which are cooled to LN_2 temperatures. Second, is to choose material with an optimum band gap for operation at room temperature. A third strategy is to use differently doped materials and produce depletion zones such as the p-n junction.

D.2.3 Amorphous Selenium and other new materials

Amorphous selenium was one of the first materials used for solid state detection of X-ray [11, 12]. The material was used as a xeroradiography detector. Even in recent development of Flat Panel X-ray Images (FPXI) using thin film transistor (TFT) active matrix arrays, amorphous Se has been very successful with some devices commercialized [13]. As such the material has proven properties which could be used for detection.

Chief among the advantages of amorphous Se is the ability to process the material in large areas [14, 11, 15, 16]. As previously stated, Si and Ge are expensive to process for large area applications. Amorphous Se is fabricated from source materials using vacuum evaporation with uniform and reliable electronic properties. Nevertheless, there are other possible materials materials which can also be produced in large areas. Table D.1 summarizes the important properties of amorphous Se and other promising candidates for FPXI devices [13]..

Recent reports have shown multi-layered PbO as a promising candidate for direct conversion X-ray detectors [5]. While polycrystalline PbO is well established since the days of PLUMBICONs, it had issues with lag. It has been shown that multi-layering the polycrystalline PbO with a layer of amorphous PbO reduces the lag, allowing for possible real-time application. However, the sensitivity of the material remains limited.

Table D.1: Properties of amorphous Se and other upcoming materials for FPXI development [13].

Material	Preparation	δ at 20 keV [μm]	E_G [eV]	$W_\pm$ [eV]	Electron $\mu_e\tau_e$ [cm^2/V]	Hole $\mu_h\tau_h$ [cm^2/V]
Stabilised amorphous Se	Vacuum deposition	49	2.2	45 (at 10 V/μm)	$3\times10^{-7}-10^{-5}$	$10^{-6}-6\times10^{-5}$
HgI_2	PVD	32	2.1	5	$10^{-5}-10^{-3}$	$10^{-6}-10^{-5}$
$Cd_{0.95}Zn_{0.05}Te$	Vacuum deposition	80	1.7	5	$\approx 2\times10^{-4}$	$\approx 3\times10^{-6}$
PbI_2	PVD	28	2.3	5	7×10^{-8}	$\approx 2^{-6}$
PbO	Vacuum deposition	12	1.9	8	5×10^{-7}	*small*
TlBr	Vacuum deposition	18	2.7	6.5	small	$1.5-3\times10^{-6}$

D.2.4 Perovskites

Recent publications have shown that perovskite materials can be used in X-ray detectors with an improvement in sensitivity of up to ten times compared with amorphous Se and CsI scintillator [17, 4, 6]. The perovskite material methylammonium lead triiodide ($MAPbI_3$) of 1 mm thickness was used as the absorber in a pixel based direct conversion detector. Devices made from this perovskite showed high sensitivities of up to 11 $\mu CmGy_{air}^{-1}cm^{-2}$. The material makes a good absorbing material since it contains materials with high Z, Pb and I. Furthermore, it was demonstrated that this material could be fabricated by printing at low temperature, giving manufacturing advantage on wide area surfaces.

Another recently reported perovskite for X-ray detection is the Ruddleson-Popper (RP) phase layered perovskite $(BA)_2(MA)_2Pb_3I_{10}$ [6]. Devices made from this perovskite were measured to have sensitivities of up to 0.276 C $Gy_{air}^{-1}cm^{-3}$. The devices exhibited a built-in potential which improved charge collection. The devices also showed high diode resistivity up to $10^{12}\Omega$·cm, improving the dark current performance. However, there are still challenges with thermally activated dark current when operated at room temperature and at high applied bias. This tends to make the perovskite unstable and susceptible to degradation, thus there is need to study the durability and long-term performance of these materials. Another issue is image sharpness, since the photogenerated carriers can spread especially when the device is operated at low applied field causing the image to blur. Adding amorphous Se superlattice to the film might be a way to mitigate some of these challenges.

References

[1] C. Leroy and P. Rancoita, *Principles of Radiation Interaction in Matter and Detection*. World Scientific, Singapore, 2009.

[2] J. G. Rocha and S. Lanceros-Mendez, "Review on X-ray detectors based on scintillators and CMOS Technology," *Recent Patents on Electrical Engineering*, vol. 4, pp. 1–26, Sep 2011.

[3] S. Kasap, C. Koughia, J. Berashevich, R. Johanson, and A. Reznik, "Charge transport in pure and stabilized amorphous selenium: re-examination of the density of states distribution in the mobility gap and the role of defects," *Journal of Material Science: Materials in Electronics*, vol. 26, pp. 4464–4658, May 2015.

[4] Y. C. Kim, H. Kim, K, D. Son, D. Jeong, J. Seo, I. T. Choi, Y. S. Han, Y. S. Lee, and N. Park, "Printable organometalic perovskite large-area, low-dose X-ray imaging," *Nature*, vol. 550, pp. 87–91, October 2017.

[5] O. Grynko, T. Thibault, E. Pineau, G. Juska, and A. Reznik, "Bilayer lead oxide X-ray photoconductor for lag-free operation," *Scientific Reports*, vol. 10, no. 20117, pp. 1 –9, 2020.

[6] H. Tsai, F. Liu, S. Shrestha, K. Fernando, S. Tretiak, B. Scott, D. T. Vo, J. Strzalka, and W. Nie, "A sensitive and robust thin-film X-ray detector using 2D layered perovskite diodes," *Science Advances*, vol. 6, no. 15, 2020.

[7] M. J. Berger, J. H. Hubbell, S. M. Seltzer, J. Chang, J. S. Coursey, R. Sukumar, D. S. Zucker, and K. Olsen, "XCOM: Photon Cross Section Database (version 1.5)," *National Institute of Standards and Technology*, 2010.

[8] G. Lutz, *Semiconductor Radiation Detectors*. Springer, Berlin, 1999.

[9] M. Nikl, "Scintillation detectors for X-rays," *Measurement Science and Technology*, vol. 17, pp. R37–R54, feb 2006.

[10] S. Kasap and M. Zangahir Kabir, "Photoconductors for X-ray Image Detectors," in *Handbook of Electronic and Photonic Materials*, pp. 1125–1147, Springer US, 2017.

[11] S. Kasap, J. B. Frey, G. Belev, O. Tousignant, H. Mani, L. Laperriere, A. Reznik, and J. A. Rowlands, "Amorphous selenium and its alloys from early xeroradiography to high resolution X-ray image detectors and ultrasensitive imaging tubes," *physica status solidi (b)*, vol. 246, no. 8, pp. 1794–1805, 2009.

[12] M. M. Wronski, W. Zhao, A. Reznik, K. Tanioka, G. DeCrescenzo, and J. A. Rowlands, "A solid-state amorphous selenium avalanche technology for low photon flux imaging applications.," *Medical physics*, vol. 37, pp. 4982–5000, Sep 2010.

[13] S. Kasap, J. B. Frey, G. Belev, O. Tousignant, H. Mani, J. Greenspan, L. Laperriere, O. Bubon, A. Reznik, G. DeCrescenzo, K. S. Karim, and J. A. Rowlands, "Amorphous and polycrystalline photoconductors for direct conversion flat panel X-ray image sensors," *Sensors*, vol. 11, pp. 5112–5157, May 2011.

[14] Z. Wei and J. A. Rowlands, "Large-area solid state detector for radiology using amorphous selenium," in *Proceedings SPIE Medical Imaging VI: Instrumentation*, vol. 1651, pp. 1–10, SPIE, 1992.

[15] D. C. Hunt, K. Tanioka, and J. A. Rowlands, "X-ray imaging using avalanche multiplication in amorphous selenium: Investigation of depth dependent avalanche noise," *Medical Physics*, vol. 34, pp. 976–986, Feb 2007.

[16] S. Abbaszadeh, C. C. Scott, O. Bubon, A. R. Reznik, and K. S. Karim, "Enhanced detection efficiency of direct conversion X-ray detector using polyimide as hole-blocking layer," *Nature Scientific Reports*, vol. 3, no. 3360, 2013.

[17] J. A. Rowlands, "Material change for X-ray detectors," *Nature*, vol. 550, pp. 47–48, Oct 2017.

Publications and Presentations

Publications

1. **John, J. D.**, Okano, S., Sharma, Nishimoto, S., M., Miyachi, N., Enomoto, K., Ochiai, J., Saito, I., Salvan, G., Masuzawa, T., Yamada, T., Chua, D. H. C., Zahn, D. R. T., Okano, K., "Spectroscopic Ellipsometry of amorphous Se superlattices. **Journal of Physics D: Applied Physics**, 2021 (Accepted manuscript) https://doi.org/10.1088/1361-6463/abf228.

2. **John, J. D.**, Okano, S., Sharma, A., Selyshchev, O., Rahaman, M., Miyachi, N., Enomoto, K., Ochiai, J., Saito, I., Masuzawa, T., Yamada, T., Chua, D. H. C., Zahn, D. R. T., Okano, K., "Observation of two-level defect system in amorphous Se superlattices." **Applied Physics Letters**, 2020, 116(19), 192104. https://aip.scitation.org/doi/10.1063/5.0004570.

3. **John, J. D.**, Okano, S., Sharma, A., Selyshchev, O., Rahaman, M., Miyachi, N., Enomoto, K., Ochiai, J., Saito, I., Masuzawa, T., Yamada, T., Chua, D. H. C., Zahn, D. R. T., Okano, K., "Transport properties of Se/As_2Se_3 nanolayer superlattice fabricated using rotational evaporation." **Advanced Functional Materials**, 2019, 29, 1904758. https://doi.org/10.1002/adfm.201904758.

4. **John, J. D.**, Enomoto, K., Miyachi, N. , Saito, I. , Masuzawa, T. , Chua, D. H., Yamada, T. and Okano, K., "Modifying the electronic properties of Se/n - Si

heterostructure using electrolysis." **Physica Status Solidi B** 2019. https://doi.org/10.1002/pssb.201800445.

5. **John, J. D.**, Saito, I., Toyama, R., Ochiai, J. Yamada, T. Chua, D. H. C. and Okano, K., "Electronic properties and potential applications of the heterojunction between Silicon and multi-nanolayer amorphous Selenium." **Electronics Letters** 2017, 53 (18). https://doi.org/10.1049/el.2017.1413.

6. **John, J. D.**, Saito, I., Toyama, R., Ochiai, J. Yamada, T. Chua, D. H. C. and Okano, K., "Electrolysis as a controllable method for establishing p-n junctions in multi-nanolayer films of amorphous selenium." **Journal of Applied Physics** 2017, 122, 065107. http://dx.doi.org/10.1063/1.4989874.

7. Masuzawa, T., Ohata, A., **John, J. D.**, Saito, I., Yamada, T., Chua, D. H. C., Neo, Y., Mimura, H. and Okano, K., "Formation of p-n junction in a-Se thin film and its application to high sensitivity photodetector driven by diamond cold cathode." **Physica Status Solidi A** 2017, 1700161. https://doi.org/10.1002/pssa.201700161.

Presentations

1. **John, J. D.**, Miyachi, N., Enomoto, K., Okano, S., Masuzawa, T., Yamada, T., Chua, D. H. C., Zahn, D. R. T., and Okano, K., Physical properties of amorphous Selenium superlattice structures for future X-ray detectors, International Vacuum Nanoelectronics Conference (IVNC), Lyon France, July 2020.

2. **John, J. D.**, Miyachi, N., Enomoto, K., Okano, S., Masuzawa, T., Yamada, T., and Okano, K., Physical properties of amorphous Selenium superlattice structures, The 67th Japan Society of Applied Physics (JSAP) Spring Meeting, Tokyo

Japan, March 2020.

3. **John, J. D.**, Okano, S., Sharma, A., Selyshchev, O., Rahaman, M., Miyachi, N., Enomoto, K., Ochiai, J., Saito, I., Masuzawa, T., Yamada, T., Chua, D. H. C., Zahn, D. R. T., Okano, K., Sub-band formation in amorphous Selenium superlattice and its controlled physical properties, Institute of Electronics and Information Communication Engineering (IEICE) Electronic Devices Conference, Tokyo Japan, November 2019.

4. K. Okano, **J. D. John**, Liberal arts education for science and engineering students in Japan, International Conference on Materials for Advanced Technologies, Singapore, June 2019.

5. **John, J. D.**, Enomoto, K., Miyachi, N., Saito, I., Masuzawa, T. , Chua, D. H., Yamada, T. and Okano, K., Response time of amorphous selenium based photodetector driven by diamond cold cathode, International Vacuum Nanoelectronics Conference (IVNC), Osaka Japan, June 2018.

6. **John, J. D.**, Enomoto, K., Miyachi, N., Saito, I., Masuzawa, T. , Chua, D. H., Yamada, T. and Okano, K., Electronic characteristics of amorphous Selenium and Silicon heterostructure, Atomically Controlled Surfaces Interfaces and Nanostructures (ACSIN-14), Sendai Japan, October 2018.

7. K. Okano, **J. D. John**, I. Saito, T. Masuzawa, T. Yamada, D. H. C. Chua, Device applications of amorphous selenium (a-Se) photoconductor, IEEE Nanotechnology Materials and Devices Conference, Singapore, October 2017.

8. ダイヤモンド冷陰極を用いたX線検出機試作に向けた課題、岡野健、遠山諒、増澤智昭、斉藤市太郎、**Joshua D John**, 山田貴壽, 第１４回真空菜ナノエレクトロニクスシンポジウム、03/2017

9. Tomoaki Masuzawa, Akinori Ohata, Jun Ochiai, **Joshua D. John**, Ichitaro Saito, Takatoshi Yamada, Yoichiro Neo, Hidenori Mimura, Ken Okano, Char-

acterisation of amorphous selenium based photoconductor for high-sensitivity photodetector driven by diamond cold cathode, International Vacuum Nanoelectronics Conference (IVNC), June 2017.